

POLITECNICO DI TORINO

Collegio di Ingegneria Chimica e dei Materiali

**Corso di Laurea Magistrale
in Ingegneria Chimica e dei Processi Sostenibili**

Tesi di Laurea Magistrale

**TiO₂ mixed phases and their behaviour
towards the photocatalytic degradation of
N-phenylurea**



Relatori

prof.ssa Barbara Bonelli
dott.ssa Francesca Stefania Freyria

Candidato

Vincenzo Annelio

Ottobre 2019

Summary

Sommario	I
1. Introduction.....	1
2. Photocatalysis.....	5
2.1 Photocatalysis fundamentals.....	5
2.2 Materials for photocatalytic applications	9
2.3 The effect of doping	10
2.4 TiO ₂ photocatalysis.....	11
2.5 TiO ₂ synthesis methods	13
2.5.1 Sol gel route	13
2.5.2 Hydrothermal route	13
2.5.3 Solvothermal route.....	14
2.5.4 Reverse micelles route	14
3. Pesticides	15
3.1 Persistent organic pollutants: which pesticides are included?.....	15
3.2 Contamination level in EU and Italian ground water	16
3.3 N-containing organic compounds.....	16
3.3.1 Phenylurea family	17
3.4 Degradation pathways for phenylureas	19
4. Catalyst characterization	23
4.1. Techniques used in this work: summary	23
4.2 X-ray Powder Diffraction (XRD).....	23
4.2.1 Theory	23
4.2.2 Data acquisition	25
4.3. BET analysis.....	26
4.3.1 Theory.....	26
4.3.2 Adsorption models.....	28
4.3.2.1 Langmuir model.....	28
4.3.2.2 BET model.....	29
4.3.3 Data acquisition	29
4.4. UV-Vis spectroscopy.....	30
4.4.1. Theory.....	30
4.4.2 Instrument description and data acquisition	32
4.5 Infrared spectroscopy	34
4.5.1 Theory	34

4.5.2 Instrument description	35
4.6 Transmission electron microscopy (TEM)	36
4.6.1 Theory	36
4.6.2 Data acquisition	37
4.7 Dynamic light scattering (DLS): ζ potential measurements	37
4.7.1 Theory	37
4.7.2 Data acquisition	38
5. Materials	41
5.1 Template-assisted sol gel method	41
5.1.1. Method description	41
5.1.2 Synthesis #1: a triblock copolymer used as template	42
5.1.3 Synthesis #2: Fe doped Mesoporous Titania	43
5.1.4 Synthesis #3: Reverse Micelle TiO ₂	44
5.2 Sol gel method in acidic condition	44
5.2.1 Synthesis #4: mixed phase anatase/brookite TiO ₂ in acidic medium	44
5.3 Characterization results	45
5.3.1. Degussa P25: used as reference	45
5.3.2 Template-assisted mesoporous titania: MT	47
5.3.3 Template-assisted mesoporous titania: Fe-MT_dirc	49
5.3.4 Template-assisted mesoporous titania: RM-TiO ₂	51
5.3.5 Sol gel method in acidic conditions: B-TiO ₂ _200	54
5.3.6 Sol gel method in acidic conditions: B-TiO ₂ _600	56
5.4 ζ potential measurements	58
5.5 Titania electronic properties: direct or indirect band gap	61
6. Photocatalytic degradation tests	65
6.1 Experimental setup	65
6.2 Photolysis	66
6.3 Photocatalytic tests under simulated solar light	67
6.3.1 Template assisted mesoporous titania: MT	67
6.3.2 Template assisted mesoporous titania: Fe-MT_dirc	68
6.3.3 Template assisted mesoporous titania: Fe-MT_dirc + H ₂ O ₂	68
6.3.4. RM-TiO ₂	69
6.3.5 B-TiO ₂ _200	70
6.3.6 B-TiO ₂ _600	71
6.3.7 Degussa P25	72

6.4 Photocatalytic tests under UV light.....	73
6.4.1 Template assisted mesoporous TiO ₂ : MT.....	73
6.4.2 Template assisted mesoporous TiO ₂ : Fe-MT_dirc	73
6.4.3 RM-TiO ₂	74
6.4.4 B-TiO ₂ _200	75
6.4.5 B-TiO ₂ _600	76
6.4.6 Degussa P25.....	76
6.5 Powders behaviour under simulated solar light and UV light.....	77
6.5.1 UV light	77
6.5.2 Solar light.....	78
6.6 N-phenylurea degradation rate under simulated solar light.....	79
7. Summary	81
Bibliography.....	83

Sommario

A causa dei disastri naturali e dell'incremento demografico registrato negli ultimi decenni, è stato necessario sviluppare le migliori tecnologie disponibili per fronteggiare l'incombente scarsità delle risorse idriche. Le acque provenienti da siti industriali e/o civili contengono solidi sospesi e altre sostanze chimiche di recente scoperta che sono in grado di bioaccumularsi nei tessuti umani ed animali. Si tratta degli inquinanti organici persistenti (POPs, persistent organic pollutants) che agiscono come inibitori del sistema endocrino (prodotti farmaceutici o per la cura personale, pesticidi). Secondo il network NORMAN (organo dell'Unione Europea), la classe dei contaminanti emergenti include le sostanze chimiche che non fanno ancora parte di alcun programma di monitoraggio. Potranno essere normate da regolamentazioni future sulla base della loro ecotossicità e sui potenziali effetti che esercitano sulla salute umana. Solo recentemente sono state sviluppate delle tecniche analitiche capaci di caratterizzare questi inquinanti che sono presenti nelle acque di falda e superficiali in concentrazioni dell'ordine dei nanogrammi. (Freyria, 2018)

Le tecnologie convenzionali utilizzate per lo smaltimento dei reflui (adsorbimento, coagulazione) non sono capaci di degradare totalmente i contaminanti ma li trasferiscono ad altre fasi, sono costosi e richiedono una elevata quantità di reagenti oltre a generare prodotti di scarto con alto grado di tossicità.

In termini di efficienza e sostenibilità, i processi di ossidazione avanzata (AOPs, advanced oxidation processes) risultano essere i più promettenti nella degradazione dei contaminanti emergenti dalle acque di scarico. Essi sono utilizzati per produrre radicali ossidrilici che sono responsabili dell'ossidazione dei composti organici a CO_2 ed H_2O (reazione di mineralizzazione) senza trasferimento di fase. Sono processi fotochimici che si basano sull'interazione luce-materia e possono agire in combinazione con materiali semiconduttori sensibili alla luce (il più utilizzato è il biossido di titanio) nella degradazione di molecole inquinanti (processo fotocatalitico). A questo proposito il TiO_2 è capace di generare radicali se irradiato da radiazione luminosa di un'opportuna lunghezza d'onda.

Questo lavoro di tesi si propone di studiare le proprietà del TiO_2 , catalizzatore ampiamente utilizzato per applicazioni ambientali, soprattutto nel campo della disinfezione e potabilizzazione delle acque da pesticidi. Tre differenti metodi di sintesi sono impiegati per ottenere catalizzatori nanostrutturati composti da fasi miste del TiO_2 (anatasio, rutilo, brookite). L'attività di questi catalizzatori è stata testata nella degradazione fotocatalitica della N-phenylurea, molecola modello rappresentativa della famiglia delle feniluree. I risultati ottenuti sono stati comparati con quelli del catalizzatore commerciale Degussa P25, una miscela bicristallina di anatasio-rutilo (80%-20%).

I tre metodi di sintesi impiegati si rifanno al metodo sol-gel convenzionale al quale sono state apportate alcune modifiche:

- (i) Metodo sol-gel assistito da templante: un copolimero triblocco (Pluronic, P123) viene utilizzato per dotare il catalizzatore di una struttura mesoporosa ordinata;
- (ii) Metodo sol-gel assistito da template con formazione di micelle inverse: un copolimero diblocco (BrijO20) contribuisce al processo self-assembly in un'emulsione acqua/idrocarburo;
- (iii) Metodo sol-gel semplificato in ambiente acido;

Le polveri ottenute sono state caratterizzate utilizzando le seguenti tecniche: diffrazione a raggi X che fornisce le informazioni relative alla presenza di fasi cristalline e loro quantificazione percentuale (tramite Rietveld refinement); le isoterme di adsorbimento/desorbimento di N₂ a 77 K sono state studiate con l'obiettivo di calcolare i valori di area superficiale specifica utilizzando la teoria Brauner Emmett Teller (BET); sono state effettuate misure di potenziale ζ per una stima dei fenomeni di adsorbimento superficiale tra molecola bersaglio e catalizzatore; lo studio della morfologia delle nanoparticelle è stato effettuato per mezzo della microscopia elettronica a trasmissione e scansione (TEM-FESEM); per stimare qualitativamente il meccanismo di degradazione del contaminante, sono state effettuate misure di assorbanza mediante spettrofotometria UV-Vis. Con l'ausilio di una sfera integrativa montata direttamente sullo strumento è stato possibile effettuare misure di riflettanza diffusa per calcolare i valori di band gap delle fasi polimorfe del TiO₂ per studiarne le proprietà ottiche.

I.I Fondamenti di fotocatalisi

Se un semiconduttore viene irradiato da un fotone con energia $h\nu \geq E_{bg}$ (energy band gap), si promuove il trasferimento degli elettroni dalla banda di valenza a quella di conduzione. Nella banda di valenza si genera una buca capace di reagire con le molecole d'acqua adsorbite sulla superficie del catalizzatore per produrre radicali ossidrilici dotati di un forte potere ossidante verso le molecole organiche. Gli elettroni promossi nella banda di conduzione reagiscono, invece, con l'ossigeno disciolto in acqua per generare il radicale superossido O₂⁻ che si lega ai prodotti intermedi di reazione convertendosi in perossido, perossido di idrogeno e infine acqua (Saravanan, 2017). Se l'ambiente di reazione è aerato in modo continuo, O₂ disciolto in acqua si adsorbe sulla superficie del catalizzatore e funge da iniziatore per la catena di reazioni fotocatalitiche. I due portatori di carica (buca h⁺, elettrone e⁻) migrano verso la superficie del catalizzatore e nel frattempo possono incontrare difetti nella struttura del semiconduttore prima che avvenga il trasferimento di carica all'interfaccia. I difetti reticolari nella struttura del semiconduttore possono essere di due tipi a seconda che questi si trovino in prossimità delle bande (shallow traps) o ad un livello superiore all'interno della banda proibita (deep traps). La presenza di questi difetti intrinseci può essere causata da una violazione della stechiometria durante la preparazione dei catalizzatori (Gaya, 2013) e introduce una serie di stati discreti di energia che possono ospitare sia le buche che gli elettroni, fungendo così da sedi preferenziali per il fenomeno della ricombinazione di carica. Un esempio di shallow trap è l'introduzione nel reticolo del semiconduttore di eteroatomi dopanti; le deep traps negli ossidi semiconduttori sono invece associate alle vacanze di ossigeno. Quando i portatori di carica si ricombinano possono rilasciare energia sotto forma di calore (fononi) o sotto forma di fotoni con un'energia pari al E_{bg}.

I.II Materiali utilizzati in applicazioni fotocatalitiche

I materiali più frequentemente utilizzati per le applicazioni fotocatalitiche sono gli ossidi semiconduttori inorganici. Questa classe di composti è altamente stabile, abbondante in natura oltre ad essere biocompatibile e facilmente riutilizzabile. TiO₂, ZnO, SnO₂, CeO₂ sono ossidi semiconduttori che hanno trovato largo impiego nella degradazione delle sostanze organiche, soprattutto nei coloranti. (Mansoob Khan, 2015) Grazie alle loro proprietà elettroniche sono capaci di assorbire quanti di luce con una lunghezza d'onda nell'intervallo UV-Vis (190-700 nm).

I.III Proprietà del biossido di titanio

TiO₂ è capace di assorbire solo la radiazione ultravioletta. Ha un band gap $E_{bg}=3.0-3.2$ eV e può essere fotoattivato solo se un quanto di luce con una lunghezza d'onda $\lambda < 388$ nm raggiunge la sua superficie sfruttando così solo il 4% della radiazione dello spettro elettromagnetico. Si trova in natura in 3 differenti fasi polimorfe: anatasio, rutile e brookite. Il rutile e l'anatasio hanno struttura cristallina tetragonale, la brookite ha struttura ortorombica.

La geometria delle tre fasi polimorfe può essere descritta utilizzando una struttura ottaedrica in cui lo ione Ti⁴⁺ si coordina con 6 atomi di ossigeno (TiO₆). Le forme cristalline differiscono a causa della distorsione delle catene ottaedriche che costituiscono il reticolo: nella fase anatasio due strutture ottaedriche adiacenti condividono i vertici, nella fase rutile ad essere condivisi sono gli spigoli. La forma allotropica anatasio è ampiamente considerata come la più attiva nei processi fotocatalitici mentre il rutile è la fase termodinamicamente più stabile. La stabilità delle fasi cristalline dipende fortemente dalle condizioni di temperatura e pressione adoperate durante il processo di sintesi oltre che dalla dimensione dei cristalli. A questo proposito, la transizione anatasio-rutile (AR) avviene a ca. 600°C e la stabilità delle fasi polimorfe può essere discussa confrontando i valori di energia libera superficiale che dipendono dalle dimensioni dei cristalli sintetizzati. Le particelle di anatasio con dimensioni $d_p < 14$ nm hanno un'energia libera superficiale minore dei cristalli di rutile, quindi risultano termodinamicamente più stabili. La fase rutile è stabile se $d_p < 35$ nm mentre la brookite per $11 \text{ nm} < d_p < 35$ nm. (Pawar, 2018)

TiO₂ in fase anatasio è un semiconduttore dotato di band gap indiretto, il rutile e la brookite hanno un band gap diretto. Per un semiconduttore con band gap indiretto la transizione diretta della coppia fotogenerata dalla banda di conduzione alla banda di valenza viene proibita, ciò comporta un ritardo nei fenomeni di ricombinazione di carica rendendo l'anatasio la fase più attiva fotocataliticamente.

L'alto valore di E_{bg} nel TiO₂ puro non permette di sfruttare la radiazione visibile nei processi fotocatalitici. Per sintetizzare dei catalizzatori che mostrino un'efficiente attività sotto l'azione della luce visibile è necessario ricorrere al processo del doping. TiO₂ può essere dopato con eteroatomi appartenenti alla famiglia dei metalli di transizione (Fe, Cu, Mo) o dei non metalli (C,N,S). La dispersione delle nanoparticelle di un eteroatomo metallico nel reticolo cristallino del semiconduttore permette la formazione di nuovi livelli discreti di energia che fungono da trappole per gli elettroni ritardando il fenomeno di ricombinazione di carica e favorendo, quindi, l'allontanamento degli elettroni dalla superficie del catalizzatore. Il doping con un metallo promuove il trasferimento degli elettroni all'O₂ molecolare accelerandone la riduzione che risulta essere lo step che limita la cinetica della reazione globale. (Mogal, 2013) Se il doping è effettuato con un eteroatomo non metallico si promuove la capacità del semiconduttore di assorbire la luce visibile: un esempio è rappresentato dal N-TiO₂. Si ha un restringimento della banda proibita grazie alla generazione di nuovi orbitali risultanti dall'ibridazione degli orbitali 2p dell'azoto con gli orbitali 2p dell'ossigeno che hanno energie comparabili e possono ospitare le lacune promosse dalla banda di valenza. (Zaleska, 2008)

I.IV Contaminanti organici contenenti azoto: proprietà della N-phenylurea e meccanismi di degradazione

In questo lavoro si tratta lo studio di un sistema fotocatalitico per la degradazione di composti organici contenenti azoto. Prima di esaminare nel dettaglio i metodi non convenzionali che utilizzano la luce in combinazione con altri agenti ossidanti (H_2O_2 , $\text{Fe}^{3+}/\text{H}_2\text{O}_2$ reazioni di tipo Fenton) è necessario passare in rassegna alcune delle fonti di azoto presenti in natura:

- Amminoacidi, proteine e sostanze umiche;
- Urea, ammoniaca prodotte dal metabolismo umano;
- Sostanze organiche derivanti dalle industrie: derivati dell'acido nitrico e coloranti (Freyria, 2017)

I composti organici contenenti azoto sono presenti sia nelle acque di falda che in quelle superficiali con una concentrazione variabile tra 0.5 e 2.5 mgL^{-1} .

Un pesticida può essere disciolto in acqua con una concentrazione limite di 0.1 μgL^{-1} , questo valore è diverso per le miscele di pesticidi (1 μgL^{-1}) così come riportato nel Decreto Ministeriale DM 56/2009 (Paris, 2016)

Il pesticida oggetto di studio è N-phenylurea (NPU) la cui struttura è mostrata in Fig. (58). È conosciuta con il nome di fenilcarbammide, dai gruppi funzionali che la compongono: fenilico $-\text{C}_6\text{H}_5$ e carbammico $-\text{NH}_2\text{CONH}_2$. È una polvere idrofila con una solubilità in acqua di 10 mg/mL (Liu, 2010). I pesticidi di questa famiglia sono commercializzati con i nomi di Diuron, Bromuron o Fenuron che sono composti arilici polisostituiti. Sono sostanze organiche persistenti caratterizzate da un tempo di dimezzamento di 30-40 giorni nel terreno e di 200 giorni in acqua.

La mineralizzazione dei composti organici azotati porta alla formazione di diverse specie (NO_3^- , NH_4^+ e azoto elementare). Le prime due risultano essere potenzialmente nocive per la salute umana, l'ultima è inerte.

Il meccanismo di degradazione dei composti arilici azotati è complesso e ancora oggetto di studio. Viene riportata la sequenza di ossidazione del Diuron come esempio (Oturán, 2010):

- I gruppi metilici delle catene laterali vengono ossidati;
- L'anello aromatico subisce idrossilazione. Questa reazione è competitiva rispetto all'apertura dell'anello, che è un altro sito preferenziale di attacco dei radicali ossidanti. È più facile che l'apertura dell'anello avvenga per un intermedio idrossilato e che per effetto di attacchi successivi da parte delle specie ossidanti si abbia formazione di aldeidi che si ossidano immediatamente ad acidi carbossilici essendo altamente instabili;
- Declorazione: questo step dipende dalla natura dei sostituenti sull'anello aromatico. N-phenylurea non è sostituito quindi non subisce la reazione.

I gruppi alchilici laterali, legati all'anello aromatico, hanno un'alta reattività. Così, l'urea può reagire con una lacuna h^+ adsorbendosi sulla superficie del catalizzatore ed

ossidandosi per prima. Un prodotto dell'ossidazione dell'urea in acqua può essere NH_4^+ che a sua volta è trasformato in NO_3^- . La presenza di nitrati è facilmente monitorabile seguendo l'evoluzione della banda di assorbimento a 300-320 nm di uno spettro UV-visibile.

Le feniluree possono subire la fotolisi dei legami laterali C-X (se sono sostituite), fotoeliminazione, fotossidazione (reazione di Norrish di tipo II) e fotoriarrangiamento (Bamba, 2017)

Le ipotesi avanzate sopra sono supportate da altri lavori (Lhomme, 2005) in cui viene studiata la degradazione del Chlortoluron e viene ipotizzato un percorso di degradazione:

- I radicali ossidrilici attaccano i gruppi metilici della catena laterale provocando la formazione di prodotti carbossilati;
- L'anello aromatico è idrossilato.

Dalle informazioni raccolte si può affermare che i radicali OH^\bullet attaccano preferenzialmente i gruppi metilici (delle catene laterali) e l'anello aromatico. Effettuando delle analisi di cromatografia liquida, su un campione irradiato per 2 ore dalla luce solare simulata, è emerso che i gruppi metilici sono stati ossidati ad acido formico che a sua volta si è decomposto in acido acetico. L'unico modo per ottenere acido acetico è l'apertura dell'anello aromatico sottoposto a reazioni di decarbossilazione successive solo dopo alcune ore di irraggiamento.

I.V Metodi di sintesi

I.V.I Metodo sol-gel assistito da templante

I precursori di sintesi del TiO_2 sono altamente reattivi in acqua e per ottenere nanoparticelle stabili si possono utilizzare dei tensioattivi non ionici che agiscono da templanti. Il templante Pluronic (P123) viene utilizzato per la sintesi di due campioni MT e Fe-MT-dirc. P123 è un copolimero triblocco simmetrico costituito da catene alternate PEO_{20} - PPO_{70} - PEO_{20} . L'utilizzo del templante induce una limitazione spaziale promuovendo la crescita di nanoparticelle con mesoporosità ordinata o gerarchica, inoltre riduce i processi di aggregazione (Phattepur, 2019). Gli alcossidi di titanio utilizzati come precursori possono essere stabilizzati efficacemente se il tensioattivo non ionico viene disperso in una soluzione alcolica con una concentrazione minore della CMC (concentrazione critica micellare). Si propone, perciò, una descrizione sommaria del processo EISA (formazione delle micelle indotta da evaporazione del solvente) accoppiato al metodo di sintesi sol-gel (Bonelli, 2017).

Il processo EISA è condotto in una miscela acqua/etanolo seguito dalla formazione degli oligomeri del precursore di sintesi che è controllata dall'aggiunta di un acido (come HCl). Se si modificano le condizioni di umidità relativa dell'aria circostante è possibile indurre l'evaporazione del solvente favorendo il processo di formazione delle micelle. Quest'ultimo si verifica mediante la formazione di interazioni deboli (generalmente legami idrogeno) tra il catalizzatore acido e la catena idrofila del tensioattivo. L'acido acetico, per esempio, agisce da stabilizzatore dei precursori di sintesi, in particolare gli ioni acetato si comportano da agenti chelanti aumentando il numero di coordinazione della molecola precursore che raggiunge una configurazione stabile.

Nel metodo sol-gel convenzionale l'idrolisi è uno step veloce che inibisce la seguente polimerizzazione. Se si fa avvenire la reazione di idrolisi in un ambiente catalizzato da acidi è possibile ottenere dei cristalli di dimensioni nanometriche.

Il primo metodo di sintesi prevede la preparazione di due soluzioni differenti:

- la soluzione A è una soluzione acquosa di acido acetico al 20% v/v alla quale viene aggiunto goccia a goccia $\text{Ti}(\text{O}i\text{Bu})_4$ tetrabutossido di titanio, precursore di sintesi. La miscela risultante viene sottoposta ad agitazione magnetica per 4 ore a temperatura ambiente;
- la soluzione B contiene il templante Pluronic 123 disciolto in acqua a cui si aggiunge dell'etanolo. La miscela risultante viene, anch'essa, sottoposta ad agitazione magnetica per 4 ore a temperatura ambiente.

Dopo 4 ore la soluzione A è versata goccia a goccia nella soluzione B facendo attenzione a non formare aggregati. La miscela (A+B) viene sigillata e agitata per 24 ore a temperatura ambiente. In seguito viene posta in un autoclave in Teflon e lasciata in stufa a 98°C per 48 ore (step di invecchiamento). Viene lavata con acqua ed etanolo (in rapporto 1/3) e centrifugata a 4000 rpm per 12 minuti. I cicli di lavaggio sono stati ripetuti fino alla scomparsa di aggregati nel liquido surnatante. La polvere ottenuta è stata essiccata a 60°C per 48 ore e calcinata a 450°C per 4 ore con una rampa di temperatura di $1.8^\circ\text{C}/\text{min}$. Il campione ottenuto è etichettato con MT.

Un campione dopato con Fe è stato ottenuto seguendo la stessa procedura di sintesi opportunamente modificata con l'aggiunta di un sale precursore $\text{FeCl}_3 \cdot 6\text{H}_2\text{O}$ al fine di ottenere una dispersione pari al 2.5% p/p.

Un ulteriore metodo di sintesi è proposto nel lavoro di Nasi et al. È di nuovo basato sul metodo sol-gel assistito da templante in cui viene utilizzato un copolimero diblocco (nome commerciale BrijO20). Se in contatto con un solvente organico è capace di formare micelle inverse. Questo metodo viene utilizzato per controllare le velocità di reazione di idrolisi e condensazione inibendo la formazione di idrossidi di Ti che potrebbero precipitare. I reagenti utilizzati per questa sintesi sono: Brij-O20, cicloesano e butossido di titanio.

Il tensioattivo viene disperso nella fase idrocarburica tramite agitazione magnetica a 50°C . viene aggiunta acqua bidistillata per generare una microemulsione di acqua in olio. La miscela risultante viene agitata per 45 minuti. Il precursore del Ti viene aggiunto goccia a goccia all'emulsione che viene agitata per 2 ore a 50°C . L'emulsione viene rotta con l'aggiunta di 2-propanolo e poi sonicata. In seguito, viene centrifugata ed essiccata a 100°C per 24 ore. Allo scopo di rimuovere il tensioattivo si effettua un trattamento termico di calcinazione a 500°C con una rampa di temperatura di $2.5^\circ\text{C}/\text{min}$ per 2 ore. Il campione ottenuto è etichettato con RM- TiO_2 .

I.V.II Tecnica sol gel in ambiente acido

Modificando opportunamente la temperatura di calcinazione e/o il pH della soluzione si possono sintetizzare fasi miste del TiO_2 . Viene proposto un metodo di sintesi semplificato basato sulla tecnica sol-gel convenzionale.

I reagenti usati per la sintesi sono: isopropossido di titanio (TTIP), alcol isopropilico, acido nitrico e acqua bidistillata. Una soluzione alcol/precursore per 20 minuti a 500 rpm e lasciata in stufa a 80°C per 5 ore. In seguito, viene raffreddata fino a raggiungere la temperatura ambiente. Il pH della soluzione viene modificato aggiungendo una soluzione 1M di acido nitrico con lo scopo di generare il sol in ambiente acido a pH =2. Il sol ottenuto gelifica a seguito di agitazione magnetica per 20 ore. Il gel viene lavato con acqua bidistillata, poi centrifugato per 12 minuti a 4000 rpm ed essiccato in un'autoclave in Teflon a 100°C per 12 ore.

Due diversi campioni vengono calcinati con una rampa di temperatura di 5°C/min a 200°C (B-TiO₂_200) e a 600°C (B-TiO₂_600). Prima di testare le polveri nella degradazione fotocatalitica del pesticida, sono state lavate con acqua ed etanolo (in rapporto 3/1) e centrifugate per 10 minuti ad 8000 rpm per essere in seguito essiccate a 60°C per 24 ore.

I.VI Risultati della caratterizzazione

La Figura I riporta i diffrattogrammi a raggi X di quattro campioni sintetizzati oltre a quello del catalizzatore commerciale utilizzato per confrontare le performance nella degradazione della N-phenylurea. P25 (curva nera) è una miscela bicristallina di anatasio (88.8% p/p) e rutilo (11.2% p/p); MT (curva blu) mostra solo picchi relativi alla fase anatasio (il picco più intenso è visibile per $2\theta=25.5^\circ$ e corrisponde al piano cristallino avente indice di Miller 011). Dall'analisi del diffrattogramma si evince che il campione sintetizzato è puro, così come conferma l'analisi quantitativa effettuata mediante Rietveld refinement (100% anatasio). La dimensione media dei cristalliti di MT è di 12.4 nm e le micrografie TEM suggeriscono la presenza di nanoparticelle con forma allungata e dimensioni piuttosto omogenee, al contrario della polvere commerciale che è costituita da particelle di forma irregolare.

Nel campione RM-TiO₂ (curva verde) oltre ai picchi relativi alla fase anatasio è possibile osservare un ampio picco di diffrazione ascrivibile alla presenza della fase brookite per $2\theta=30.7^\circ$. La formazione di quest'ultima fase è probabilmente favorita dall'ambiente acido di reazione generato dalla formazione delle micelle inverse che agiscono da micro-reattore di sintesi. Nonostante la bassa temperatura di calcinazione, dai diffrattogrammi sono visibili dei picchi relativi al rutilo (da analisi qualitativa in quantità pari al 2.1% p/p). La presenza di brookite in catalizzatori nanostrutturati costituiti da fasi miste abbassa la temperatura di transizione di fase verso il rutilo. Le micrografie FESEM mostrano particelle sferiche di forma omogenea ma fortemente aggregate.

Il campione B-TiO₂_200 (curva arancione) mostra i picchi di diffrazione di anatasio (78% p/p) e brookite (22% p/p). Le nanoparticelle hanno forma e dimensioni variabili.

In accordo con l'aumento della temperatura di calcinazione, il campione B-TiO₂_600 mostra i picchi relativi al rutilo.

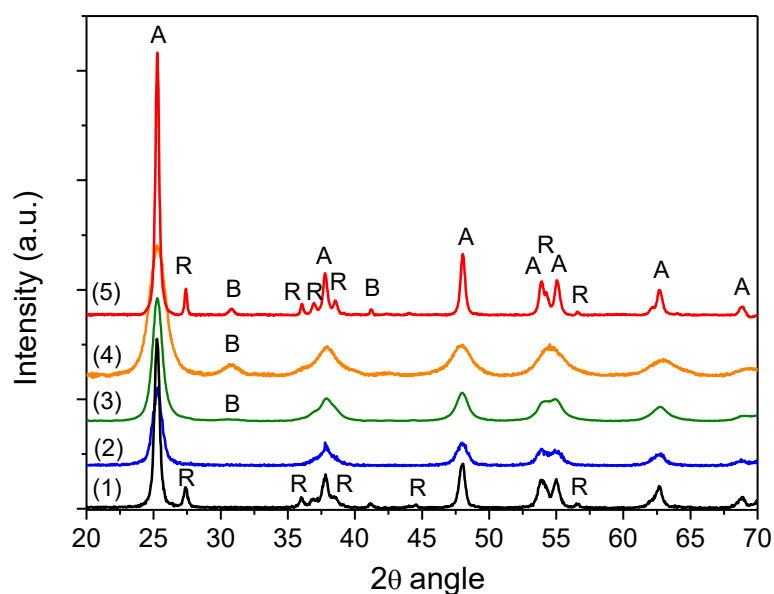


Figura I Diffrattogrammi a raggi X dei campioni sintetizzati

Figura II e Figura III mostrano le isoterme di adsorbimento/desorbimento di N_2 a $-196^\circ C$. La polvere commerciale P25 (curva nera) ha un'isoterma di tipo II, tipica dei materiali macroporosi ed è caratterizzata dalla presenza di meso-macropori interparticellari. Tutti gli altri campioni sintetizzati seguono il comportamento dei materiali mesoporosi poiché si verifica il fenomeno dell'isteresi. Grazie alla classificazione IUPAC è possibile risalire alla struttura dei pori studiando la forma del ramo di isteresi (desorbimento). Tutti i campioni hanno un ramo di isteresi di tipo H2 e sono caratterizzati da una porosità intraparticellare, eccetto RM-TiO₂ la cui porosità è interparticellare. I valori di area superficiale di ciascun campione sono riportati nella Tab. B-TiO₂_200 è il campione con la più elevata area superficiale grazie alla temperatura scelta per effettuare il trattamento di calcinazione ($200^\circ C$).

Applicando il metodo Barrett-Joyner-Halenda (BJH) al ramo di desorbimento delle isoterme è possibile calcolare la distribuzione porosimetrica (PSD) di ciascun campione (Fig. IV). La curva distributiva relativa al campione RM-TiO₂ ci suggerisce la presenza di mesopori con il diametro più piccolo; MT esibisce una curva asimmetrica la cui moda è pari a 7.5 nm. Il volume dei pori diminuisce all'aumentare della temperatura di calcinazione, ciò viene confermato dai risultati ottenuti confrontando le distribuzioni per i due campioni B-TiO₂_200 e B-TiO₂_600.

I risultati della caratterizzazione sono riassunti in Tabella I.

Tabella I Risultati della caratterizzazione: il metodo Williamson-Hall è stato utilizzato per calcolare il diametro dei cristalliti; l'analisi quantitativa delle fasi è stata condotta per mezzo del Rietveld refinement; si riportano le aree superficiali dei catalizzatori dopo aver applicato la teoria BET alle isoterme di adsorbimento/desorbimento di N₂

Sample	Crystallite size (nm)	QPA (%wt)	SSA (m ² /g)	Total pore volume (cm ³ /g)
P25	19±3 (A)	88.8 (A)	74	0.10
	23±4 (R)	11.2 (R)		
MT	12.4±1.3 (A)	100 (A)	147	0.28
RM-TiO₂	10.5±0.4 (A)	83 (A)	70	0.09
	5.4±0.1 (B)	14.9 (B)		
	7.8±0.2 (R)	2.1 (R)		
B-TiO₂_200	5.5±0.6 (A)	78 (A)	210	0.31
	3.8±0.4 (B)	22 (B)		
B-TiO₂_600	39±5.5 (A)	81.6 (A)	31	0.09
	16.8±3.6 (B)	9.3 (B)		
	52.1±8.1 (R)	9.1 (R)		
Fe-MT_dirc	12 (A)	100 (A)	130	0.25

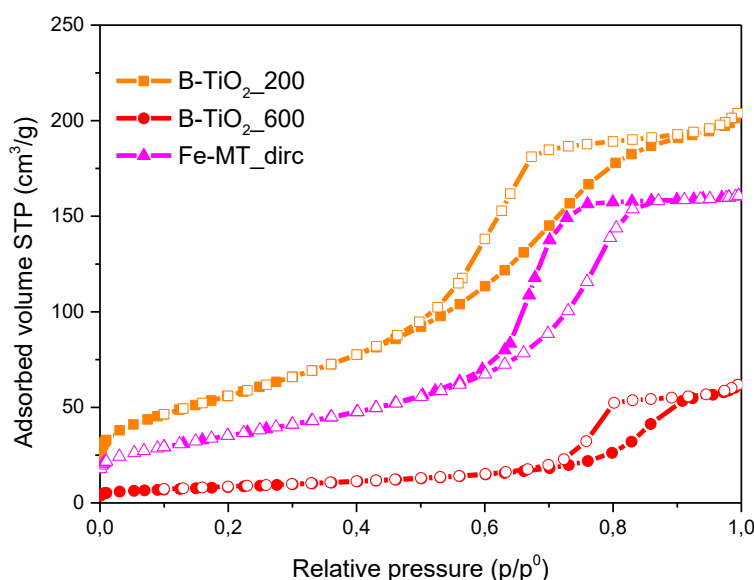


Figura II Isotherme di adsorbimento/desorbimento di azoto a 77 K per i campioni B-TiO₂_200 (curva arancione), B-TiO₂_600 (curva rossa), Fe-MT-dirc (curva magenta)

Fig. V riporta gli spettri ottenuti dalle misure di riflettanza diffusa delle polveri sintetizzate, effettuate con l'obiettivo di calcolare i valori di energy band gap (E_{bg}) dei semiconduttori. I campioni assorbono in un range ristretto compreso tra 365-390 nm ad

eccezione del campione dopato con Fe ($E_{bg} = 2.3$ eV) che assorbe radiazioni nel campo visibile fino ad una lunghezza d'onda di circa 540 nm. I valori di band gap sono calcolati utilizzando il metodo del Tauc plot. Sulla base della distinzione tra semiconduttori a band gap diretto e/o indiretto i calcoli sono effettuati utilizzando la funzione di Kubelka-Munk ($F(R)$); la funzione $(F(R)h\nu)^2$ viene utilizzata per le transizioni dirette; $(F(R)h\nu)^{1/2}$ si utilizza per le transizioni indirette. In letteratura (Lance, 2018) si riportano i valori di band gap per le tre fasi polimorfe del TiO_2 : anatasio (~ 3.2 eV), rutilo (~ 3.0 eV) e brookite (~ 3.56 eV).

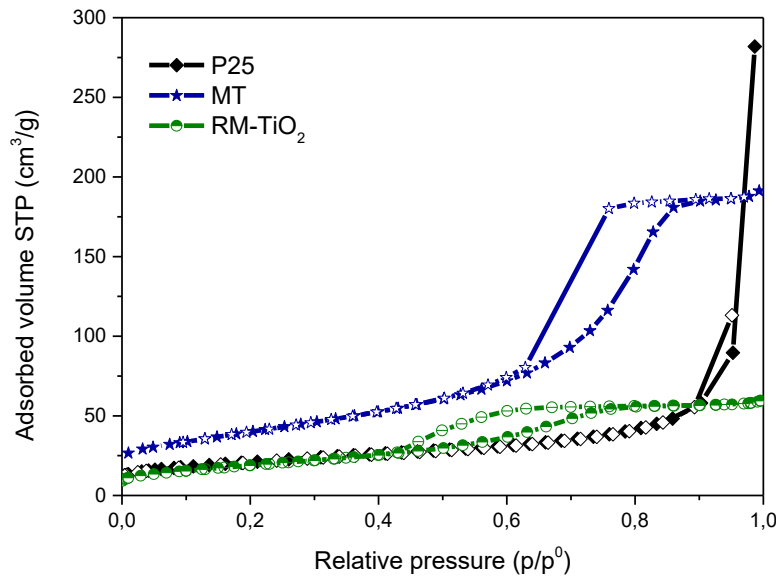


Figura III Isotherme di adsorbimento/desorbimento di azoto a 77 K per i campioni P25 (curva nera), MT (curva blu), RM- TiO_2 (curva verde).

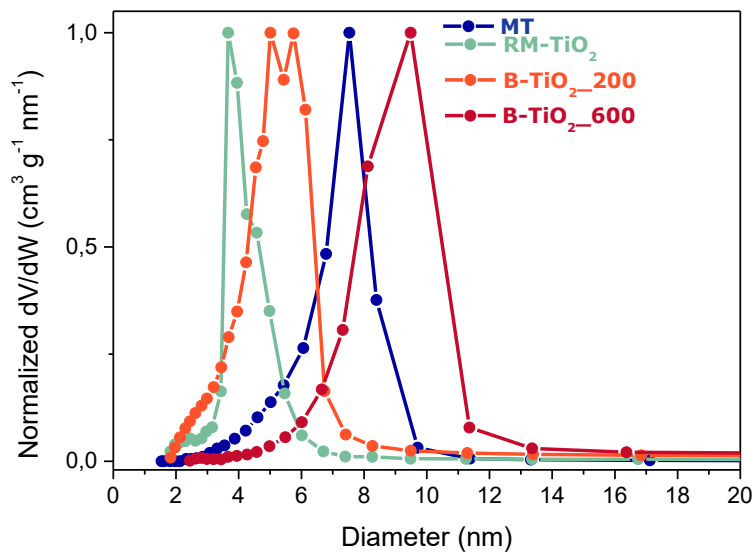


Figura IV Distribuzione porosimetrica dei campioni sintetizzati

I campioni di TiO_2 contenenti fasi miste anatasio/brookite registrano un valore di band gap più elevato. Questo risultato è ascrivibile alla presenza della brookite.

I fenomeni di adsorbimento del pesticida in soluzione acquosa sono strettamente correlati alla carica superficiale delle nanoparticelle. In condizioni di temperatura e pressione ambiente, la fenilurea ha un $\text{pH} = 5.7$ e si adsorbe preferenzialmente sulla superficie di nanoparticelle di TiO_2 cariche negativamente grazie alla generazione di un'attrazione di tipo elettrostatico. Il punto isoelettrico della titania commerciale è pari a $\text{pH}_{\text{IEP}} = 6.2-6.9$. Tutte le polveri sintetizzate in questo lavoro registrano dei valori di pH_{IEP} inferiori (Figura VI).

I valori assunti dal punto isoelettrico possono dipendere dalle condizioni di sintesi e dalle dimensioni delle particelle, al contrario non si è evidenzia nessuna dipendenza dalla struttura cristallina del catalizzatore. Se durante la sintesi delle nanoparticelle si utilizza un tensioattivo (come nel caso del templante) si registrano valori di pH_{IEP} inferiori rispetto a quelli della polvere di riferimento. Ciò può essere dovuto alla presenza di carbonati sulla superficie delle nanoparticelle. Al diminuire della dimensione delle nanoparticelle pH_{IEP} aumenta. Quest'ipotesi è confermata dai risultati ottenuti per il campione RM- TiO_2 le cui condizioni di sintesi permettono di controllare efficacemente la dimensione delle particelle e di ottenere una struttura mesoporosa altamente ordinata.

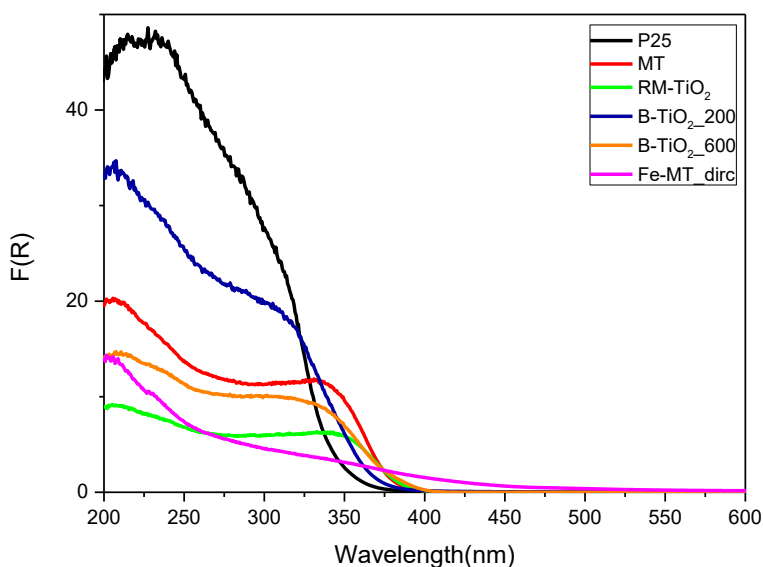


Figura V Spettri delle polveri ottenuti mediante misure in riflettanza diffusa.

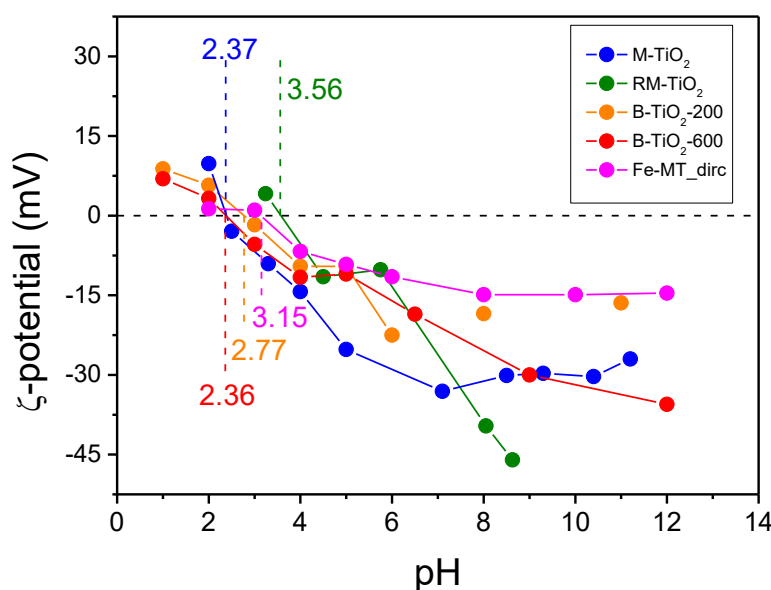


Figura VI Valori del potenziale isoelettrico dei campioni sintetizzati.

I.VII Test fotocatalitici

L'attività fotocatalitica delle polveri sintetizzate è stata testata nella degradazione della N-phenylurea. I parametri che più influenzano l'efficienza di una fotoreazione sono: la natura della radiazione luminosa e la sua intensità; la quantità di catalizzatore utilizzato; la concentrazione del contaminante in acqua; utilizzo di sostanze ossidanti allo scopo di aumentare la velocità di produzione di radicali ossidrilici che sono responsabili della degradazione della materia organica.

I test sono stati effettuati a temperatura ambiente e la soluzione acquosa (50 ml) contenente il pesticida è posta in un reattore di quarzo di forma cilindrica ed esposta all'ossigeno atmosferico. Per irradiare la soluzione si utilizzano due differenti lampade che emettono rispettivamente radiazione visibile e UV. La concentrazione in acqua dell'inquinante esaminato è regolata dalla legge: una concentrazione limite pari a $1 \cdot 10^{-7} \text{M}$ è tollerata nelle acque destinate al consumo umano. Per seguire qualitativamente il meccanismo di degradazione del contaminante si utilizza la spettrofotometria che misura i valori di assorbanza di una soluzione $1 \cdot 10^{-5} \text{M}$ di N-phenylurea allo scopo di evidenziare i picchi di assorbimento caratteristici della sostanza analizzata ($\lambda=199 \text{ nm}$ gruppo amminico; $\lambda=235 \text{ nm}$ gruppo aromatico) verificando la validità della legge di Lambert-Beer per le soluzioni diluite nel range di concentrazione considerato.

La lampada che simula la luce solare ha un'intensità luminosa pari a 1000 W/m^2 ed è posta ad una distanza di 6 cm ortogonalmente al reattore. Essa emette anche una piccola frazione di radiazione ultravioletta con un'intensità pari a 22 W/m^2 . Una intensità luminosa di $55\text{-}60 \text{ mW/cm}^2$ è settata per la lampada UV. La stessa quantità di catalizzatore è utilizzata nei test fotocatalitici (1 gL^{-1}).

Nel test dove è impiegato il campione Fe-MT_dirc si aggiunge alla soluzione H₂O₂ in quantità stechiometrica rispetto alla reazione di parziale mineralizzazione riportata da Malato che porta alla formazione di acido nitrico. La reazione che si instaura in queste condizioni è di tipo Fenton.

La polvere commerciale P25 è molto volatile e rimane finemente dispersa in soluzione perciò è necessario utilizzare un filtro a siringa in cellulosa rigenerata con porosità pari a 0,45 µm in seguito alla centrifugazione per eliminare le particelle solide di catalizzatore dal surnatante la cui assorbanza viene misurata ad intervalli regolari di 1 ora.

Gli spettri del surnatante dei campioni di soluzione contenenti le due polveri B-TiO₂_200 e B-TiO₂_600 evidenziano i picchi caratteristici delle polveri. Quest'effetto può essere dovuto alla presenza di precursore non reagito durante la fase di sintesi e rende difficile l'interpretazione del meccanismo di degradazione. Per ovviare a questo disturbo, le aliquote prelevate sono state centrifugate e successivamente filtrate con la stessa modalità già citata.

I.VII.I MT

Lo spettro della soluzione diluita di N-phenylurea 0.01 mM mostra due picchi di assorbimento caratteristici a 199 nm e 235 nm. La curva (nera tratteggiata in fig VII) relativa ai fenomeni di adsorbimento in assenza di luce ci suggerisce la scarsa interazione tra la molecola contaminante e le nanoparticelle di catalizzatore in soluzione acquosa. Il punto isoelettrico del campione MT è $pH_{IEP} = 2.36$ mentre la soluzione sottoposta ad irraggiamento in condizioni ambiente ha un pH iniziale di ca. 5.5. Per questo motivo le nanoparticelle di titania si caricano negativamente se vengono disperse in acqua. La N-phenylurea è un acido debole con un $pK_a = 13.37$ e mostra perciò poca affinità nell'interazione elettrostatica con particelle di carica superficiale negativa.

Sotto l'azione della radiazione solare simulata l'assorbanza dei cromofori diminuisce in maniera progressiva: dopo tre ore di illuminazione il picco a 235 nm subisce un effetto ipsochromico indice dell'attacco dei radicali ossidrilici sulla catena laterale della molecola bersaglio che è la prima ad essere degradata. Gli stessi radicali agiscono preferenzialmente sull'anello aromatico dopo 4 ore illuminazione, provocandone l'apertura e la formazione di probabili prodotti decarbossilati. Ciò si evince dall'analisi dello spettro UV-Vis (curva arancione) che mostra una nuova banda di assorbimento corrispondente all'intervallo delle lunghezze d'onda $\lambda = 200-210$ nm insieme ad una banda meno pronunciata per $\lambda = 228$ nm dovute alla presenza in soluzione del cromoforo -COOH, gruppo funzionale caratteristico degli acidi carbossilici.

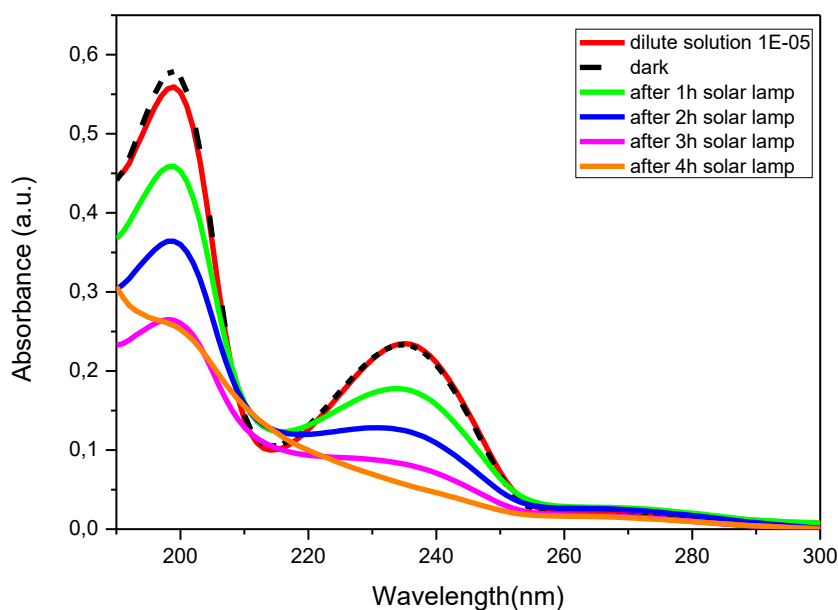


Figura VII Spettri UV-Vis dei surnatanti della soluzione di N-phenylurea prelevati ad intervalli regolari di 1h durante i test fotocatalitici con il campione MT irradiato da luce solare.

I.VII.II RM-TiO₂

La banda di assorbimento a 235 nm subisce un effetto ipsocromico solo dopo 240 minuti. Perciò, l'anello aromatico esibisce un'elevata stabilità sotto l'effetto combinato di radiazione luminosa e catalisi eterogenea. Per questo motivo è probabile trovare in soluzione degli intermedi aromatici idrossilati. Una ulteriore banda, la cui assorbanza è crescente nel tempo, si forma a 280-300 nm. Questo comportamento indica che i radicali ossidrilici abbiano causato la rottura della sola catena laterale della N-phenylurea che si è ossidata progressivamente formando dei nitrati (Fig. VIII)

I.VII.III B-TiO₂_200

Le due bande di assorbimento caratteristiche della molecola bersaglio decrescono progressivamente nel tempo indicando la buona attività della polvere sotto l'effetto della luce solare simulata. Esse subiscono entrambe un effetto ipsocromico traslando verso lunghezze d'onda inferiori (Fig IX). Questo risultato suggerisce un meccanismo di degradazione differente rispetto a quelli descritti finora. Lo shift della banda a 235 nm indica nuovamente la rottura della catena laterale ma i prodotti idrossilati intermedi, generati dall'attacco degli OH[•] che si legano all'anello, sono completamente degradati dopo 4 h di illuminazione.

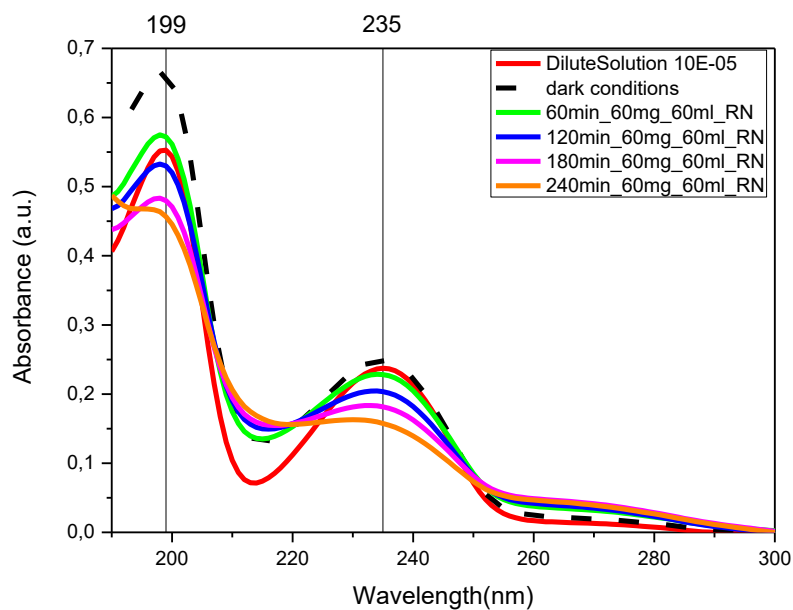


Figura VIII Spettri UV-Vis dei surnatanti della soluzione di N-phenylurea prelevati ad intervalli regolari di 1h durante i test fotocatalitici con il campione RM-TiO₂ irradiato da luce solare.

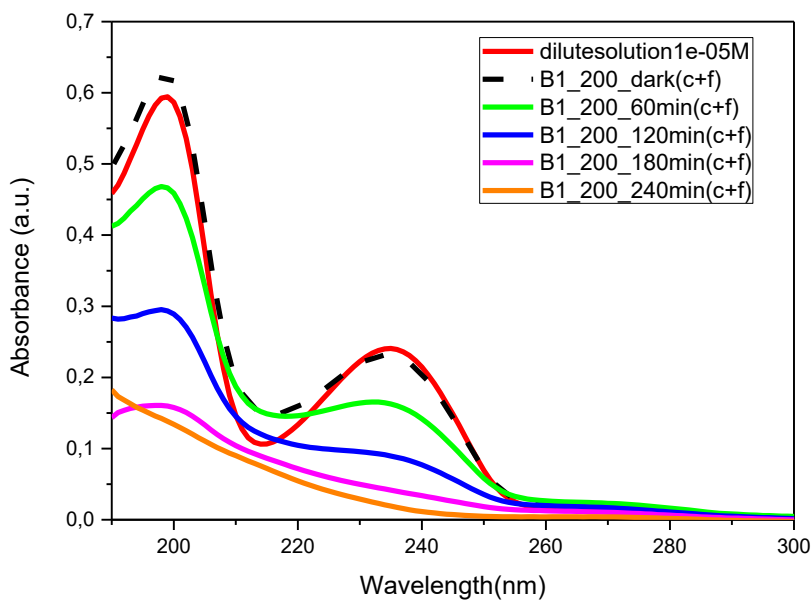


Figura IX Spettri UV-Vis dei surnatanti della soluzione di N-phenylurea prelevati ad intervalli regolari di 1h durante i test fotocatalitici con il campione B-TiO₂_200 irradiato da luce solare.

I.VII.IV B-TiO₂_600

Il picco caratteristico della N-phenylurea a 235 nm subisce effetto ipsocromico, indice della rottura della catena laterale e conseguente formazione di prodotti aromatici idrossilati (Fig.X). Nonostante l'alto contenuto di brookite, risultato promettente nella degradazione del contaminante, le bande di assorbimento si attenuano in maniera meno marcata rispetto al test condotto con il campione B-TiO₂_200. Ciò è dovuto all'effetto della minore superficie specifica esposta alla reazione fotocatalitica. Una nuova banda si forma a $\lambda = 220$ nm suggerendo la formazione di prodotti aromatici idrossilati, poiché il fenolo assorbe a $\lambda = 210$ nm ed ha un coefficiente di estinzione molare $\epsilon = 6000 \text{ M}^{-1}\text{cm}^{-1}$.

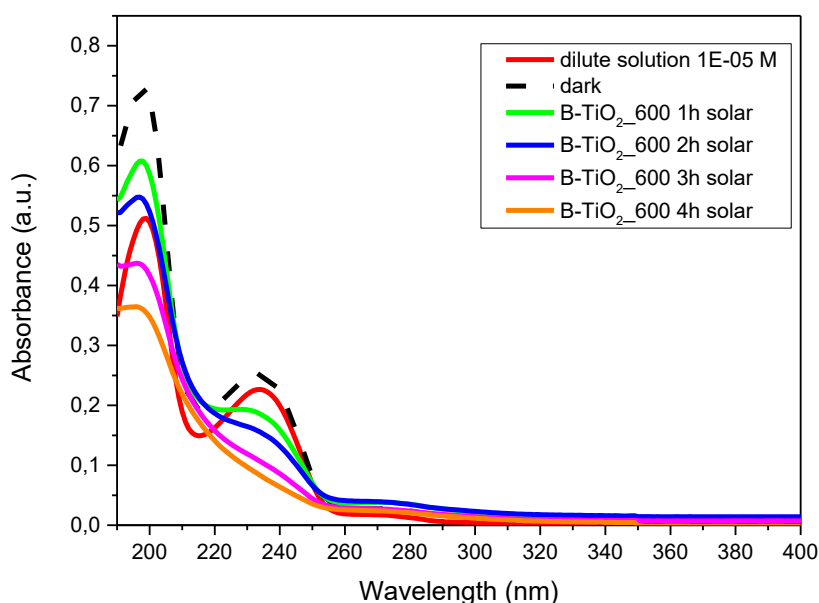


Figura X Spettri UV-Vis dei surnatanti della soluzione di N-phenylurea prelevati ad intervalli regolari di 1h durante i test fotocatalitici con il campione B-TiO₂_600 irradiato da luce solare.

I.VIII Conclusioni

In questo lavoro di tesi sono stati sintetizzati catalizzatori a base di fasi miste di TiO₂ e la loro attività è stata testata della degradazione fotocatalitica della N-phenylurea, considerata recentemente un contaminante emergente.

Per produrre le nanoparticelle di TiO₂ si è ricorso a tre metodi di sintesi differenti:

- (i) Metodo sol-gel assistito da templante (Pluronic P123) seguito da trattamento termico di calcinazione a 450°C per ottenere anatasio puro;
- (ii) Metodo sol gel assistito da templante (BrijO20) in un'emulsione acqua-idrocarburo che favorisce la formazione di micelle inverse;

L'uso del templante promuove la formazione di nanoparticelle di dimensioni controllate e di una struttura mesoporosa; l'ambiente acido che si instaura tra le micelle inverse che agiscono da microreattore durante la sintesi favorisce la formazione della brookite.

- (iii) Metodo sol-gel semplificato in ambiente acido: nessun templante viene utilizzato durante la fase di sintesi ma il pH della soluzione viene modificato tramite l'aggiunta di HNO_3 . Il campione sintetizzato ha esibito il più alto contenuto di brookite e la più alta superficie specifica.

I catalizzatori sintetizzati sono stati caratterizzati mediante diffrattometria a raggi X per ottenere informazioni relative alla formazione e alla composizione relativa delle fasi cristalline; le isoterme di adsorbimento/desorbimento di N_2 a 77 K sono state misurate per calcolare i valori di superficie specifica dei campioni; sono state effettuate misure di potenziale zeta per calcolare i valori del punto isoelettrico per ciascuna polvere. Tutti i campioni hanno esibito pH_{IEP} inferiori rispetto alla polvere commerciale ($\text{pH}_{\text{IEP}} = 6.2-6.9$). Questo risultato è ascrivibile alla differente dimensione delle particelle e alle condizioni di sintesi adoperate.

Una stima dell'indice di polidispersità è data mediante misure di DLS (dynamic light scattering). I valori di PDI, per i due campioni sintetizzati mediante il terzo metodo descritto sopra, si attestano circa a 0.6 suggerendo una migliore dispersione delle nanoparticelle in acqua rispetto ai campioni MT e Fe-MT_dirc. Questo risultato conferma che la presenza di aggregati/agglomerati in acqua influenzi negativamente la resa quantica della reazione.

Infine, la sintesi in ambiente acido promuove la formazione della fase brookite. Il campione B-TiO₂_600 è stato calcinato a 600°C ed esibisce un'area superficiale inferiore rispetto al campione calcinato a 200°C, indice della maggiore cristallinità della polvere. La temperatura scelta per il trattamento termico favorisce la transizione brookite-rutilo che ritarda i fenomeni di ricombinazione di carica.

Per studiare le proprietà ottiche delle polveri cristalline di TiO₂ sono state effettuate misure di riflettanza diffusa per mezzo di una sfera integrata montata direttamente sullo spettrofotometro allo scopo di calcolare i valori di band gap (E_{bg}). Come previsto, Fe-MT_dirc ha mostrato E_{bg} più basso (2.3 eV). Ciò ha confermato l'abilità del campione dopato nell'assorbire radiazioni nel campo della luce visibile. Sono stati calcolati i valori di band gap diretto ed indiretto mediante il metodo del Tauc plot che utilizza la funzione di Kubelka-Munk $F(R)$. B-TiO₂_200 ha esibito un valore di band gap maggiore rispetto al campione contenente anatasio puro (MT) a causa della presenza di una miscela bicristallina di anatasio e brookite. Perciò i valori E_{bg} crescono all'aumentare del contenuto di brookite.

Tutte le polveri sono state testate sotto l'azione della luce solare simulata e della radiazione ultravioletta. Risultati promettenti nella degradazione del contaminante sono stati ottenuti dal campione B-TiO₂_200, caratterizzato dalla più elevata superficie specifica e dal più elevato contenuto di brookite. B-TiO₂_600 ha mostrato una buona attività, nonostante la sua ridotta area superficiale. Le tre fasi di cui è costituito sono ben interconnesse e ciò ritarda la ricombinazione buca-elettrone. Questo risultato suggerisce che i meccanismi di ricombinazione di carica influenzano maggiormente il processo fotocatalitico rispetto alla superficie specifica dei campioni, seppur questa sia indice del numero dei siti attivi esposti disponibili per la reazione.

P25 ha anch'esso mostrato una buona attività sotto l'effetto di entrambe le sorgenti luminose, essendo una miscela bicristallina di anatasio e rutilo. Questa polvere è finemente dispersa in acqua e fornisce probabilmente una superficie esposta alla reazione maggiore di quella calcolata con le isoterme di adsorbimento.

Al contrario, il campione RM-TiO₂ disperso in acqua forma aggregati, risultando il campione meno attivo nella degradazione. Nonostante la sua area superficiale sia comparabile con quella del campione commerciale, l'aggregazione delle particelle inibisce i fenomeni di trasferimento di materia diffusivi e influenza la resa quantica della reazione in quanto la presenza di aggregati rende torbida la sospensione.

La buona disperdibilità del campione P25 può suggerire l'utilizzo di una concentrazione di catalizzatore inferiore per effettuare i test catalitici. Analisi successive a questo lavoro potranno essere effettuate allo scopo di calcolare la quantità di catalizzatore da utilizzare, normalizzata rispetto alla superficie specifica del campione commerciale.

Le tecniche analitiche utilizzate per seguire il percorso di degradazione del contaminante non forniscono risultati univoci. Per studiare più efficacemente la natura degli intermedi di degradazione e valutarne l'eventuale tossicità è necessario effettuare misure di cromatografia liquida.

Inoltre, uno studio cinetico più approfondito apporterebbe dati quantitativi relativi alla velocità di degradazione del contaminante esaminato e confermerebbe le tesi esposte relative all'attività dei campioni sintetizzati.

Bibliografia

Freyria, Francesca Stefania, Francesco Geobaldo, and Barbara Bonelli. "Nanomaterials for the abatement of pharmaceuticals and personal care products from wastewater." *Applied Sciences* 8.2 (2018): 170.

Saravanan, R., Francisco Gracia, and A. Stephen. "Basic principles, mechanism, and challenges of photocatalysis." *Nanocomposites for Visible Light-induced Photocatalysis*. Springer, Cham, 2017. 19-40.

Gaya, Umar Ibrahim. *Heterogeneous photocatalysis using inorganic semiconductor solids*. Springer Science & Business Media, 2013.

Khan, Mohammad Mansoob, Syed Farooq Adil, and Abdullah Al-Mayouf. "Metal oxides as photocatalysts." (2015): 462-464.

Pawar, Milind, S. Topcu Sendoğdular, and Perena Gouma. "A Brief Overview of TiO₂ Photocatalyst for Organic Dye Remediation: Case Study of Reaction Mechanisms Involved in Ce-TiO₂ Photocatalysts System." *Journal of Nanomaterials* 2018 (2018).

Mogal, Sajid I., et al. "Metal doped titanium dioxide: synthesis and effect of metal ions on physico-chemical and photocatalytic properties." *Materials Science Forum*. Vol. 734. Trans Tech Publications, 2013.

Zaleska, Adriana. "Doped-TiO₂: a review." *Recent patents on engineering* 2.3 (2008): 157-164.

Freyria, Francesca S., et al. "Catalytic and photocatalytic processes for the abatement of N-containing pollutants from wastewater. Part 2: Organic pollutants." *Journal of Nanoscience and Nanotechnology* 17.6 (2017): 3654-3672.

Paris, P., et al. "Rapporto Nazionale dei Pesticidi Nelle Acque." *ISPRA, Roma* (2016).

Liu, Jing. "Phenylurea herbicides." *Hayes' handbook of pesticide toxicology*. Academic Press, 2010. 1725-1731.

Bamba, Drissa, Mariame Coulibaly, and Didier Robert. "Nitrogen-containing organic compounds: Origins, toxicity and conditions of their photocatalytic mineralization over TiO₂." *Science of the Total Environment* 580 (2017): 1489-1504.

Oturan, Mehmet A., et al. "Kinetics of oxidative degradation/mineralization pathways of the phenylurea herbicides diuron, monuron and fenuron in water during application of the electro-Fenton process." *Applied Catalysis B: Environmental* 97.1-2 (2010): 82-89.

Lhomme, Ludovic, et al. "Photocatalytic degradation of a phenylurea, chlortoluron, in water using an industrial titanium dioxide coated media." *Applied Catalysis B: Environmental* 61.3-4 (2005): 227-235.

Bonelli, Barbara, Serena Esposito, and Francesca S. Freyria. "Mesoporous Titania: Synthesis, properties and comparison with non-porous titania." *Titanium Dioxide* (2017): 119-141.

Phattepur, Harish, Gowrishankar Bychapur Siddaiah, and Nagaraju Ganganagappa. "Synthesis and characterisation of mesoporous TiO₂ nanoparticles by novel surfactant assisted sol-gel method for the degradation of organic compounds." *Periodica Polytechnica Chemical Engineering* 63.1 (2019): 85-95.

Nasi, Roberto, et al. "Application of Reverse Micelle Sol–Gel Synthesis for Bulk Doping and Heteroatoms Surface Enrichment in Mo-Doped TiO₂ Nanoparticles." *Materials* 12.6 (2019): 937.

Lance, Ryan A. "Optical Analysis of Titania: Band Gaps of Brookite, Rutile and Anatase." (2018).

1. Introduction

According to the World Health Organization (WHO), water pollution is the most important environmental aspect concerning human health, more than air pollution or climate change. Chemical contamination plays a key role due to long-term effects. The presence of new chemicals in groundwater raises concerns due to their potential environmental consequences. Emerging pollutants are considered one of the most alarming problems in recent decades. Some of them can be: PFAS (perfluoroalkyl substances), cyanobacteria, mycotoxins, drugs, hormones and pesticides. Pollutants listed above are classified as endocrine disruptors. That is the reason why they could be dangerous for human health.

Interest in the study of emerging pollutants arose in 1962, when Rachel Carson published her book entitled "Silent Spring". It revealed that the excessive use of DDT (dichlorodiphenyltrichloroethane) and pesticides caused the death of several animal species. [1],[2]

Nowadays, studies are focused on new chemicals that have not been detected in groundwater yet.

According to the NORMAN network definition[3], the class of emerging pollutants includes some chemicals that are not involved in any detection program yet. They can be submitted to future regulations based on their ecotoxicity, potential effects on human health.

Only recently some analytic techniques have been developed and they are able to characterize these pollutants that are present in water bodies and soil in very small concentration[4].

The amount of some contaminants in groundwater is regulated by law. Some concentration limits can be defined with respect to the discharge into the receiving water bodies.

Water treatment plants can only partially remove those compounds since they are present in such a low concentration in the wastewater stream (the order of magnitude is about ng / l or µg / L) and are continuously released into water bodies where they cannot be completely degraded.

The removal technologies already used are not effective or consolidated and are not easily applicable to water treatment plants. Scientific research aimed at identifying sustainable treatment solutions.

Drugs and personal care products (referred to as PPCPs) are subject of studies in order to identify concentration ranges in ground and surface water, to analyze the removal or degradation efficiency by using ordinary treatments, to quantify non toxicity concentration for aquatic life due to the presence of some residual. [1]

Many pesticides are carcinogenic to animals and probably also to humans[5]. Potentially, they alter the endocrine system. Atrazine and malathion have shown some interference with the endocrine system even if present in low concentrations[6]. Exposure

to these chemical compounds can cause damage to the reproductive system or metabolic diseases[7]. The two most common pesticides in the United States are atrazine [8] and metolachlor[9]. Conventional treatment technologies such as chlorination, coagulation and filtration are unable to remove emerging contaminants from water. Ozonation is applicable but is rather expensive for large-scale treatments. Advanced oxidation processes (referred to as AOPs) are the most promising treatments for degradation of persistent contaminants from wastewater. Potentially they ensure complete mineralization avoiding phase transfer.

To this purpose, this work deals with the study of TiO₂ properties. It is a semiconductor widely used as catalyst in environmental applications i.e. in the field of water disinfection or purification from pesticides. Three different synthesis methods were employed to tailor nanostructured TiO₂ nanoparticles. The research was focused on the synthesis of mixed phases (anatase, rutile, brookite). The activity of these catalysts was tested in the photocatalytic degradation of N-phenylurea since it is classified as an emerging contaminant and it can be considered as a model substrate for the phenylureas family. AOPs were used to produce hydroxyl radicals OH[•] that are responsible of oxidizing organic compounds to CO₂ and H₂O (mineralization reaction).

The three synthesis methods employed were slightly modified form the conventional sol-gel method typically used in wet chemistry:

- (i) Template assisted sol gel method: a triblock copolymer (Pluronic, P123) acts as template;
- (ii) Template-assisted sol gel method in a reverse micellar environment: a diblock copolymer (BrijO20) acts as template;
- (iii) Facile sol gel method in acidic medium;

Powders obtained were characterized by means of X-ray diffraction that provides information about crystal phases and their quantification (Rietveld refinement); N₂ adsorption/desorption isotherms at -96°C were used to calculate specific surface area (SSA) using the Brauner Emmett Teller (BET) theory; ζ potential measurements were performed to better investigate adsorption phenomena between the target molecule and the catalyst surface dispersed in water; Transmission Electron Microscopy (TEM) or Field Emission Scanning Electron Microscopy (FESEM) were used to study particles morphology; in order to estimate qualitatively the degradation path of the contaminant, UV-Vis spectroscopy was used to measure N-phenylurea absorbance in both UV and visible region. Besides, an integrated sphere was mounted on the spectrophotometer to perform diffuse reflectance (DR-UV) measurements with the aim of calculating energy band gap (E_g) values of the mixed phases.

This work is structured in 6 chapters:

- 1st chapter: photocatalysis fundamentals are discussed; the attention is focused on TiO₂ structure and the fate (charge transfer mechanism) of the photogenerated pair that is responsible of the overall photocatalytic reaction. A brief paragraph is dedicated on doping and its effect on TiO₂ ability to better absorb visible radiation. A short insight of the most used TiO₂ synthesis methods is mentioned;

- 2nd chapter: a definition of pesticides is given besides a short summary of laws regulating their release into surface and ground water. The structure of N-phenylurea is discussed and possible degradation paths were discussed;
- 3rd chapter: a description of conventional methods used to characterize (*vide supra*) synthesized powders and instruments used to perform the measurements is given;
- 4th chapter: synthesis methods are widely discussed; characterization results are given;
- 5th chapter: UV-Vis spectra recorded during the photocatalytic tests are shown and a possible degradation path is discussed for every TiO₂ sample. Both solar and UV light were used to perform the test. A rough estimation of the rate constant for the degradation reaction is given based on Langmuir Hinshelwood (LH) model;
- 6th chapter: conclusions and guidelines for future works are given.

2. Photocatalysis

2.1 Photocatalysis fundamentals

AOPs can be classified depending on how radical species are generated. Photolysis is the process in which the energy of the light is transferred to a reagent molecule and breaks its bonds [10]. First photolysis step results in the generation of a target molecule in an excited state followed by some chemical transformation such as dissociation, isomerization or intermolecular rearrangement [11]. Photocatalytic processes are instead heterogeneous and are based on specific properties of semiconductor materials that are sensitive to light [12].

Photochemistry deals with reactions induced by the interaction between light and matter. It is essentially based on two principles [13]:

- Grotthus-Draper law: a light beam hits the reagents. They absorb some wavelengths and a chemical reaction occurs;
- Stark-Einstein law: every absorbed quantum of light reacts with the molecule.

Photocatalysis is a process in which a photocatalyst modifies the rate of a chemical reaction through the action of the light. It was discovered in 1972 by Fujishima and Honda^[14]. The mechanism of photocatalysis exploits solar energy to make photocatalysts active. If they are irradiated by a radiation of proper wavelength induce the formation of strong oxidant reagents that are able to decompose organic and inorganic compounds.

Titanium dioxide (TiO_2), for example, is capable of generating radicals when illuminated by a radiation of adequate wavelength^[15].

Photocatalysis enhances the oxidation processes already existent in nature. Semiconductors modify the rate of a chemical reaction through the action of the light. When a semiconductor is hit by some photons having an amount of energy which is larger than its energy gap, an electron is capable to migrate from valence to conduction band generating a hole at the upper limit of the valence band. The photogenerated couple electron-hole can either reduce or oxidize a compound which is adsorbed on the catalyst surface.

Photocatalytic performances are strongly affected by the electron mobility [16].

Charge carriers could take different paths [17] as shown in Figure 2.1:

- They can be trapped into pre-existing material defects known as shallow (ST) or deep traps (DT). The latter are associated to oxygen vacancies in metal oxides semiconductors. If photogenerated electrons meet traps before reaching the conduction band or the catalytic site they could persist for a long period of time into the structure of the metal oxide used as photocatalyst (i.e. TiO_2). [18]
- They can recombine releasing the input energy as heat
- They can react with other species (electron donor or acceptor as well) which are adsorbed on the surface of the catalyst.

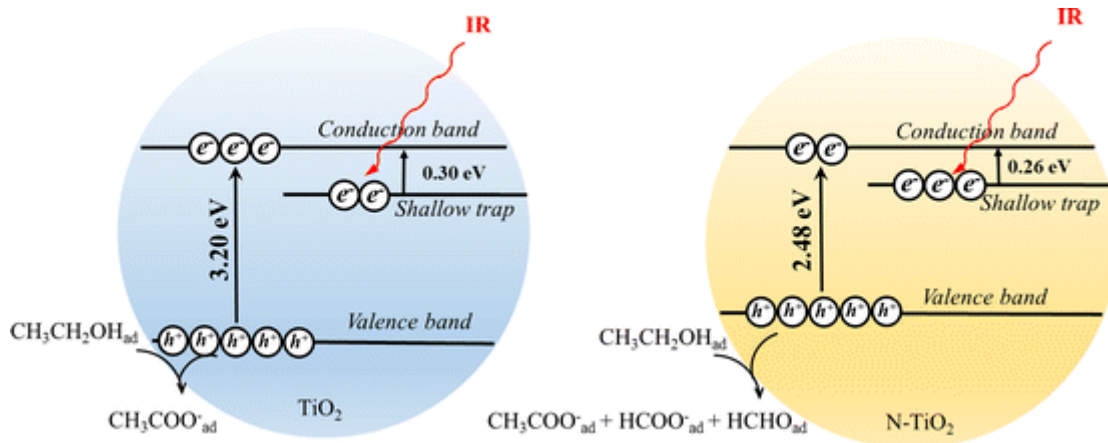


Figure 2.1 Charge carrier mobility in pure and doped TiO₂ (modified by ref. 18)

If the semiconductor is in contact with water the hole can produce hydroxyl radicals while electrons are sufficiently reducing to produce O^{2-} ions from oxygen^[19].

For instance, metal oxides show an appreciated photocatalytic activity because they generate

- OH[•] radicals by oxidation of hydroxyl anions;
- O^{2-} radicals by reduction of oxygen.

The conductivity of a semiconductor can be increased by adding some foreign atoms to its crystal lattice. They supply more electrons in the conductive band (CB) or more holes in the valence band (VB).

Three classes of semiconductors can be distinguished [13]:

- Extrinsic semiconductor (n type): the atoms added to the crystal lattice are able to give up some electrons, the Fermi level is shifted towards the conductive band.
- Extrinsic semiconductors (p type): the atoms added to the lattice are instead able to accept electrons and generate some holes, the Fermi level is moved to the valence band.
- Intrinsic semiconductors: no foreign atoms are added to the lattice.

Fermi level is referred to as an energy level for which there is a 50% probability of finding an electron.

Semiconductors are usually used in form of powder and they are suspended in aqueous solutions. Metal oxides semiconductors behave as electrodes in an electrochemical circuit. An example was provided by Fujishima studying the water splitting process in which TiO₂ was used as a working electrode. Pt black was used instead as counter electrode. When TiO₂ was irradiated by light with $\lambda \leq 415$ nm a current flow occurred from TiO₂ (oxidation site) to Pt (reduction site). In this way hydrogen can be generated from water and no external voltage is needed. [20]

Semiconductors used as photocatalysts have to be:

- Chemically and biologically inert
- Easy to synthesize and reusable
- Light sensitive
- Economic

Solid phase catalysts made by semiconductor metal oxides have a relevant importance because it is possible to act on the main properties of the material by varying the size, morphology and structure of the particles leading to a strong modification in photocatalytic activity.

In particular for semiconductors, size control allows modifications of the material properties without affecting the chemical composition. By varying the size of the crystals it is possible to modify the redox potential of the photogenerated couple. [21]

The photocatalytic activity occurs on the surface of the catalyst. Nanomaterials are characterized by a high surface-volume ratio. Acting on this parameter helps to increase the availability of surface sites, thus increasing the speed of the photodecomposition reaction.

The activity of a photocatalyst can be affected also by its specific surface which is in turn function of particles morphology. The larger is the specific surface the more efficient is the photocatalytic activity. Specific surface can increase if the size of the particles decreases or if particles are made of different shapes such as nanotubes, nanorods.

Photocatalysis process can be divided into three main steps:

- reagents adsorption on the catalyst surface;
- catalytic reaction on the surface;
- products desorption on the catalyst surface.

The catalyst activation occurs when a quantum of light, with an energy larger than the catalyst energy gap, hits the surface. Electrons migrate from VB to CB to generate an electron-hole pair. Photogenerated charge carriers are subjected to the surface electric field and are free to move in any direction, thus their recombination is hindered. The process can be retarded as well because of the presence of some traps on the catalyst surface.

Photogenerated pairs which are not subjected to recombination may diffuse towards the catalyst surface where they react with water or oxygen molecules adsorbed.

Evidently, water and oxygen molecules adsorbed on the catalyst surface play a key role during the whole process. The hydroxyl radical, generated by the reaction between the water and the hole, reacts with the contaminants and oxidizes them.

Oxygen traps electrons by forming O^{2-} which in turn may recombine to form peroxides and hydroxyl radicals, responsible of an oxidative decomposition chain.

Electron-hole recombination is undesired during a photocatalytic process because it is competitive with charge separation and transfer mechanisms on which photocatalysis is based. They are responsible of contaminants degradation.

Recombination processes are induced by the presence of impurities or defects into the crystal. Conversely, the presence of surface defects allows the photogenerated pair to initiate the reaction longer. In this way electrons can be transferred to the reactants adsorbed onto the surface.

Titanium ions can be trapped in the form of Ti(III) instead of Ti(IV) because of the presence of some trapping centers on the surface. $Ti^{3+}OH$ attracts holes and it can act as a recombination center. Trapped electrons lifetime could increase up to 500 ms [22] enhancing the photocatalytic activity. Holes can bind OH^- surface group leading to the formation of $O^{\cdot-}$ or OH^{\cdot} . [22]

Fig. 2.2 shows the fate of the photogenerated pair and the relative timescales of reactions that can occur.

A way to promote charge separation is to dope the catalyst and prepare nanosized crystals.

Photocatalytic efficiency depends on [23]:

- Light intensity and wavelength;
- Concentration of the organic compound and catalyst load in water: the generation of electron-hole pairs is enhanced by adding more powder but if its amount exceeds a certain limit, problems in penetration of the light arise.
 - pH: it affects the surface charge of the catalyst dissolved in water and results in different ways of adsorption;
 - Addition of extra oxidants: in this case we have focused on the usage of H_2O_2 stoichiometric amount following the mineralization reaction reported by Malato.[24]

Hydrogen peroxide provides more traps for the electrons by hindering the recombination of the photogenerated pair; this strong oxidant agent results as OH radicals generator;

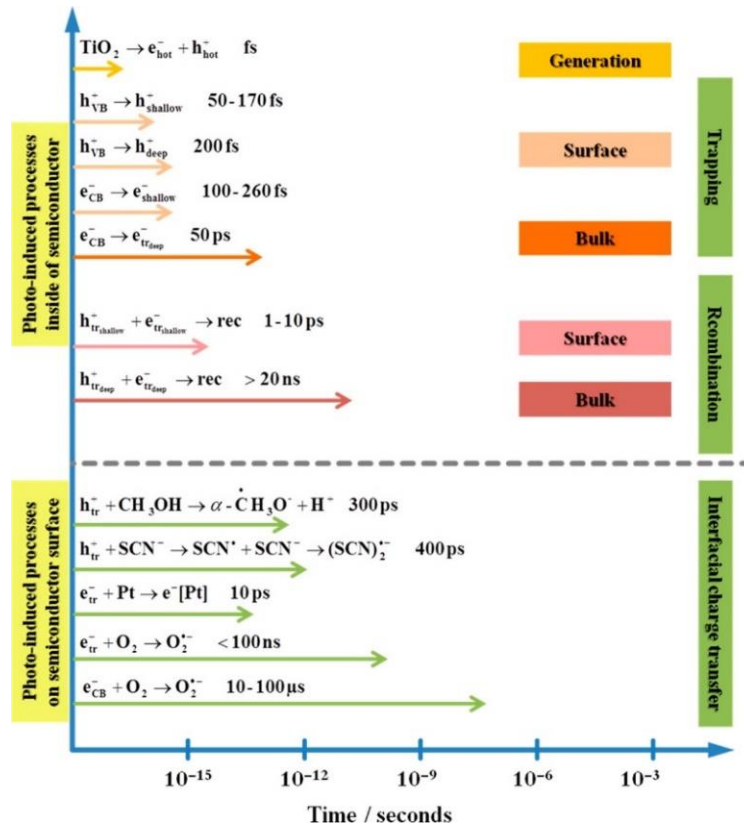


Figure 2.2 Reaction steps in TiO₂ photogenerated pair and relative time scales. (partially modified from ref. 22)

2.2 Materials for photocatalytic applications

The most used catalyst in photocatalytic applications is, undoubtedly, the titanium dioxide thanks to its stability and the high oxidizing nature of its photogenerated holes.[20]

It is a crystalline and white powder which is particularly effective if it is irradiated by UV rays based on its band gap which is relatively large (3.0-3.2 eV)[25]. It is economic and very efficient in photocatalytic processes. It is also used as a pigment for several products (foodstuffs or toothpaste etc.) so it is still available in a great amount.

Different materials show photocatalytic properties (TiO₂, ZnO, SnO₂, CdS etc). They are suitable for photocatalytic applications thanks to the biocompatibility. However, some of them are not enough efficient or stable to be applied. The semiconductor charge carrier is governed by the mutual position of its bands and the value of the redox potential of the photogenerated pair.

Other photocatalysts result to be less stable than titanium dioxide if they are exposed to air and the undergo degradation easier^[26]:

- ZnO: it has a low energy band gap that theoretically enhances the photocatalytic degradation of organic compounds in water solution but it forms a Zn(OH)₂ passivating layer that affects its properties. [27]

- SnO₂: it has a high energy band gap that doesn't promote the generation of the photogenerated pair.
- WO₃: it has good photocatalytic properties.

Photocatalytic activity of a catalyst depends on which conditions (chemical or physical) are chosen for the reaction to be led:

- Catalyst load
- Temperature
- pH

Degradation kinetics of organophosphorus pesticides is sensitive to the choice of the catalyst.

If peroxides are added to TiO₂, the catalyst is able to degrade and mineralize dimethoate (used as insecticide) completely instead of ZnO[13],[28]. O₂ in aqueous solution has a low solubility. In order to improve the photocatalytic efficiency of the system hydrogen peroxide can be added in a small amount. H₂O₂ enhances OH[·] production rate thanks to its higher oxidizing potential. [29]

2.3 The effect of doping

TiO₂ is well activated only if it is irradiated by UV rays. This is an issue that occurs if a low percentage of solar energy is available. Its photoinduced activation is promoted only if the catalyst surface is irradiated by a light beam with a wavelength larger than 388 nm (UV light). [30]

TiO₂ doping is a method used to reduce the band gap of the catalyst. Doping consists of the introduction of some heteroatoms into the solid crystal lattice. So, TiO₂ can be doped by using transition metals (typically V, Mn, Fe, Ni) or non metals (C, N, S). [31]

Non metals ease the quantum leap because they provide discrete states nearby the valence or conduction bands (Fig 2.3) [32]. N_{2p} states are energetically close to O_{2p} states leading to a band gap restriction [33]. By using non metals a red shift in light absorption is provided.

Noble metals are also used to dope titania. Ag reduces the semiconductor bandgap by promoting wavelength absorption in the visible region. Ag is able to prevent electron-hole recombination.

In order to insert a foreign ion into TiO₂ crystal lattice some crystallographic criteria are to be considered: ionic radius size and valence. Cations having very different ionic radius and valence from those of Ti(IV) cannot enter the lattice. If an ion with a valence number less than 4 is used to dope titania, it enhances the polymorphic transformation because of the formation of some oxygen vacancies. On the contrary, if an ion with a valence larger than 4 fills the lattice the transformation is slower. That is because of the reduction of the oxygen vacancies and the formation of Ti(III) interstitial ions. [31]

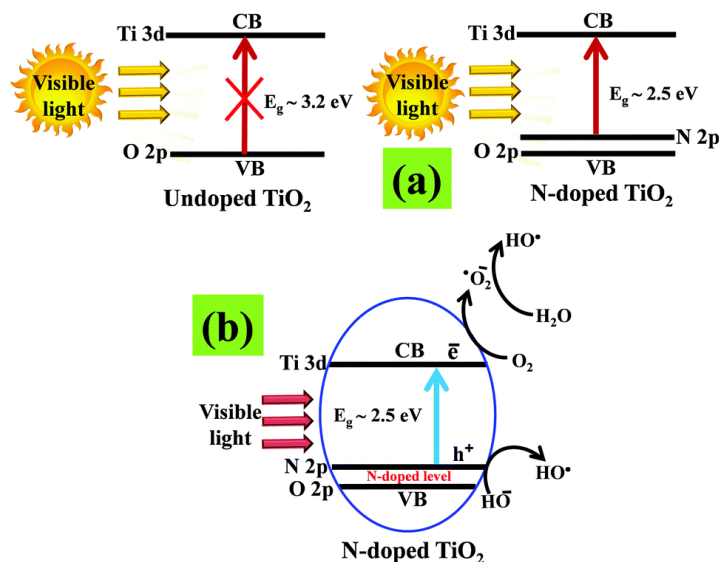
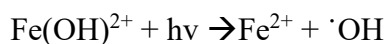


Figure 2.3 Introduction of energy discrete states near TiO₂ valence band after N doping (modified from ref 32)

Doping with Fe(III) leads to a decrease of the phase transition (anatase to rutile) temperature. Ferric ions insertion provides the formation of several oxygen vacancies enhancing water adsorption. OH groups onto the catalyst surface improve the photocatalytic activity. Fe³⁺ and Ti⁴⁺ have similar ionic radius sizes (respectively 0.64 Å and 0.68 Å.) That is the reason why ferric ions can be easily inserted into TiO₂ crystal lattice. Ferric NPs are smaller than pure TiO₂ ones, resulting in a higher surface area.[34]

If Fe doped TiO₂ is used during photocatalytic tests, Fenton or Fenton-like reactions can occur depending on the presence of Fe²⁺ or Fe³⁺ ions in the solution, reacting with H₂O₂ and light to generate radicals. The mechanism of a Fenton reaction is shown below:



It refers to a homogeneous Fenton process and presents a drawback: after the wastewater treatment is finished the sludge containing ferrous ions has to be discharged. In order to avoid it, a heterogeneous photo-Fenton process has been developed resulting with Fe oxides deposition on catalyst surface. [35]

Photo Fenton like reaction involves ferric ions combined with UV light and H₂O₂. Fe³⁺ ions are present in a hydroxylated form and they are continuously reduced to Fe²⁺ [36]:



2.4 TiO₂ photocatalysis

Because of its oxygen deficiency TiO₂ belongs to the n- type semiconductors class and it is the most studied photocatalyst. Some of its features are listed below: [37]

- transparency in visible region
- high porosity
- high superficial affinity with reagents
- low cost
- chemical inertia, non toxicity, biocompatibility

TiO₂ is present in three different polymorphs: anatase (tetragonal), rutile (tetragonal), brookite (orthorhombic).

The geometry of these polymorphic structures can be easily described by using a octahedral structure in which titanium Ti(IV) is coordinated to six oxygen atoms. The three crystalline forms differ for the assembly and distortion of the octahedral chains.

Octaedra in anatase phase share vertices while in rutile phase the edges. Vertices and edges are both shared in brookite phase. Polymorphs structures are shown in Figure 2.4 [38] and cell parameters TiO₂ are shown in Table 2.1 [39].

Rutile is the most thermodynamically stable phase. It consists of distorted octahedra sharing two edges. Anatase is metastable but it is the most used in technological applications thanks to its good photoactivity. Anatase to rutile phase transformation occurs when the temperature exceeds 600°C. The relative stability of a phase can be inverted when the particle size decreases. Surface stress and free energy depend on particle size. Anatase has the lowest surface free energy. When particle size is less than 11 nm anatase is stable, while brookite is stable in a dimensional range from 11 to 35 nm. Rutile phase becomes stable when particle size is larger than 35 nm. [40][41]

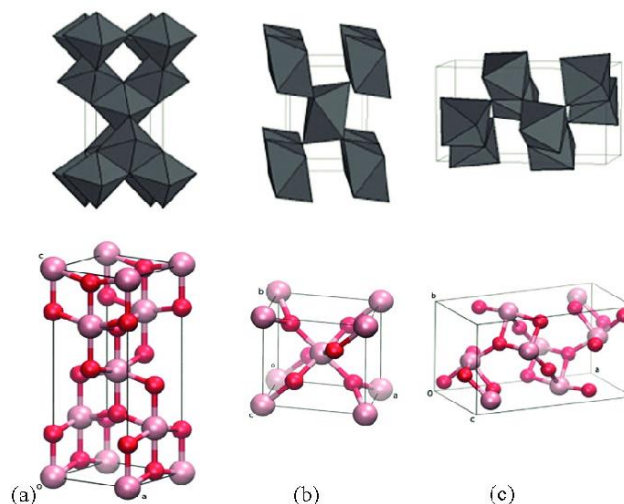


Figure 2.4 Titanium dioxide polymorphs structures: (a) anatase, (b) rutile, (c) brookite. (partially modified from ref. 38)

Optical absorption measurements showed that the E_g of rutile (3.03 V) is lower than the anatase and brookite ones (~3.2V). Anatase is a semiconductor with an indirect band gap whereas rutile and brookite have direct band gaps. It results in a longer lifetime of the photogenerated pair for the anatase phase in which the direct transition of the electrons from CB to VB is strictly forbidden. Photogenerated electrons in the anatase phase have the

lightest average mass leading to a fast migration of the pair from the interior to the particle surface. That is why anatase TiO₂ shows a low recombination rate [42]

Table 2.1 TiO₂ cell parameters. Data collected from Ref .38

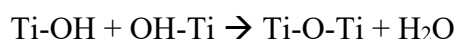
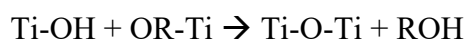
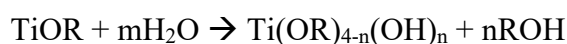
Properties	Anatase	Rutile	Brookite
Crystal bulk structure	Tetragonal	Tetragonal	Orthorhombic
Atoms per unit cell (Z)	4	2	8
Crystal size (nm)	<11	>35	11-35
Lattice parameters (nm)	a 0,3785	a 0,4594	a 0,5436
	b 0,3785	b 0,4594	b 0,9166
	c 0,9514	c 0,2959	c 0,5436

2.5 TiO₂ synthesis methods

TiO₂ properties are highly affected by the preparation methods. Titania is commonly used for a wide range of applications (environmental remediation first) and in order to fulfill NPs specific features (such as particles size and shape) different routes can be followed to synthesize this metal oxide. A short list is provided below.

2.5.1 Sol gel route

TiO₂ nanoparticles (NPs) are synthesized starting from an aqueous solution in which some titania precursors are dissolved. They are generally alkoxide that undergo two main reactions in water: hydrolysis forms a stable dispersion of colloidal particles whereas polycondensation forms a gel. These reactions in series result in the formation of oxopolymers[43] that in turn are transformed into metal oxide. Gel may be formed by agglomeration of colloidal particles or by using linking polymer chains. This process is largely preferred if both NPs size and shape have to be controlled and it can be used at low temperatures. A summary of sol gel chemistry is shown below:



2.5.2 Hydrothermal route

This synthesis route is led at high temperature (usually above the boiling point of water) and pressure (between 1 and 10000 atm) into an autoclave. It results in the formation of crystals starting from metal precursors that could be moderately insoluble under room

conditions. High pressure enhances the interaction of the precursors used during the synthesis and NPs degree of crystallinity increases as temperature increases. Hydrothermal route can only occur under supercritical conditions[44]. This method is preferred if the aim is to obtain nanotubes.

2.5.3 Solvothermal route

If a specific solvent instead of water is used during the synthesis the route is referred to as solvothermal. Temperature and pressure chosen to lead the synthesis are generally higher than the hydrothermal route that is solvent with higher boiling point can be used. In this way both size and shape can be controlled easier. NPs obtained by this method have a defined crystallinity and a smaller size.

2.5.4 Reverse micelles route

If a surfactant is dissolved in a solvent with a concentration higher than its critical micelle concentration (CMC) a micelle is formed. Micelles formation process is referred to as self assembly. Reverse micelles are generated in apolar solvent and they appear as globular aggregates. They behave as a microreactor to obtain TiO₂ NPs with a good size-polidispersity[45]. Procedure is similar to that described for sol gel route but in this case hydrolysis reaction occurs in a reverse micellar environment whereas polycondensation (i.e. the formation of the gel) is due to inorganic polymerization[45]. Rates of hydrolysis and condensation can be controlled with this route by acting on the frequency of the intermicellar exchanges. Using a surfactant allows to control particle size because it prevents agglomeration.[46]

3. Pesticides

The term pesticide is used to speak about all the chemicals able to control, limit and destroy living organisms considered to be harmful[47]. This class of chemical is also used to hinder their development into the soil. It involves plant crops protection and veterinary use products.

Pesticides are poisons with a specific function they are used to protect crops by pests' attacks (insects and mites) and pathogenic agents (bacteria, virus, fungi), to ensure high standard quality in agriculture production. Modern regulations have been imposing limits on their usage and applications because of their high toxicity. A more precise distinction collects pesticides depending on their usage and mechanism of action into the soil[48]:

- Contact pesticides: they are fixed on the external surface of the vegetal part which is treated;
- Systemic pesticides: they diffuse in vegetal tissues because they are carried by plant lymph;

Several aspects affect the pesticides action[49]:

- Temperature: some systemic product is active only if a temperature higher than 8°C is reached. If the temperature exceeds 28°C the plants physiological functions decrease leading the pesticide to be less effective; high temperature makes chemicals evaporation faster;
- Rain: the active principle has to enter into the foil and if it rains this process is hindered. On the other hand, if the pesticide is applied directly onto the soil the rain action is synergic;
- Light: it enhances photosynthesis and the diffusion of systemic pesticides;

According to the ISPRA report[50], more than 259 different chemicals have been detected in Italy . Herbicides class is still the most present in surface water because of its direct application onto the soil. Peaks of its usage have been detected during rainy periods in Italy. Rain carries herbicides faster in groundwater[50].

3.1 Persistent organic pollutants: which pesticides are included?

Persistent pollutants (POPs) damage human health and environment. Stockholm convention is based on the precautionary principle and aims at the safe elimination of the chemicals listed as well as the reduction in their production and usage. EU issued a public document on the 14th October 2004 (2006/507/CE)[51]:[50] in which a POPs definition is provided and some regulations concerning production, import-export policy of these chemicals are stated. POPs are chemicals resistant to degradation. They accumulate in living organisms, are carried by air, water and migratory species. Convention mainly discusses 23

persistent pollutants(12 of them are shown in the Table 3.1 below)[52]: they can be accidentally produced or may come from some sources such as incinerator.

Table 3.1 List of 12 chemical POPs discussed during the Stockholm convention (data collected from ref. 52)

12 POPs	
Intentionally produced	Unintentionally produced
Aldrin	PCDDs
Chlordane	PCDFs
DDT	PCBs
Dieldrin	Hexachlorobenzene
Endrin	
Eptachlor	
Hexachlorobenzene	
Mirex	
PCBs	
Toxaphene	
Elimination of production and use	Minimization and, where feasible, elimination

3.2 Contamination level in EU and Italian ground water

The presence of some pesticides in groundwater raises the question concerning all the possible negative impacts on human health and environment. By comparing concentration values of contaminants detected in water body with those stated by the regulations, it is clear that 23.9% of the analyzed samples withdrawn by surface water basins, and 8.3% of samples withdrawn by groundwater basins show higher concentration than the limit.

Standard quality is based on water toxicity levels for representative species of aquatic environment. Concentration limits are expressed as annual mean values and maximum allowable concentration. Every pesticide can be present in water with a maximum concentration of $0.1 \mu\text{gL}^{-1}$ whereas pesticides mixtures must not exceed $1 \mu\text{gL}^{-1}$ (as stated in DM 56/2009).[50]:[53]

In Figure 3.1 are listed the most detected chemicals in ground and surface water during 2015-2016 as reported in ISPRA report.

3.3 N-containing organic compounds

Aldicarb ($\text{C}_7\text{H}_{14}\text{N}_2\text{O}_2\text{S}$) is present mainly in surface water whereas atrazine ($\text{C}_8\text{H}_{14}\text{ClN}_5$) in groundwater. Glyphosate ($\text{C}_3\text{H}_8\text{NO}_5\text{P}$) and its degradation product (it is a metabolite named Ampa) are the most detected herbicides in groundwater: its concentration is higher than the limit in 24.5% of samples undergone the analysis and in 47.8% of Ampa ones.

Among the herbicides metolachlor exceeds its limit concentration together with its degradation product (named metolachlor-esa).

Gliphosate was widely used as a diserbant until it was discovered that its usage had a severe impact on human health (as reported in the news[54]). It has low toxicity, high effectiveness and fast degradability into the soil: it is produced by several companies on market because it is not covered by patents anymore [55]

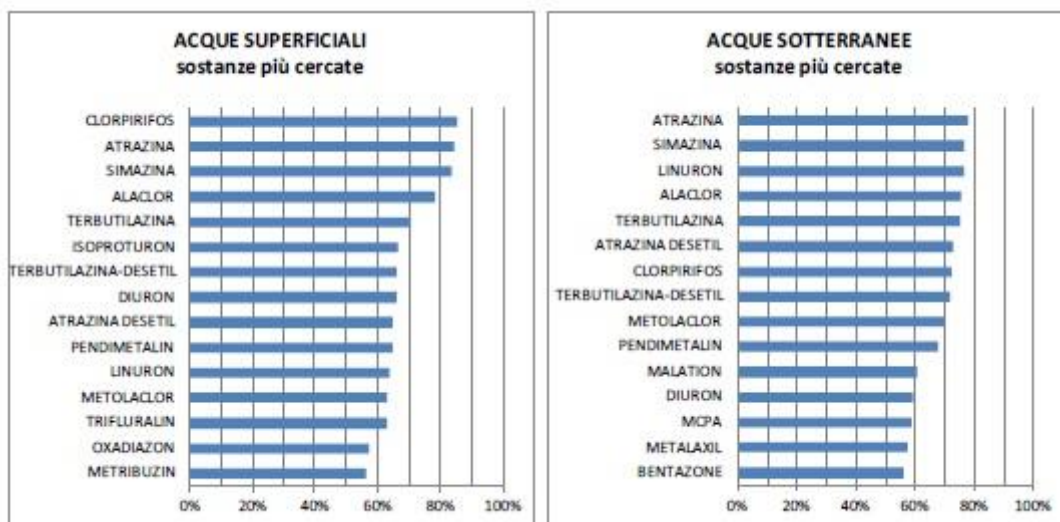


Figure 3.1 Most detected chemicals in Italian ground and surface water during 2015-2016. From Ref. 50

This work is focused on the study of a photocatalytic system for the abatement of nitrogen organic compounds. Before discussing of these new unconventional methods using light in combination with others oxidizing agents (i.e. H_2O_2 or Fe/H_2O_2 Fenton like reactions) it is better to list some nitrogen sources in the environment:

- Nitrogen is present in nature in the form of aminoacids, proteins of humic substances;
- Urea and ammonia are produced by human metabolism;
- Most of the organic compounds come from chemical industries: nitrous acid derivatives and azodyes.[56]

Nitrogen organic compounds are mainly present in surface water with a variable concentration between 0.5 and 2.5 mgL^{-1} .

3.3.1 Phenylurea family

Pesticide which we focus our attention on in this work is N-phenylurea. Its chemical structure is shown below (Fig. 3.2).[57]

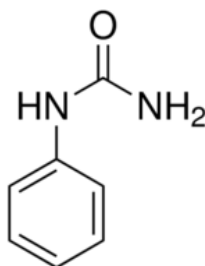


Figure 3.2 N-phenylurea chemical structure (modified from Ref 58)

It is also well known with the name phenylcarbamide due to the functional groups it is made of: phenyl group $-C_6H_5$ and carbamide $-NH_2CONH_2$. It consists of a wettable powder with a solubility in water of 10 mg/mL.[58] It can be found on the market with several commercial formula (Diuron, Bromuron, Fenuron). The latter are mono or polysubstituted phenylureas.

Chemicals data in the next steps are collected for similar compounds involved in phenylurea family.

Our work is mainly aimed at studying and discovering any possible degradation pathway of the molecule by using light with different wavelengths (i.e UV or solar) by exploiting photocatalytic phenomena and the interaction between the dissolved substrate (phenylurea) and the powder (titanium dioxide).

Phenylurea herbicides are distributed under several commercial names depending on the ring halogens substituents (such as Diuron, Bromuron, Fenuron or Isoproturon).[59]

Diuron ($C_9H_{10}Cl_2N_2O$) is the most used pesticide of this class. It is widely studied in literature and it has been detected in water and in soil as well. It is used worldwide from Japan to Alsace region in France (Europe) with an average concentration of $3.05 \mu\text{gL}^{-1}$. (Fig. 3.3). [60]

Concentrations ($\text{pg}\cdot\text{m}^{-3}$) of different pesticides in the region of Alsace (France) at the period between 2000 and 2003.

Pesticide	Sanusi et al. (2000)	Sauret (2001)	Scheyer et al. (2007)	Scheyer et al. (2008)
	n FD Min.-max. (average)	n FD Min.-max. (average)	n FD Min.-max. (average)	n FD Min.-max. (average)
Atrazine	9 690-51,260 (20030)	29 15 <LQ-794 (130)	23 13 <LQ-278 (150)	9 6 <LQ-688 (300)
Diffufenican		29 24 57-1250 (214)	23 14 <LQ-462 (164)	9 8 <LQ-96 (72)
Diuron	9 9 870-5850 (2049)		23 18 49-669 (201)	9 9 48-1534 (455)
Trifluralin	9 743-3800 (2118)		23 23 <LQ-179 (50)	9 9 <LQ-182 (90)

Figure 3.3 Pesticide average concentration (data reported particularly for Diuron) in Alsace region (France). (modified from ref. 57)

3.4 Degradation pathways for phenylureas

The most effective method to get the abatement of these N-containing organic compounds is represented by the advanced oxidation processes (AOPs). Fig. 3.4 shows any possible step during the pesticide phototransformation by using titanium dioxide as solid substrate. [23] The degradation efficiency depends on the method applied and the nature of the organic compound as well (i.e. aliphatic or aromatic compounds and their oxidation states). It consists of a *in situ* application method leading to the generation of radical species that are highly reactive and provides the mineralization of the organic compound following the next reaction [23]:



Mineralization of nitrogen organic compounds involves the formation of several species (i.e. NO_3^- , NH_4^+ and elementary nitrogen). The first two species are considered to be still harmful to humans whereas the latter does not affect the environment.

Aliphatic compounds undergo reactions to the formation of NH_4^+ . Hydroxylated amines are converted to nitric ions in water. [56]

The degradation pathway of some N-containing aromatic compounds is more complex. As before, Diuron molecule has been tested in several studies. It undergoes degradation following these steps [61]:

- Methyl groups of the lateral chains are oxidized
- Aromatic ring undergoes hydroxylation
- Dechlorination; this step depends on the nature of the substituents on the aromatic ring. The molecule we focused on this work is the N-phenylurea which is not substituted so it does not undergo this reaction.

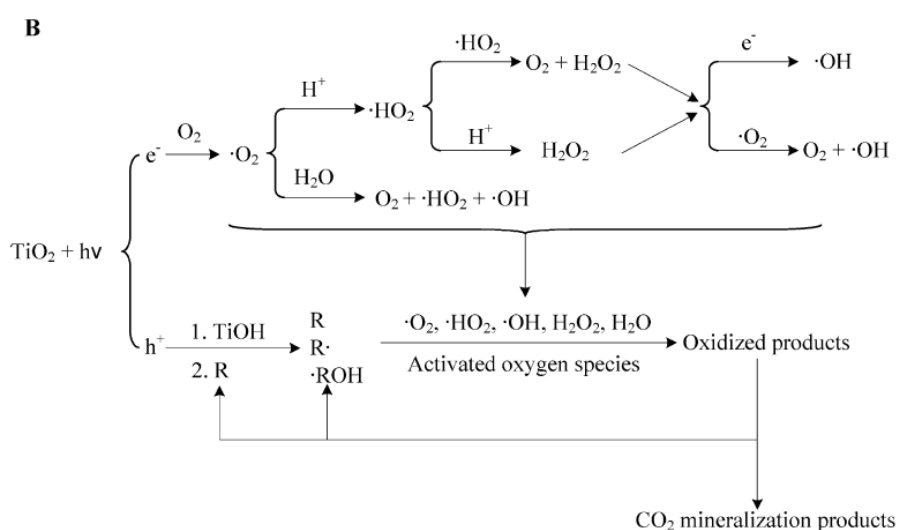


Figure 3.4 Reactive species and product generated during pesticide phototransformation by TiO_2 . From Ref. 23

Phenylureas are used because they inhibit photosynthesis.[62] They undergo decomposition if they are hit by UV light or if they are dissolved in a heterogeneous system together with a TiO₂ based catalyst. Thanks to the nature of TiO₂ (it is a metal oxide) the degradation pathway can be led both in acidic or alkaline medium.

They may undergo photolysis of C-X bond (if they are substituted), photoelimination, photooxidation (it is referred to as Norrish type II reaction) and photorearrangement.[59]

Phenylureas are considered to be persistent in soil and water because of their long half-life: respectively 30-40 and 200 days.

Adsorption in dark conditions and UV light irradiation only are not effective for the degradation of phenylureas. Their removal efficiency increases if we add 1 gL⁻¹ TiO₂ (it is the concentration used during almost all the photocatalytic test in this work). The degradation kinetics can be simply described by using a Langmuir-Hinshelwood model. By plotting ln(C/C₀) on the y-axis vs time on the x axis a straight line results as Figure 3.5 shows [63]:

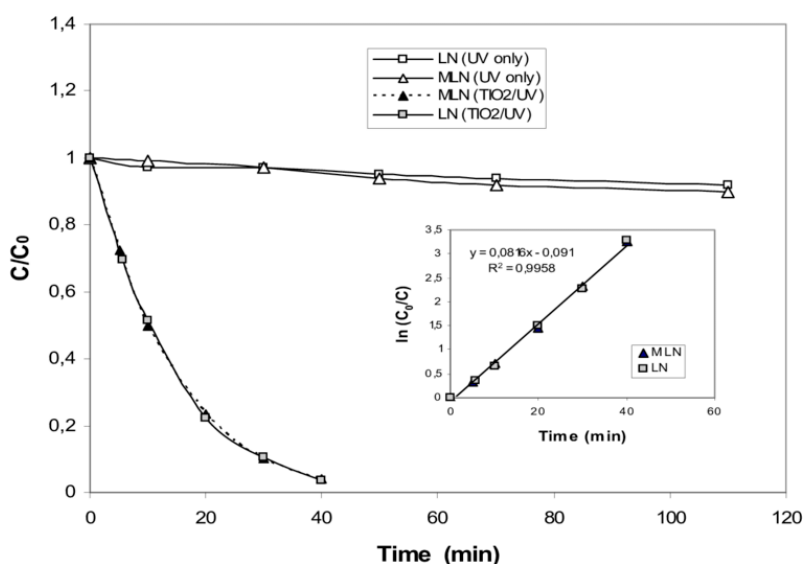


Figure 3.5 Pseudo first order kinetics for linuron and monuron during their transformation by UV/TiO₂ combined action. From Ref. 63

Data collected into the plot suggest that the degradation rate of a phenylurea pesticide follows a pseudo first order kinetics.

By using orbital theory, it can be shown that the aromatic ring is attacked by OH radicals and the alkyl groups attached to the ring (no matter if in -ortho or -para) have a high reactivity. In this way the urea group attached to the ring can react with the hole (h⁺) by leading to the molecule adsorption on the catalyst surface. The side chain of the molecule is the first part to be decomposed by the photocatalytic process.

The degradation pathway of a phenylurea pesticides can be summarized by: (i) the complete cleavage of the urea side chain; (ii) hydroxylation of parent molecules^[23]

This hypothesis can be supported by further analysis in the work of Lhomme et al (2006) where Chlortoluron degradation has been studied and a degradation mechanism has been listed[64]:

- OH radicals attack the methyl groups leading to the formation of hydroxylated or carboxylated compounds
- The aromatic ring is hydroxylated

Finally, it can be stated that OH radicals preferentially attack two sites: the methyl groups or the aromatic ring.

By using LC-MS analysis on a 2 hours irradiated sample some organic aliphatic parental compounds have been detected: methyl groups are mainly oxidized to formic acid that in turn is decomposed in acetic acid (as the last degradation step). The only way to get acetic acid by the molecule degradation is the rupture of the aromatic ring (this decomposition step occurs only after several hours of irradiation).

Most of the nitrogen in the untreated pesticide results in NH_4^+ after some hours of irradiation. This ionic species is released meanwhile formic acid is produced (it suggests that this couple of reactions occurs in the first step of degradation);

NO_3^- formation occurs after several hours of irradiation and it is not a byproduct of the NH_4^+ oxidation.

Similar results are shown in the work of Pramauro et al (1993) where the photocatalytic degradation of Monuron in aqueous dispersion is studied[65] Contaminant has been mineralized to CO_2 but the oxidation of nitrogen source to NO_3^- is the kinetic (pseudo first order) rate determining step passing by the formation of ammonia. Ammonium ions can be detected by following the characteristic adsorption band at 400 nm in a UV-Vis spectrum.

The first degradation step involves hydrolytic processes as usual. The formation of NH_4^+ can be achieved because of the presence of primary amines. Next steps of degradation pathway involve the appearance of hydroxylated products after ammonia underwent photooxidation over the solid catalyst. By HPLC analysis many hydroxylated intermediates have been detected such as phenylisocyanate or phenylformamide.

Figure 3.6 shows several degradation pathway phenylurea herbicides may undergo.[66]

Amine-Khodja et al (2004) [67] studied the photochemical behavior of some phenylurea herbicides. They stated that for unhalogenated phenylureas there is a preferential pathway by which the homolytic cleavage of carbamide occurs followed by a radicalic rearrangement of the excited molecule.

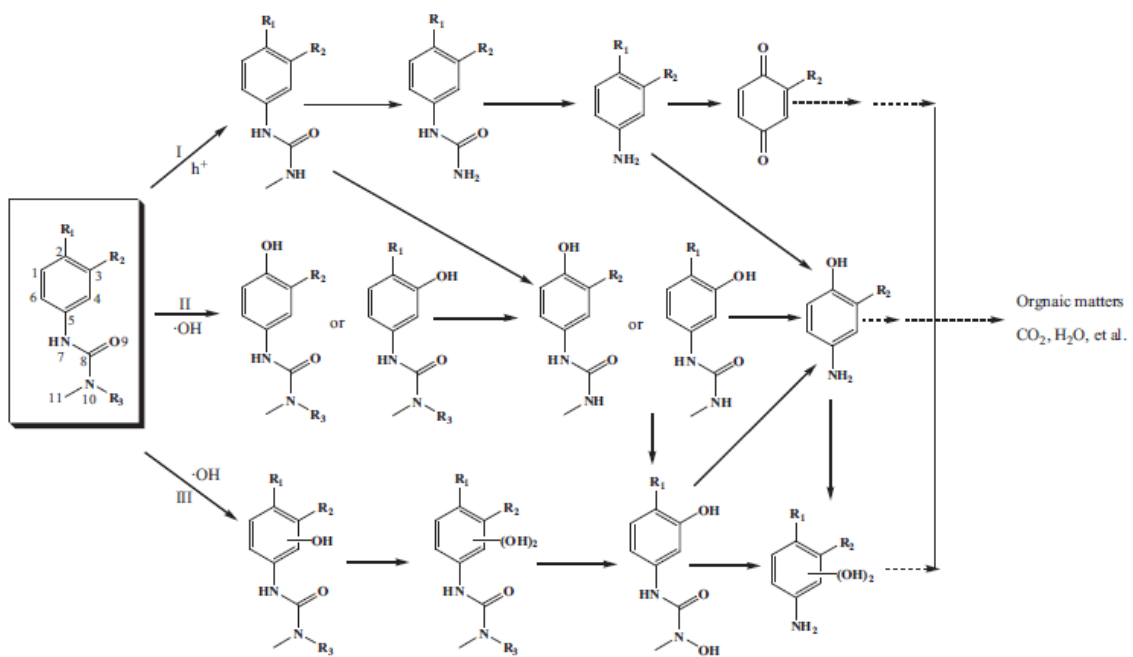


Figure 3.6 Degradation pathways phenylureas may undergo by phototransformation. From Ref 66.

4. Catalyst characterization

4.1. Techniques used in this work: summary

Mixed phases TiO₂ catalysts were synthesized and they were characterized by using the following techniques:

- X-ray powder diffraction: used to investigate powders structure in terms of phases identification and crystallite size. Information obtained by using this technique are referred to the bulk composition of the catalyst.
- N₂ adsorption/desorption isotherms: are used to determine specific surface area (SSA) of each powder catalyst. This method is based on N₂ adsorption/desorption at constant temperature (77K i.e nitrogen liquefaction temperature). Average pore diameter can be computed as well by BJH method.
- UV-Vis spectroscopy is used to follow qualitatively the degradation path of N-phenylurea. The study focused on the attribution of the absorption bands of the molecule and their relative shift over time. Besides diffuse reflectance measurements have been performed by means of an integrating sphere to compute energy band gap of the powders.
- FTIR: used to investigate potential powder contamination by some precursor that have not been reacted during the synthesis.
- TEM: used to observe morphology of the catalyst and to have a prediction of particles size by using different resolutions.
- DLS (dynamic light scattering): used to measure ζ potential and particle size distribution with the aim of predicting colloidal stability.

4.2 X-ray Powder Diffraction (XRD)

4.2.1 Theory

X ray diffraction is based on Bragg's law and the interference between photons and a crystal lattice with a proper spatial ordering.

A copper cathode is bombarded by fast electrons to produce X rays whose wavelength depends on the anticathode material.

A crystal can be seen as a periodic system consisting of equidistant and parallel atoms. Interatomic distances are measured in Å (10^{-10} m) and there are comparable to X rays wavelength.

X rays are produced in tubes in which an anelastic hit between high energy electrons beam (coming from a heated filament) and a metal (anode) occurs.

Anodic radiation emitted consists of two components[68]:

- Characteristic lines
- Bremsstrahlung radiation (usually filtered)

Bragg's law

It is used to correlate radiation wavelength to the interplanar distance passing by the measurable diffraction angle θ . It is based on interference phenomena between rays that are diffracted by parallel planes of a crystal having Miller index (h,k,l).

Constructive interference is possible only if Bragg's law (Eq. 4.1) is satisfied.

$$n\lambda = 2d\sin\theta \quad (4.1)$$

Where:

λ is the incident radiation wavelength;

d is the interplanar distance;

θ is the diffracted semi-angle;

n is an integer

XRD diffractometers are based on Bragg-Brentano geometry[69] (Fig. 4.1). X rays source is fixed whereas sample and detector rotate with angular frequencies that are respectively θ/min^{-1} e $2\theta/\text{min}^{-1}$.

A nickel filter removes some lines from the spectrum in order to make incident radiation monochromatic.

Samples are generally analysed in form of powder in order to expose the largest number of crystalline planes.

This analysis produces an XRD pattern from which the following information are extracted:

- Angular position by which catalyst structure and phases composition can be determined;
- Peak intensity: relative abundancy of the phases and plans preferential orientation can be studied;
- Peaks profile by which crystallite size can be computed and stress state is shown;

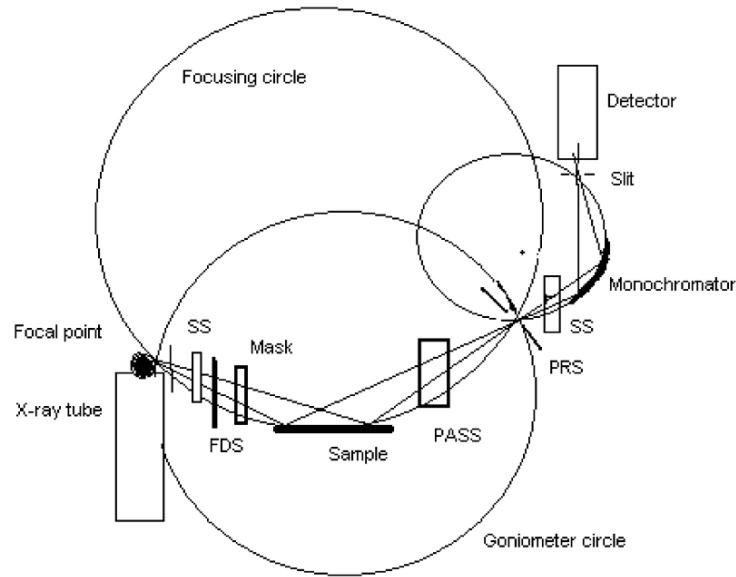


Figure 4.1 A schematic representation of a X-rays diffractometer with Bragg-Brentano geometry (partially modified from ref. 69)

Crystallites have an average size in the range of nm. Scherrer equation (Eq. 4.2) can be used to compute the average size and has the form:

$$\tau = \frac{K\lambda}{\beta \cos\theta} \quad (4.2)$$

Where:

τ is the average size of the crystallite:

K is a shape factor (approximately 0,9)

λ is the incident radiation wavelength

β is referred to as FWHM (full width at half maximum)

θ is the diffracted semi-angle;

Due to mechanical distortions inducing peaks enlargement Debye Scherrer equation is conservative.[70]

A more detailed approach, based on Williamson-Hall plot, has been used to compute crystallite size by using High Score Plus software.

4.2.2 Data acquisition

XRD patterns (Fig. 4.2) have been recorded by means of a XPert Philips diffractometer equipped with Cu $K\alpha$ radiation (2θ angle range: 10° - 90° , step scan: 6s). Phase composition of synthesized powders have been analysed by means of Rietveld refinement.

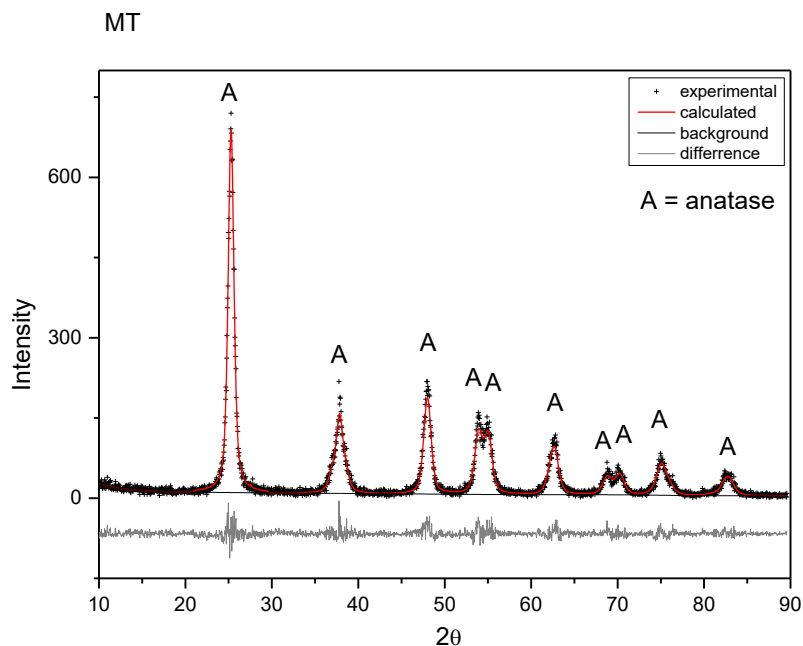


Figure 4.2 Mesoporous titania (calcined at 450°C) XRD pattern

4.3. BET analysis

4.3.1 Theory

Porous materials are characterized by deep cavities known as pores. Pores structure has been studied by means of the shape of the hysteresis curve after the adsorption process and several geometries have been characterized such as cylindrical, conical, slit shaped or ink-bottle.

Characterization of properties based on porosity and specific surface area (SSA) can be led by means of gas adsorption. This method is specifically applied to surface area and pore volume calculations and to particle size distribution (PSD) as well.

Adsorption is referred to as the mechanism by which a penetration of a gas occurs to enter a solid surface. Two phases are involved into the process: adsorbent (the solid phase on which adsorption occurs) and adsorbate (gas adsorbed on the solid). Depending on the nature of the interactions between the two phases, physisorption or chemisorption can occur.

Physisorption (physical adsorption) is generally preferred thanks to its reversibility[71].

In the case of physical adsorption, the interaction forces between molecules are dispersive (van der Waals forces)

Gas phase may adsorb on the solid forming a multilayer as its relative pressure increases..

Adsorption isotherms (Fig 4.3) are curves by which adsorbed gas quantity is related to its relative pressure.[72]

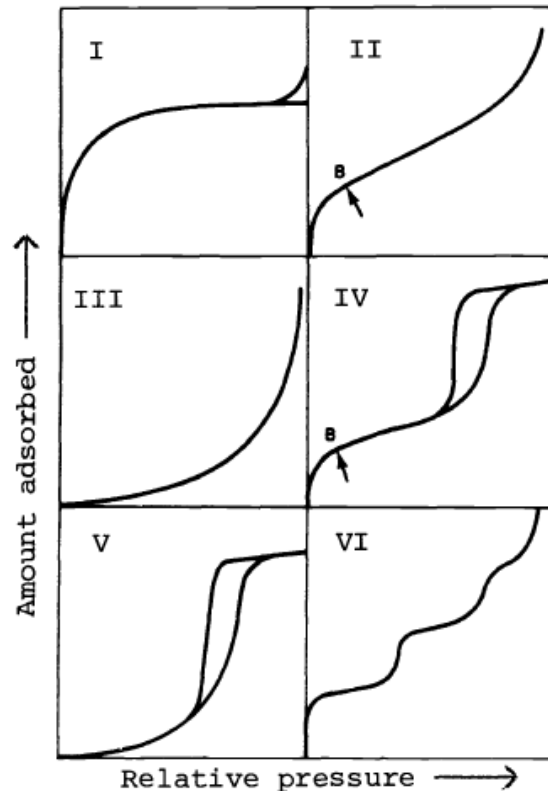


Figure 4.3 IUPAC classification of adsorption/desorption isotherms by using nitrogen at -196°C (modified from ref. 72)

IUPAC provides the following definitions:

- Type I: describes microporous materials. At low relative pressure (p/p°) the number of moles of the adsorbed gas increases rapidly until a knee is reached. The curve becomes flat although the pressure increases when the solid surface is not able to adsorb. Gas liquefaction occurs as saturation is reached;
- Type II: describes adsorption on macroporous or non-porous solid. It indicates the formation of an adsorbed monolayer whose thickness increases progressively with the relative pressure until $p/p^{\circ}=1$. The knee on the plot is matched to the value of the pressure at which the monolayer is formed.;
- Type III: has a convex shape with no knee. It is typical of weak interactions between adsorbent and adsorbate.
- Type IV: is characterized by an initial trend similar to that of Type II. It tends to a constant value as the relative pressure increases. It shows both adsorption and desorption isotherms. It is typical of mesoporous materials. During adsorption gas molecules fill the monolayer until it is completely filled at a relative pressure $p/p^{\circ}=0,95$. Capillary condensation can occur even if $p < p^{\circ}$.

- Type V: indicates weak interactions between adsorbent and adsorbate as Type III does.
- Type VI: is typical of systems in which the solid surface is morphologically and energetically uniform and porosity is not present.

Porous materials are characterized by some parameters:

- specific surface area (SSA in m²/g);
- pore volume (in cm³/g): is the sum of the volume of micro and mesopores;
- particle size distribution (PSD).

Based on adsorption mechanism, at low values of p/p^o the adsorbent gas fills micropores. That is why by using these data pore volume and pore size distribution (PSD) are obtained. The region of the plot corresponding to the monolayer formation can be used to compute the specific surface area (SSA).

4.3.2 Adsorption models

4.3.2.1 Langmuir model

It is based on the assumption that only a gas monolayer can be formed on the solid surface. Besides, all the active sites are isoenergetic, i.e. ΔH_{ads} (adsorption enthalpy) is constant. That is the reason why is commonly applied in the case of chemisorption. The collision between the molecule of the gas and the substrate is anelastic.

By knowing the surface area occupied by a single gas molecule (σ) and the value of V_m it is possible to compute the specific surface area as follows (Eq. 4.3):

$$S = \frac{V_m \sigma N_A}{m V_0} \quad (4.3)$$

Where

V_m is the quantity of the gas required to form a monolayer

σ is mentioned above

N_A is the Avogadro number;

m is the mass of the adsorbate in measured in g;

V₀ is the gas molar volume;

4.3.2.2 BET model

Brunauer, Emmett and Teller extended Langmuir's theory to multilayer adsorption. BET theory is based on a dynamic equilibrium between the vapor and the molecules adsorbed on the highest level of the multilayer.

A linearized equation used to describe the model is written below (Eq 4.4)

$$\frac{P}{V_a(P_0-P)} = \frac{1}{V_m C} + \frac{C-1}{V_m C} \left(\frac{P}{P_0}\right) \quad (4.4)$$

Where

C is a constant that is proportional to the adsorption heat of the first layer;

P₀ is the saturation pressure of the gas.

By plotting $\frac{P}{V_a(P_0-P)}$ on the x axis and $\left(\frac{P}{P_0}\right)$ on the y axis a straight line is obtained; $\frac{1}{V_m C}$ is its intercept and $\frac{C-1}{V_m C}$ is its slope.

BET model and experimental data fit in a narrow range of relative pressure with $0.05 \leq \frac{P}{P_0} \leq 0.35$.

Barrett-Joyner-Halenda (BJH) theory is a mathematical model used to study the pore distribution. This model is based on some hypothesis:

A pore can be described as a cylinder with a narrow layer "t" adsorbed to the wall and a liquid capillary[73] whose radius vary with the relative pressure by following Kelvin's equation assuming that pore are cylindrical.

A typical BJH plot shows the cumulative pore volume related to the pore radius.

A more intuitive data interpretation gives a sketch of the pore size distribution by plotting the ratio between the derivative of pore volume and of the radius with respect to the radius itself.

4.3.3 Data acquisition

A Micromeritics ASAP 2020Plus instrument has been used to obtain N₂ adsorption/desorption isotherms at -196 °C. Before the analysis powders have been outgassed for 1h at 120°C with a 5 °C temperature ramp. BET method has been used to compute specific surface area (Fig 4.4) and BJH method has been applied to the desorption branch of the isotherm to determine pore total volume.

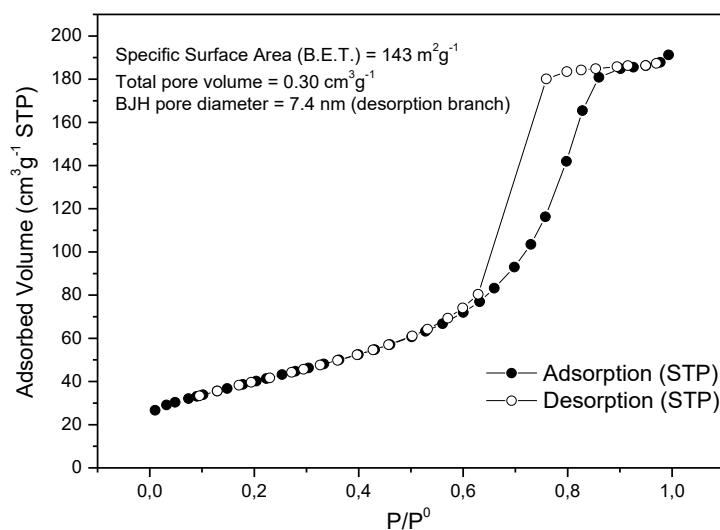


Figure 4.4 N₂ Adsorption/desorption isotherm (IV Type) of Mesoporous Titania calcined at 450°C. Pore total volume and mean pore diameter are computed by using BJH method. Data have been processed by using ASAP 2020Plus software.

4.4. UV-Vis spectroscopy

4.4.1. Theory

Spectroscopy studies the interaction between radiant energy and matter. In particular, molecular spectroscopy absorption is interested in absorption phenomena of light radiation in the region of the electromagnetic spectrum belonging to visible (400-800 nm) up to near UV (200-400 nm).

When a molecule is in the ground state its electrons stay on the lowest energy orbital. If a radiation hits the molecule with a sufficient energy to promote valence electrons transfer to higher energy levels an energetic transition occurs. This is the aim of this spectroscopic technique.

Electronic transitions (Fig. 4.5) are governed by the “selection rule” and involve generally three types of electrons[74]:

- σ : they are involved in single bonds. UV photons are not able to excite σ electrons so molecules belonging to this class are used as solvent during the analysis because they don't usually absorb. It is the case of alkanes;
- π : they are involved in unsaturated bonds. They can be excited easier than σ electrons that is they are able to absorb in visible region. Absorbance spectra in the visible region usually show the effect of delocalized π electrons. It is the case of aromatic compounds;

- n: they are free electrons (i.e. not involved in bonds) and are easily excited both in UV and visible region. It is the case of organic compounds containing nitrogen.

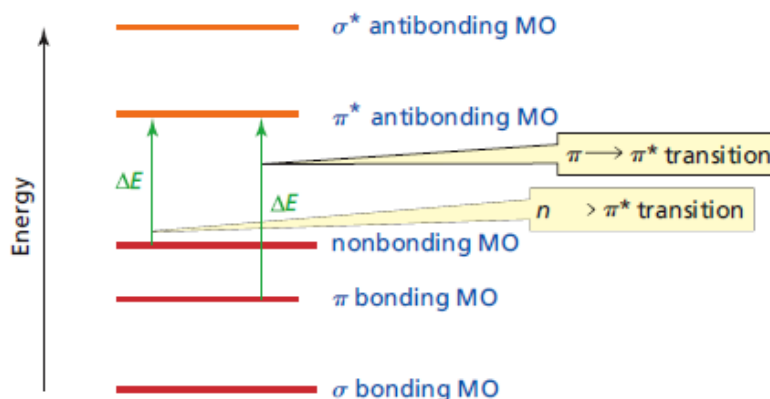


Figure 4.5 Energies associated to $n \rightarrow \pi^*$ and $\pi \rightarrow \pi^*$ electronic transitions (partially modified from ref. 74)

Because of the amount of the energy that UV-Vis radiation is able to transfer to the target molecule, only two electronic transitions are permitted: $n \rightarrow \pi^*$ and $\pi \rightarrow \pi^*$. They are listed in terms of increasing energy required to promote the transition itself. They both promote the valence electron transfer to π^* that is the antibonding molecular orbital. So, UV-Vis spectra are only produced by organic molecules that already have π electrons in their electronic structure.

The part of the molecule that is capable of absorbing radiations is called chromophore.

Absorbance spectroscopy is widely used in analytical chemistry to determine quantitatively the concentration of some organic molecules dissolved in any solvent by means of Lambert-Beer's law.

When an electromagnetic radiation hits a transparent medium it is partially reflected or refracted in the medium itself. The intensity of the refracted radiation decreases as light propagates.

Absorbance is defined as follows (Eq. 4.5):

$$A = \log \frac{I_0}{I} = \log \frac{I_0}{I} \quad (4.5)$$

Where I_0 is the intensity of the incident light; I is the transmitted intensity; $\frac{I}{I_0}$ is defined as transmittance.

Lambert-Beer's law (Eq. 4.6) relates the absorbance to the concentration of the analysed sample.

$$A = \epsilon \lambda c \quad (4.6)$$

- ϵ is the molar absorption coefficient measured in $\text{dm}^3 \text{cm}^{-1} \text{mol}^{-1}$;

- λ is the path length of the medium measured in cm;
- c is the concentration of the sample dissolved in a solvent (generally water);

Lambert-Beer's law provides a linear proportionality between the two quantities mentioned above only in a narrow range of concentration. Proportionality is not verified anymore as concentration increases. So, the law is valid only for dilute solutions.

4.4.2 Instrument description and data acquisition

The instrument used to determine the absorbance of a sample is the spectrophotometer (Fig. 4.6)[75]. A general description of the apparatus is given below. It consists of:

- Light source: the instrument is equipped with two lamps made of different materials. Tungsten light bulbs are used if the instrument works in the visible region otherwise (in the UV region) a deuterium light bulb is employed.
- Monochromator: a diffraction grating makes light monochromatic.
- Chopper: is made by three mirrors. The first one reflects the light, the second one (black) absorbs the light, the third one is drilled and transmits it.
- Sample cuvette: it can host a parallelepipedal cuvette with $\lambda=1$ cm;
- Detector: it is a photomultiplier made by a cathode covered by some alkaline metals to allow the complete wavelength range scanning from 185 nm to 900 nm.

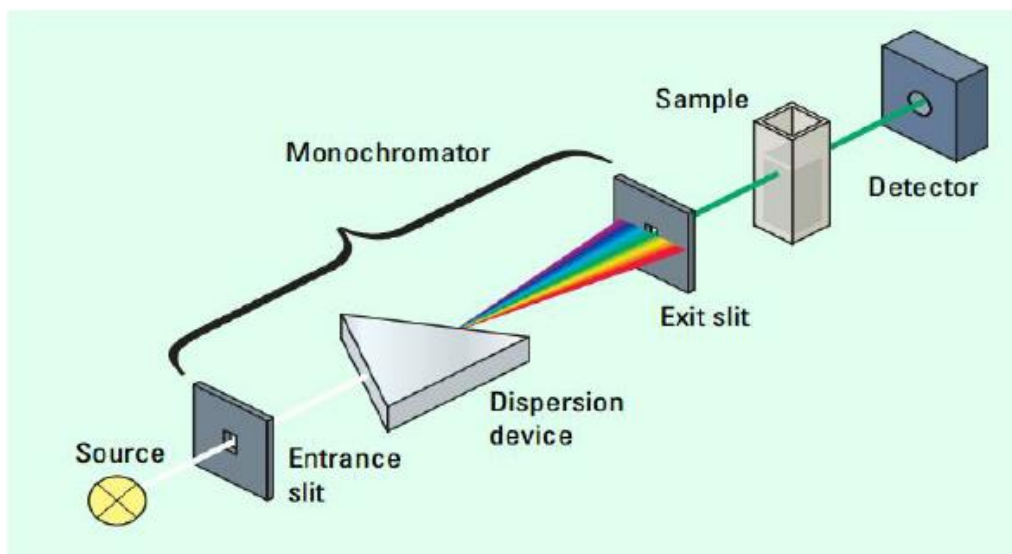


Figure 4.6 A schematic representation of a conventional spectrophotometer (partially modified from ref. 75)

Based on the spectroscopy fundamentals explained above N-phenylurea absorption bands attribution has been performed. The absorption spectrum of our target molecule is shown below. It has been obtained by means of a UV-Vis Varian Cary 5000 spectrophotometer.

Two main absorption bands can be labelled (Fig. 4.7):

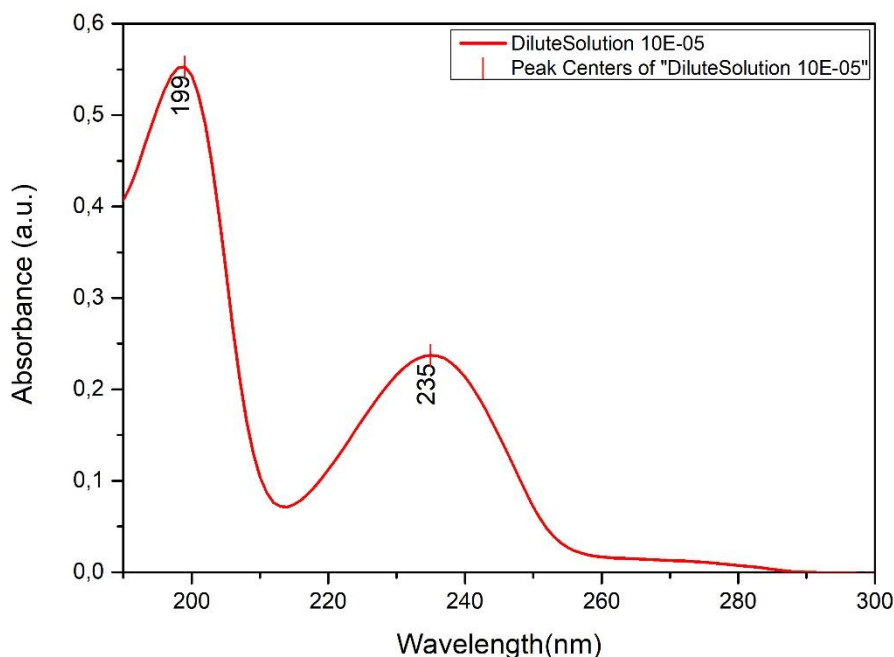


Figure 4.7 N-phenylurea ($1 \cdot 10^{-5} \text{M}$) UV-Vis spectrum

- At 199 nm the peak corresponds to the amine group of the molecule $-\text{NH}_2$. Allowed electronic transition is of the type $n \rightarrow \pi^*$ due to the presence of the nitrogen lone pair;
- At 235 nm the peak corresponds to the aromatic part of the molecule. In this case the electronic transition is of the type $\pi \rightarrow \pi^*$. Benzene ring is characterized by a molar extinction coefficient of $\sim 8000 \text{ Lcm}^{-1} \text{mol}^{-1}$;

A short list of common chromophores [76] (Tab. 4.1) and their features (λ_{max}) is given below in order to check the coherency of the attribution.

Table 4.1 Wavelengths of absorption of main functional groups acting as chromophores in organic molecules (data collected from ref. 76)

Chromophores	λ_{max} (nm)
Amine (NH_2)	195
Ester ($-\text{COOR}$)	205
Carboxyl acid ($-\text{COOH}$)	200-210
Nitro ($-\text{NO}_2$)	210
Azo ($-\text{N}=\text{N}-$)	285-400
Benzene	198 255

In order to follow qualitatively the degradation of N-phenylurea, modifications in peaks position and intensity have been attentioned. Some peak shifts can be distinguished and a sketch is shown in the figure below (Fig. 4.8) [77]

With the aid of an integrating sphere it is possible to perform diffuse reflectance (DRS) measurements (Fig. 4.9). By processing data collected into the spectrum the energy band gap (E_{bg}) of the powders can be computed by means of Kubelka-Munk function.

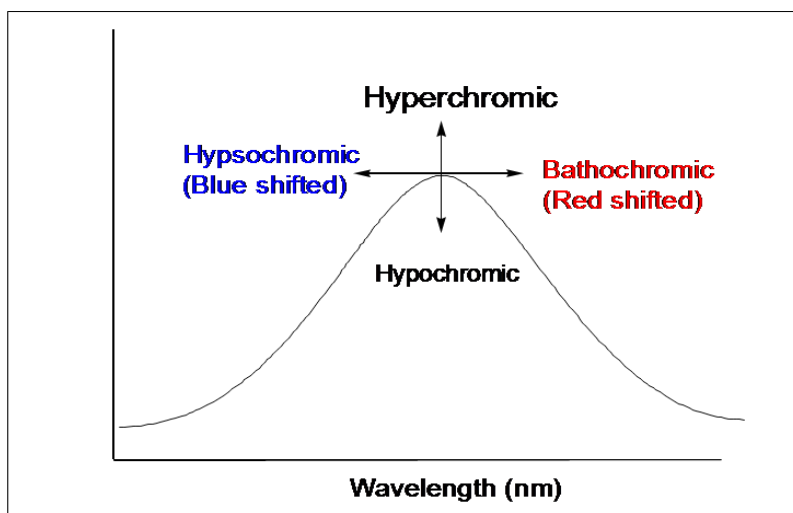


Figure 4.8 Definition of shifts in absorbance spectra (modified from ref 77)

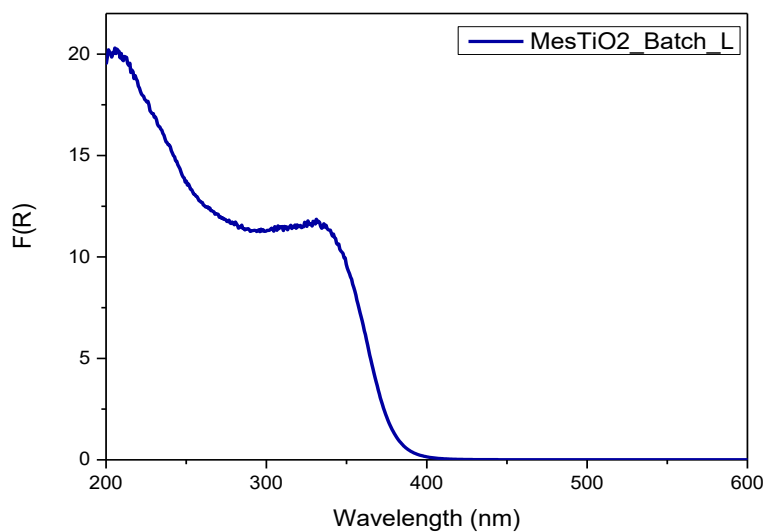


Figure 4.9 Mesoporous TiO_2 diffuse reflectance spectrum

4.5 Infrared spectroscopy

4.5.1 Theory

IR radiation interests the region of the electromagnetic spectrum between visible light and microwaves. In particular three different zones can be distinguished:

- Near IR (NIR): $13000\text{-}4000\text{ cm}^{-1}$;

- Medium IR (MIR): 4000-200 cm^{-1} ;
- Far IR (FIR): 200-10 cm^{-1} ;

Interactions between electromagnetic radiations and molecules induce the variation of the vibrational frequency of an atomic bond (vibrational transition) that reflects specific chemical groups on the surface of the solid.

IR spectroscopy is based on the empirical model by which a molecule can be described by means of a harmonic oscillator.

Molecules may vibrate into two different ways:

- Stretching: it is characterized by a periodic oscillation along the binding axis resulting in a variation of the interatomic distance.
- Bending: binding angle may be warped;

4.5.2 Instrument description

In order to obtain IR spectra in both NIR and MIR regions two types of instruments can be used:

- Dispersive spectrometer: a ceramic wire is heated up to 1600 $^{\circ}\text{C}$ to generate IR radiation that is split into reference and sample beams. A chopping mirror keeps rotating with a 11 Hz frequency and beams are sent alternatively to a diffraction grating (a prism) which disperses the light that is in turn refocused and sent to the detector. It transforms IR radiation into an electric signal. The instrument is aimed to record how the electric signal varies over time and produces a spectrum.
- Fourier-transform spectrometer: conversely to the first one, it is aimed to record spectra simultaneously over the whole spectral range. It uses an interferometer[78] (Fig 4.10) that is equipped with a moving mirror in order to introduce a difference in the optical path and produce interference with the beam reflected by a stationary mirror. Interferograms are difficult to be read so a mathematical tool (Fourier transform) is applied to convert collected data into a spectrum.[79]

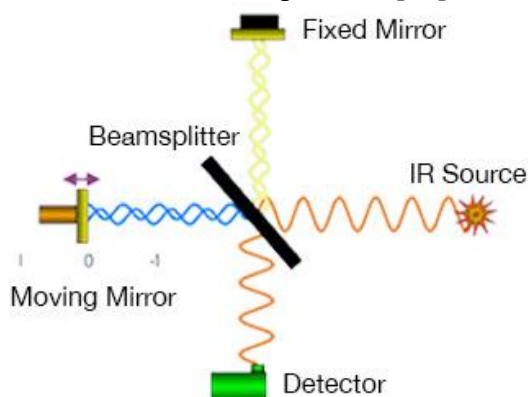


Figure 4.10 An interferometer used in FTIR spectrometer to produce interference phenomena (modified from 79)

4.6 Transmission electron microscopy (TEM)

4.6.1 Theory

Electron microscopy is used to study morphology and structure of nanomaterials.

Optical microscopy provides a low resolution (200 Å) and an alternative technique is exploited to better investigate crystal structure and the presence of reticular defects.

In detail, in transmission electron microscopy a tungsten wire is heated to emit electrons that are accelerated by an anode. Commercial anodes may accelerate electrons up to 100-300 kV.

Electrons are negatively charged and give scattering due to coulombian interactions. They have lower wavelengths than light providing consequently a higher resolution. Accelerated electrons hit the sample that has to be thin (10-200 nm) to guarantee electronic transparency and allow scattering phenomena. Anelastic scattering gives information about composition of materials whereas elastic scattering leads to diffraction and image processing[80]. The system is equipped with some lenses. When a voltage is applied between the cathode (electrons source) and the anode (perforated screen), an electromagnetic field is generated and it is parallel to the lens axis[81]. The magnetic field acts on the negative charge by deviating its motion towards the sample. Image detector is mounted under the specimen i.e. in transmission.

TEM resolution limit is 0.5 nm and this technique provides a magnification up to 100000x.

Resolution can be defined by Rayleigh criterion:

$$\text{sen}\theta = 0,61 \left(\frac{\lambda}{\rho} \right) \quad (4.7)$$

Where

θ is the resolution defined as the minimum distance between two distinguishable points on a specimen;

λ is the wavelength of the radiation measured in nm;

ρ is the slit diameter of a diffraction pattern.

4.6.2 Data acquisition

In order to perform the measurement a sample holder is used. It is made of a copper grid whose thickness is 3 mm supported by black carbon that ensures thermal and electrical conductivities. The powder is first dispersed in water and sonicated. Few drops of the resulting dispersion have been deposited on the grid. FEI Tecnai transmission electron microscope has been used with the aim of studying intra/interparticle porosity of the synthesized powders. (Fig. 4.11) The instrument is equipped with LaB₆ filament and provides a 120 kV voltage with a maximum resolution up to 0.2 nm.

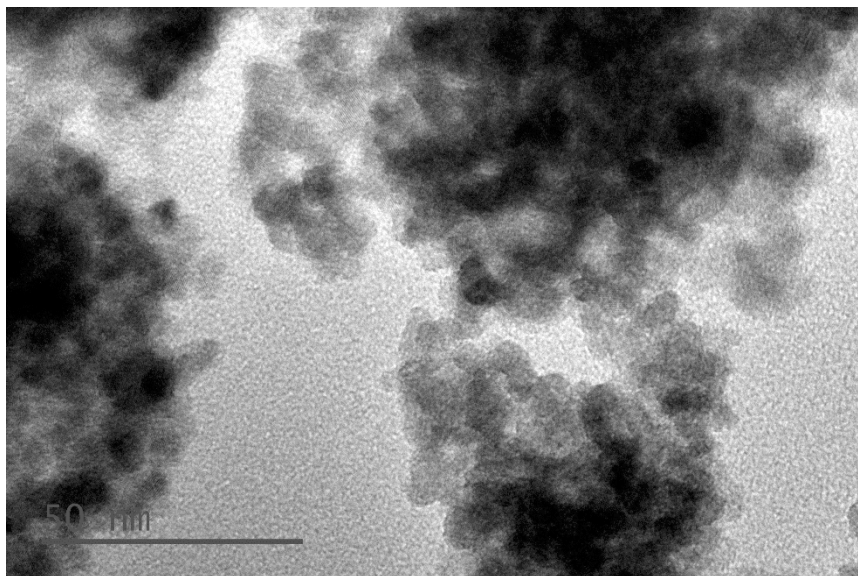


Figure 4.11 TEM image of a mixed phase TiO₂ (anatase + brookite) calcinated at 200°C

4.7 Dynamic light scattering (DLS): ζ potential measurements

4.7.1 Theory

In order to predict stability of a colloidal dispersion or to study electrostatic interactions among NPs, ζ potential measurements can be performed.

NPs dispersed in water are surface charged because ionization or specific adsorption phenomena occur. Charged particles are surrounded by a double layer (DL) whose composition is different from the bulk. DL is made of two regions: the inner one (Stern's layer) consists of ions that are strongly bounded to the surface, the outer one (diffuse layer) in which the charge distribution is governed by a balance between electrostatic and thermodynamic forces. Shear plane is theoretically placed between these two regions and ζ potential is measured at this level.

Colloidal dispersion stability is ruled by DLVO (Derjaguin Landau Verwy Overbeek) theory. It is well known that TiO₂ is a metal oxide and its potential determining ions (pdi) are H⁺ and OH⁻. That is the reason why ζ potential is function of pH.

High values of ζ potential provide stability to a colloidal dispersion due to electrostatic repulsions that hinder particle aggregation. (Fig 4.12) If $-30 < \zeta < +30$ mV a monodispersed system is obtained.[82][83]

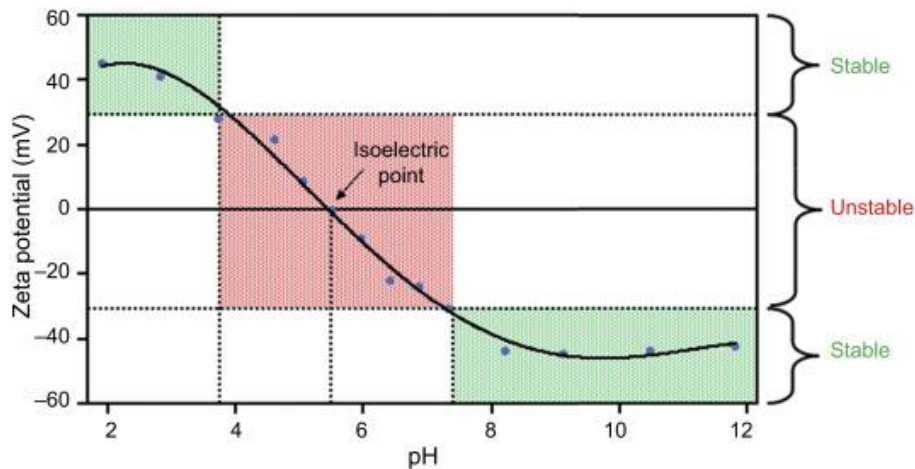


Figure 4.12 Zeta potential vs pH: a graphical description of colloidal stability in water (modified from ref 83)

Attractive and repulsive forces can be balanced by[84]:

- Adding ligands or polymers that could be adsorbed on particle surface. A shield effect of the surface charge is provided;
- Tuning the ionic composition of the system. Concentration of charged species is varied to ensure stability.

4.7.2 Data acquisition

DLS (dynamic light scattering) is used to measure both surface ζ potential and particle size distribution (PSD). ζ potential measurements have been performed by means of a Zetasizer Nano ZSP to obtain pzc (point of zero charge) values. To prepare the sample a small amount of powder has been suspended in water and sonicated for 5 minutes. pH of the solution has been adjusted by using HCl (pH = 0,9) or NH₄OH (pH = 11).

In order to measure PSD, powders have been suspended in water and sonicated for 30 minutes then a quartz cuvette with a 173° scattering angle has been used to perform the measurement. In DLS measurements the sample holder is irradiated by a laser whose wavelength is 632,8 nm. Brownian motion causes variations in light scattering intensity. Velocity of these variations is recorded over time and a correlation function is applied to compute particle diffusion coefficient that is in turn converted to a hydrodynamic diameter value (Fig 4.14) by means of Stokes-Einstein equation.

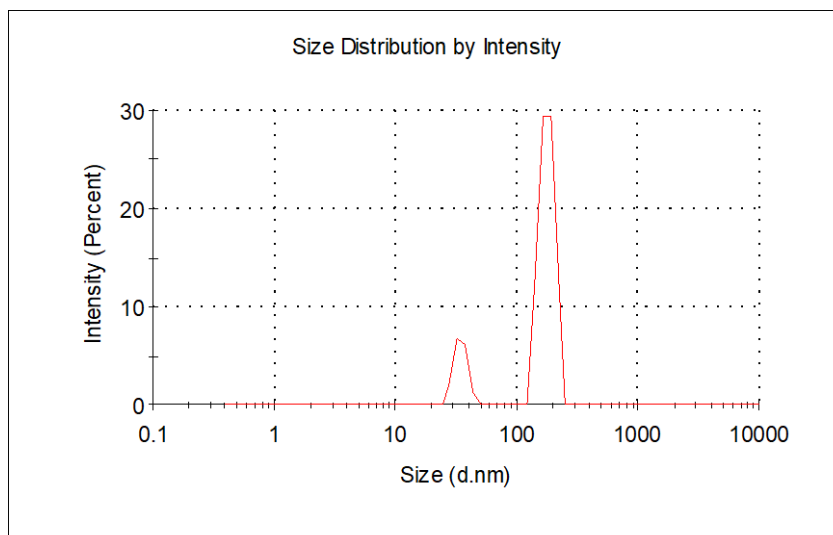


Figure 4.13 Mesoporous TiO₂ (calcined at 450°C) particle size distribution at pH = 11

5. Materials

TiO₂ nanoparticles can be obtained by using different synthesis procedures. In this chapter an insight of three methods will be given. They are slightly modified from the conventional sol gel method (Fig. 5.1):

- Template-assisted sol gel method (TASG);
- Template-assisted sol gel method in a reverse micellar environment (RM);
- Facile sol gel method in acidic conditions.

In general, by apportioning some modifications to the synthesis conditions, catalysts characterized by a higher specific surface area (SSA) and a more ordered porosity occur compared to Degussa P25 (non-porous commercial titania used as reference). P25 is a mixed phase (80% anatase 20% rutile) catalyst obtained by TiCl₄ hydrolysis in an oxy-hydrogen flame. [85]

Besides having high SSA, obtaining mesoporous materials means promoting diffusion phenomena of the reagents towards the active sites of the catalyst.

5.1 Template-assisted sol gel method

5.1.1. Method description

Ti precursors in water are highly reactive and the synthesis of stable TiO₂ NPs can be led if non-ionic surfactants (such as Pluronic hereafter referred as P123) are used [33]. P123 is a symmetrical triblock copolymer made of alternated PEO₂₀-PPO₇₀-PEO₂₀. Template usage induces a spatial limitation enhancing the formation of NPs with a high ordered mesoporosity[86]. It also reduces aggregation processes[87]. Pore size distribution of highly ordered TiO₂ mesostructure is narrower than that of P25.

Ti alkoxide used as precursor can be efficiently stabilized if a non-ionic surfactant is dispersed in an alcoholic solution with a concentration less than CMC (critical micelle concentration).

A modified sol-gel synthesis approach will be summarized below and the EISA (evaporation induced self-assembly) process will be coupled to the already known method.

EISA process is led in a water/ethanol solution followed by precursors oligomers formation which is controlled by adding an acid (such as HCl). By tuning the relative humidity of the surrounding air, it is possible to induce the evaporation of the solvent (ethanol) enhancing the self-assembly process leading to the formation of a hybrid phase (inorganic TiO₂ and organic surfactant). [33]

By using an acid catalyst during the former reaction, the diameter of the resulting crystallites has a lower value. This means that acid-catalysed hydrolysis step leads to a

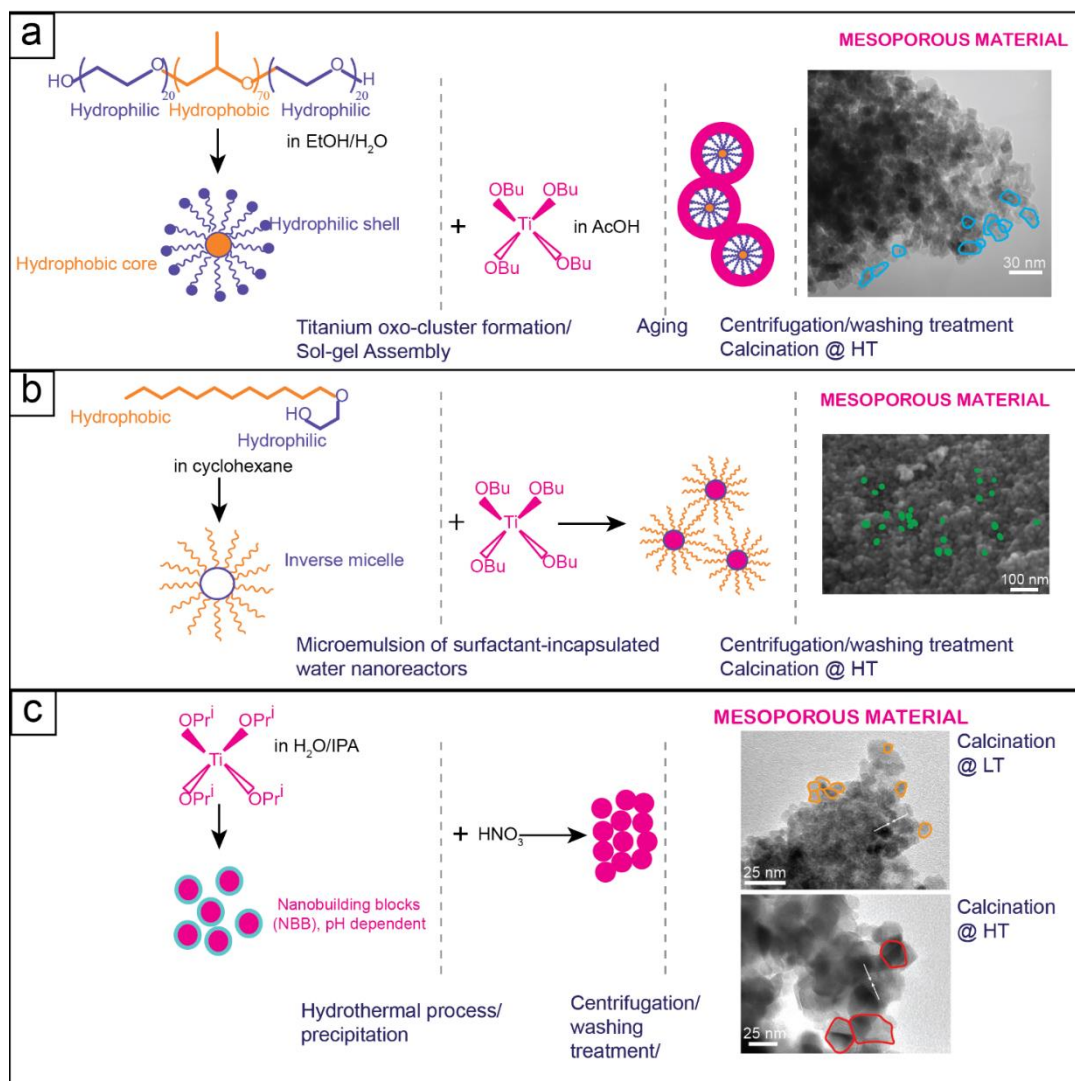


Figure 5.1 Scheme of the three synthesis methods proposed to obtain TiO₂ NPs (from Freyria et al, unpublished)

higher SSA. In the conventional sol-gel method hydrolysis is a fast step and the following polymerization is hindered.

Self-assembly process occurs by means of the formation of weak interactions (generally hydrogen bonds) between the acid catalyst and the hydrophilic chain of the surfactant. [88]

Acetic acid acts as a precursor stabilizer. In particular, acetate ions behave as chelating agent and modify (i.e. increase) the coordination number of the precursor molecule. In this way stability can be reached. [89]

5.1.2 Synthesis #1: a triblock copolymer used as template

In order to lead the first synthesis procedure [90] (TASG) two solutions have been prepared.

SOLUTION A:

- Titanium tetrabutoxide $\text{Ti}(\text{OBu})_4$ 20g
- Aqueous solution of acetic acid (AA, 20% v/v) 120 ml

24 ml of AA are mixed with 96 ml of bi-distilled water. $\text{Ti}(\text{OBu})_4$ used as precursor is added dropwise because it undergoes fast hydrolysis. The resulting mixture is left under vigorous stirring at room temperature for 4 hours.

SOLUTION B

- Pluronic P123 12 g
- Ethanol (EtOH) 80 ml

In order to prepare solution B, 12 g of P123 are dissolved in water. The resulting mixture is left under vigorous stirring for 4 hours at room temperature.

After 4 hours solution A is added dropwise to solution B paying attention not to form aggregates. The mixture (A+B) is sealed and left under stirring for 24 hours at room temperature. The following step consists of pouring the mixture in a Teflon autoclave leaving it in a stove at 98°C for 48 hours (i.e. aging step of the sol-gel method).

Once the aged mixture is withdrawn from the stove, it is washed with ethanol and bi-distilled water (with a ratio 1/3) in a typical tube that is placed in a centrifuge working at 4000 rpm for 12 minutes. Washing cycles are repeated until the supernatant did not show any aggregate. Finally, the wet powder obtained undergo the drying process into a stove at 60°C for 48 hours.

As-prepared powder is calcined at 450°C for 4 hours with a temperature ramp of $1,8^\circ\text{C}/\text{min}$. The calcined powder is hereafter labelled with MT.

5.1.3 Synthesis #2: Fe doped Mesoporous Titania

This synthesis is also used to manufacture a Fe doped TiO_2 sample. Additional steps concerning the doping procedure are listed below in more detail.

$\text{FeCl}_3 \cdot 6 \text{H}_2\text{O}$ (Iron (III) chloride hexahydrate) is added to solution A in a proper amount (ca. 0.25 g) to obtain a 2.5% wt doped sample.

Then solution A is mixed with solution B and the resulting mixture is left under vigorous stirring for 24 hours. Aging and drying step are the same as those of the MT synthesis.

A slightly different synthesis is followed to obtain a Fe doped sample known as Fe-MT_dirc. Solution A, this time, contains 0.582 g of $\text{FeCl}_3 \cdot 6 \text{H}_2\text{O}$. Besides, the washing cycles after the aging step is led in a centrifuge with the following conditions: 8000 rpm for 10 minutes.

5.1.4 Synthesis #3: Reverse Micelle TiO₂

A further synthesis procedure is proposed by Nasi et al[46]. It is again based on the TASG method. This time a di-block copolymer (i.e. Brij-O20) is used as template. It is able to form inverse micelles if in contact with an organic solvent (cyclohexane). Due to Ti precursors highly reactivity in water, fast hydrolysis occurs. Reverse micelles method can be used to control hydrolysis/condensation rates hindering the formation of Ti hydroxides that could precipitate.

Reagents used for the synthesis are: polyoxyethylene (20) oleyl ether also known as Brij-O20 (C₁₈H₃₅(OCH₂CH₂)_nOH, n~20); cyclohexane (C₆H₁₂); titanium(IV) butoxide (Ti(OBu)₄, C₁₆H₃₆O₄Ti).

The surfactant is dispersed in the oil phase by stirring vigorously at 50°C. Bi-distilled water is added to form a water in oil (w/o) microemulsion. The resulting mixture is stirred for 45 minutes. Ti precursor is added drop by drop to the emulsion then it is stirred for 2 hours at 50°C. Afterwards, the emulsion is broken by 2-propanol then it is sonicated. The mixture underwent centrifugation and drying at 100°C for 24 hours. With the aim of removing the surfactant, calcination occurred at 500°C with a 2.5°C/min temperature ramp for 2 hours.

5.2 Sol gel method in acidic condition

By finely tuning calcination temperature and/or pH of the solution, mixed phase TiO₂ NPs can be tailored. Hydrothermal route is usually followed to synthesize mixed phase titania containing brookite. Conversely, thanks to its suitability at low temperatures, a facile method based on the conventional sol gel (SG) route is proposed here by slightly modifying synthesis by Mutuma et al[91].

5.2.1 Synthesis #4: mixed phase anatase/brookite TiO₂ in acidic medium

A summary of the synthesis step is provided: titanium isopropoxide (Ti(OCH(CH₃)₂)₄, known as TTIP), isopropyl alcohol (C₃H₈O), nitric acid (HNO₃) and bi-distillate water are used. 30 ml of TTIP is mixed with 30 ml of isopropyl alcohol. The mixture is stirred for 20 minutes at 500 rpm and then heated in a stove at 80°C for 5 hours. Afterwards, it is cooled at room temperature (r.t.). pH of the solution is tuned by adding a 1M solution of HNO₃ with the aim of generating sols in acidic conditions (i.e. pH = 2,0). Obtained sol underwent gelling process under vigorous stirring for 20 hours. The resulting gel is first washed with bi-distilled water, then centrifuged for 12 minutes at 4000 rpm and dried in a Teflon autoclave at 100°C for 12 hours.

Two different samples have been calcined in a muffle furnace with a 5 °C temperature ramp up to 200°C (hereafter referred as B-TiO₂_200) and 600°C (B-TiO₂_600). Before testing, the obtained powders have been washed by means of a water/ethanol mixture (3/1). Then, they underwent centrifugation for 10 minutes at 8000 rpm and drying at 60°C for 24 hours.

5.3 Characterization results

TiO₂ synthesized NPs have been characterized by means of XRD (X-ray powder diffraction), N₂ adsorption/desorption isotherms at -196°C, diffuse reflectance UV-Vis spectroscopy, transmission electron spectroscopy and ζ potential measurements in order to investigate intimately their bulk phase composition, optical and morphological properties besides the nature of the surface.

A report of the results is provided below by comparing textural properties of our samples with commercial Degussa P25 that is an extremely fine powder whose particles have a mean diameter of 21 nm. Its specific surface area is about 50 m²/g.[92]

5.3.1. Degussa P25: used as reference

XRD patterns have been collected by means of a X'Pert Philips PW3040 diffractometer using Cu Kα radiation with 2θ in the range 20°-90°. (Fig. 5.2)

It is known that P25 has a bicrystalline structure made of anatase and rutile as pattern confirms thanks to its matching with reference (ICDD 21-2172) from Powder Data File database (PDF 2000). Particularly, main peaks of anatase at 2θ = 25.3° (101) and of rutile at 2θ = 27.4° (110) can be detected.

By means of the Scherrer equation the crystallite size is calculated by extracting from the pattern the FWHM (Full Width Half Maximum) data related to the most intense peaks of the two different phases. Anatase related peak is broader than rutile one resulting in a smaller crystallite size (anatase: 19±3 nm; rutile: 23±4 nm). Results are in agreement with TEM micrograph (Fig. 5.3) that shows irregular shaped primary particles that are partially aggregated.

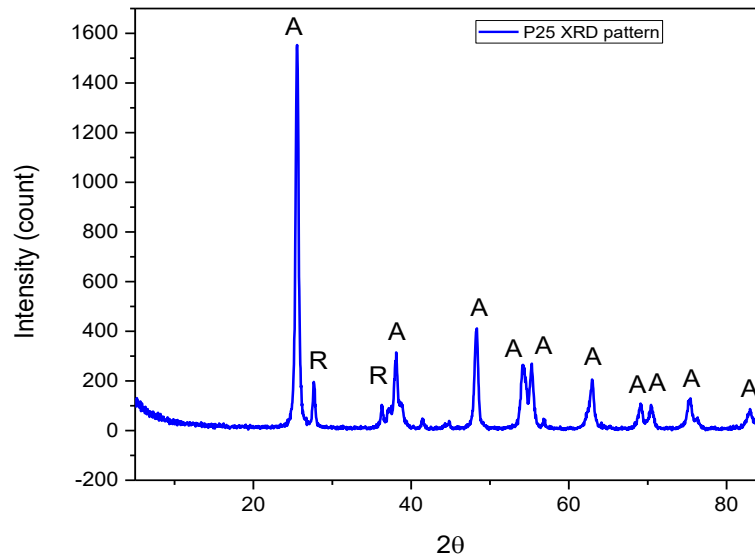


Figure 5.2. XRD diffraction pattern of P25 commercial titania (A = anatase; R=rutile)

Masolo et al confirm that P25 primary particles appear rhombic with a diameter in the range 20-40 nm.[93]

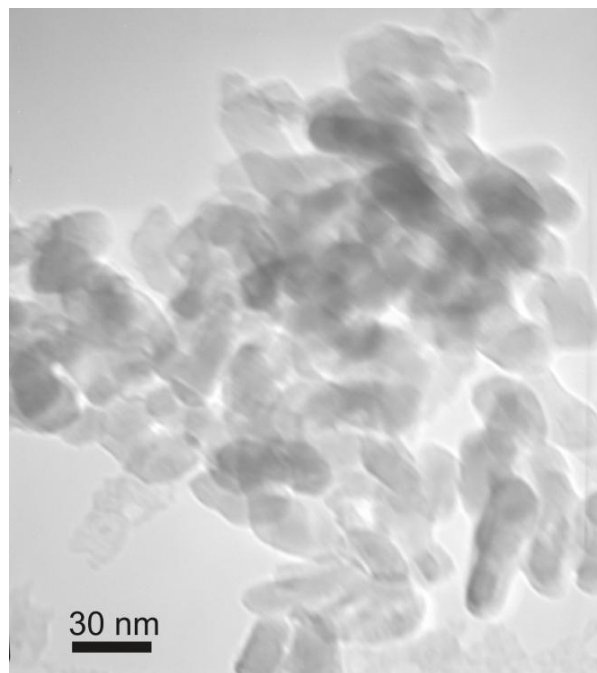


Figure 5.3 TEM micrograph of P25 commercial titania

Bulk phase composition is studied by means of Rietveld refinement to get a quantitative phase analysis (QPA): P25 consists of 88.8% anatase and 11.2% rutile.

N₂ adsorption/desorption isotherms are measured at – 196°C by means of a Micromeritics ASAP2020Plus instrument. Samples are outgassed at 150°C for 4 hours in order to remove any molecule adsorbed on the surface. Specific surface area calculations

are determined by using the BET method and pore size distribution is given by using BJH method as reported in Chapter 3.

P25 has a specific surface area of $74 \text{ m}^2/\text{g}$ as calculated by means of the linear part of N_2 adsorption isotherm. Based on IUPAC classification, it is characterized by an II type isotherm (Fig 5.4). By studying the desorption branch a matching with H3 hysteresis loop can be detected suggesting a macroporous material behaviour.

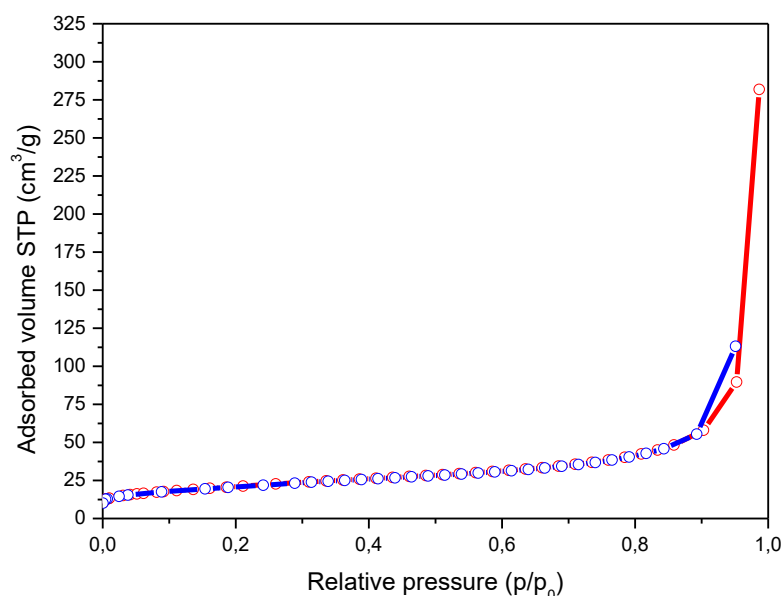


Figure 5.4 N_2 adsorption/desorption isotherm at -196°C of P25 commercial titania

5.3.2 Template-assisted mesoporous titania: MT

XRD pattern (Fig. 5.5) shows peaks only related to anatase phase (main peak at $2\theta = 25.2^\circ$) as the reference PDF #01-084-1285.

Crystallinity grade of a catalyst increases as calcination temperature does. Soft-template method requires a limit temperature of 450°C (at higher temperature the structure is not mesoporous anymore). This limit temperature ensures the presence of a unique phase (crystalline anatase). Rietveld refinement revealed the presence of 100% anatase.

By using the Williamson Hall method crystallite size has been computed. Pure anatase MT consist of $12.4 \pm 1,3 \text{ nm}$ sized NPs. This result agrees with TEM micrograph (Fig. 5.6) showing a more ordered but elongated structure compared with that of P25. Particles are homogeneous in size.

MT has a specific surface area of $150 \text{ m}^2/\text{g}$. N_2 adsorption/desorption isotherm (Fig. 5.7) shows a typical mesoporous material behaviour (type IV) as hysteresis loop is present and classified as H2 according to IUPAC classification. The shape of the hysteresis loop

suggests that pores are ink-bottle. Probably the sample is characterized by an intraparticle porosity providing a higher specific surface area with respect to that of P25. This likely leads MT to have a better photocatalytic response than that of P25. If the latter is a mixture of anatase/rutile and the occurrence of two phases retards electron/hole recombination, MT is textured to have a disposal of more active sites enhancing its activity.

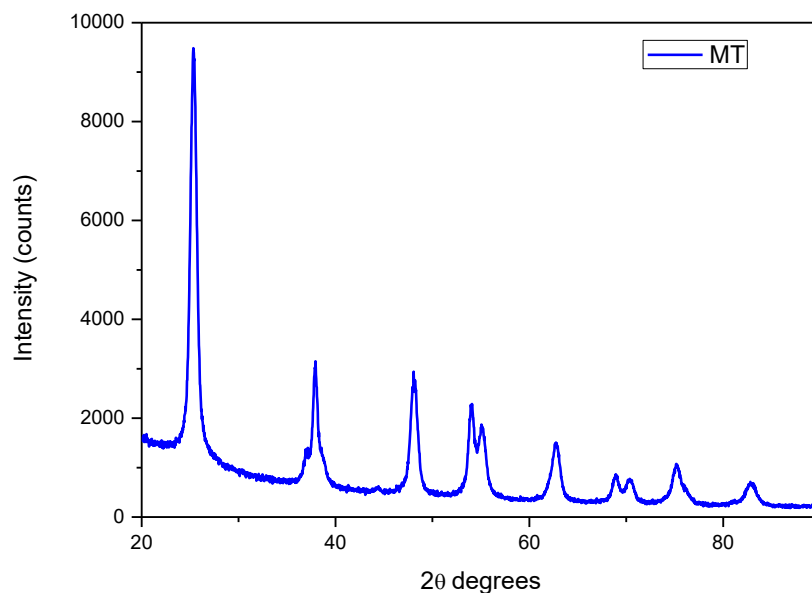


Figure 5.5 XRD pattern of pure anatase (calcined at 450°C) mesoporous titania (MT)

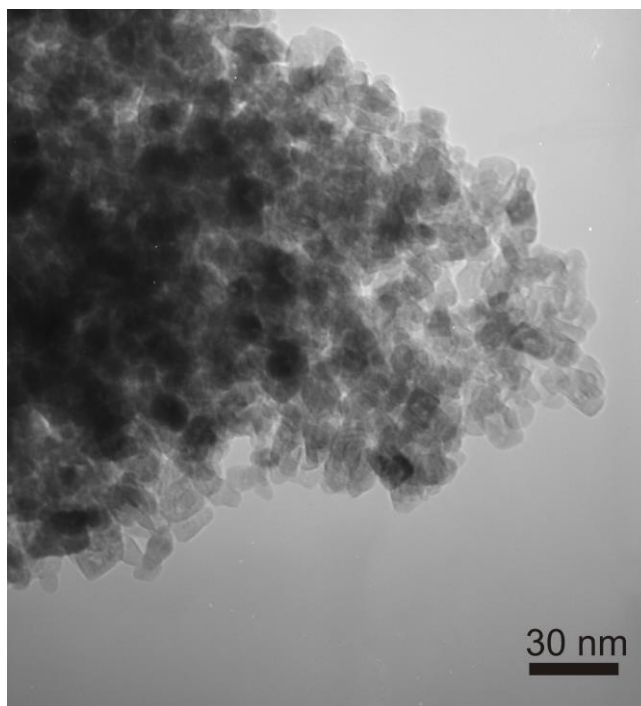


Figure 5.6 TEM micrograph of pure anatase (calcined at 450°C) mesoporous titania (MT)

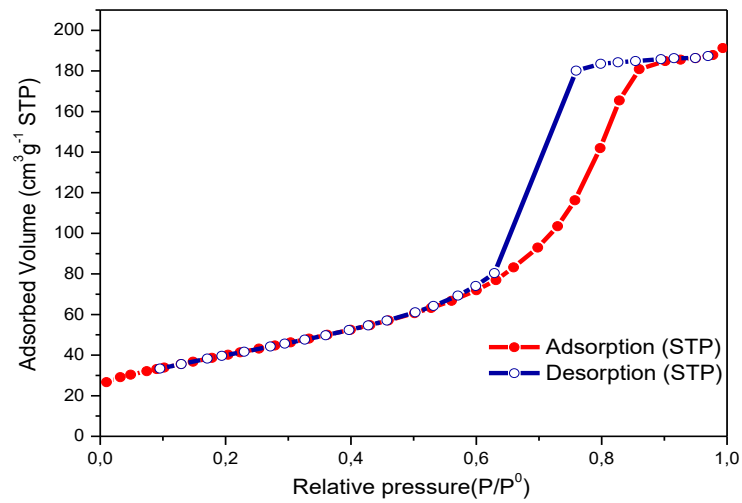


Figure 5.7 N₂ adsorption/desorption isotherm at -196°C of mesoporous titania (MT)

Pore size distribution (Fig. 5.8) shows an abundance of 7.5 nm sized mesopores.

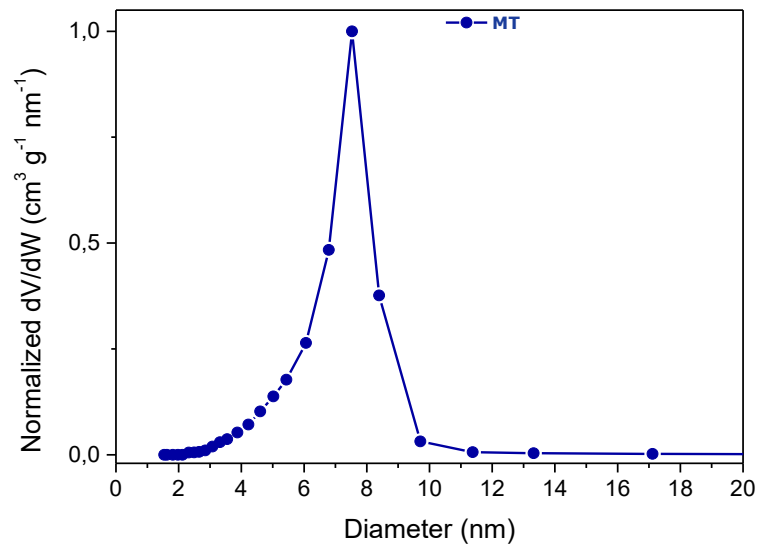


Figure 5.8 Pore size distribution of mesoporous titania (MT)

4.3.3 Template-assisted mesoporous titania: Fe-MT_dirc

XRD diffraction pattern (Fig. 5.9) shows peaks only related to anatase phase as the reference #01-084-1285 confirms.

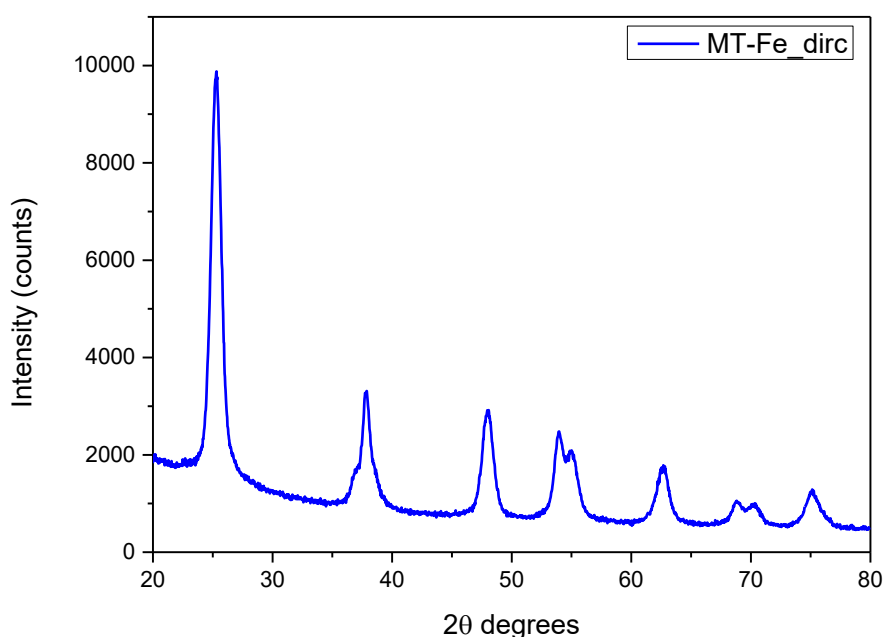


Figure 5.9 XRD pattern of pure anatase (calcined at 450°C) Fe doped titania

By studying the diffraction peaks a precise matching with the typical tetragonal structure of the anatase phase can be found. So, anatase phase is not affected by doping.

Ionic radius of Fe^{3+} is 0.785 Å whereas that of Ti^{4+} is 0.745 Å. This difference in size causes an elementary cell expansion. Even though a certain amount of dopant ion is introduced into the lattice, XRD pattern doesn't show the presence of iron oxides suggesting that a substitutional doping occurred. [94]

Few differences have been noticed by comparing MT and Fe-MT_dirc XRD patterns: they concern the distortion of TiO_6 octahedra due to Fe^{3+} substitution into the lattice, leading to a better charge separation of the photogenerated couple enhanced by the generation of an intense dipole moment. [94]

Fe^{3+} cations are shallow traps (ST) in the lattice of titania[95]. Ferric ions optimal concentration is subject of several studies because it deeply affects the lifetime of the photogenerated couple. In general, optimal Fe^{3+} concentration decreases as crystallite size increases.[96]^[17] As ferric ions behave as ST, they may be recombination centers. Recombination can occur between the hole trapped in a ST and an electron excited by the next photon during the photocatalytic process.

Pure anatase Fe-MT_dirc consist of 11.0 ± 3 nm sized NPs as resulted from Williamson Hall method.

Fe-MT_dirc has a high specific surface area of 130 m^2/g (Fig. 5.10). No appreciable differences have been detected with respect to MT concerning the presence of mesopores or the shape of the hysteresis meaning that direct synthesis method to introduce heteroatoms in the lattice of TiO_2 does not evidently affect the texture of the catalyst.

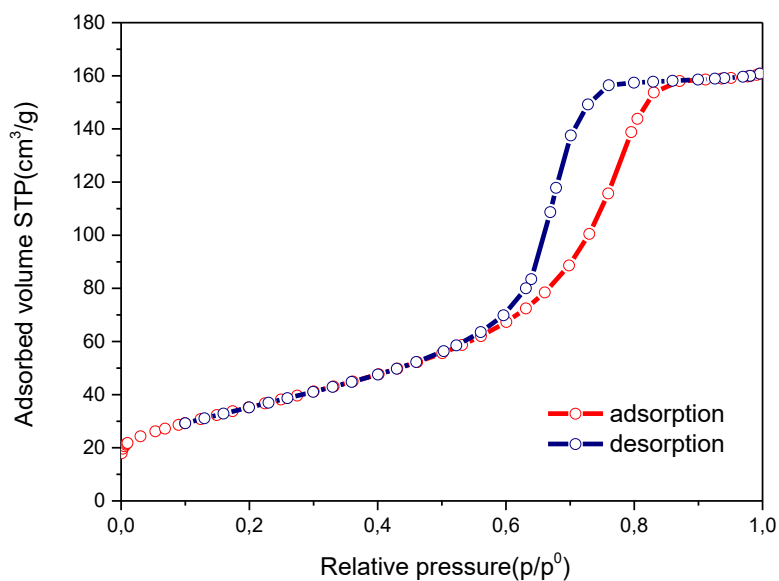


Figure 5.10 N₂ adsorption/desorption isotherm at -196°C of Fe doped titania

BJH method provides a narrow pore size distribution (Fig. 5.11) with an abundance of ca. 6 nm sized pores.

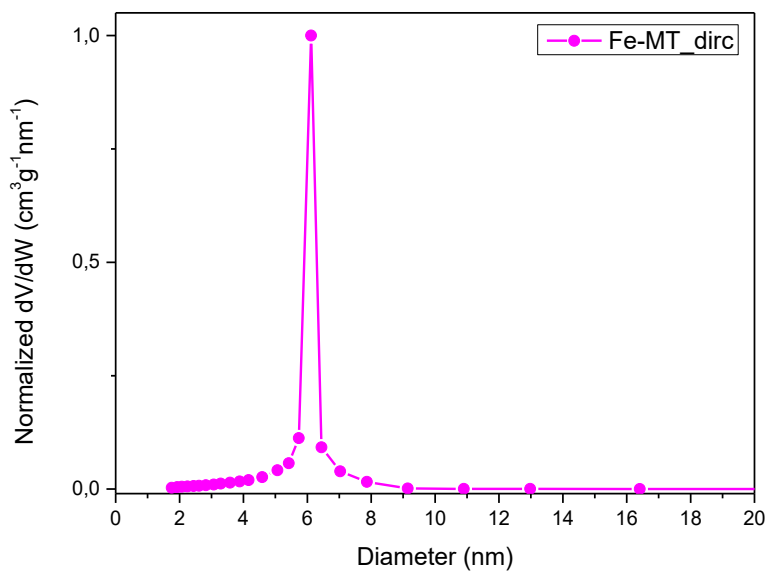


Figure 5.11 Pore size distribution of Fe doped titania

4.3.4 Template-assisted mesoporous titania: RM-TiO₂

By analysing the XRD pattern (Fig 5.12) main peaks related to both anatase ($2\theta = 25.2^\circ$) and brookite ($2\theta = 30.7^\circ$) can be detected. Rutile phase occurs in small amount. Due to synthesis

conditions, with a high content of Ti precursors, brookite formation is favoured by an acidic environment.

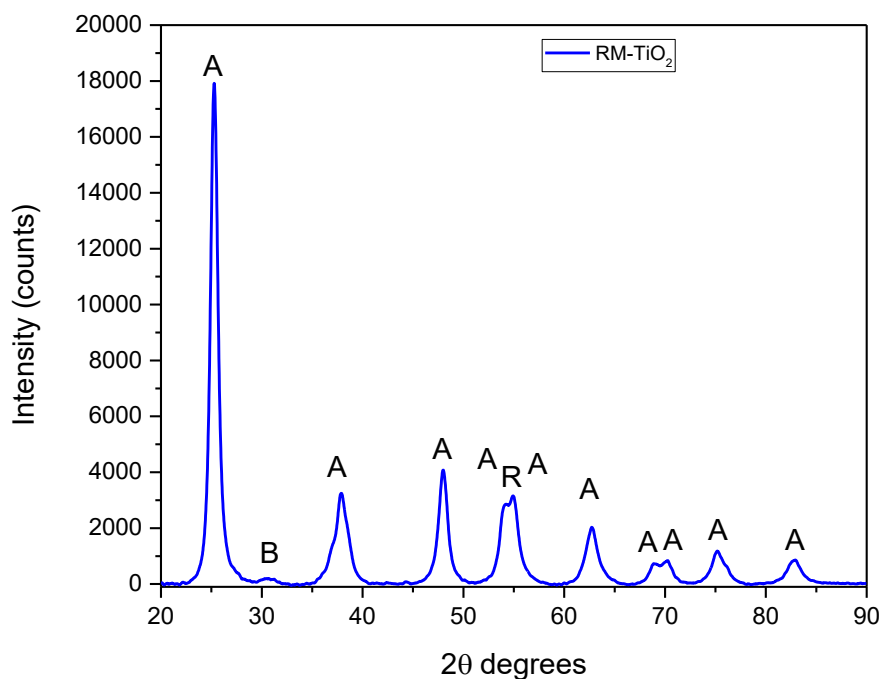


Figure 5.12 XRD pattern of RM-TiO₂. The letter “A” is used to label anatase; “B” is used to label brookite, “R” stands for rutile.

Williamson Hall method provides a crystallite size of 10.3 ± 0.5 nm related to anatase phase. whereas Rietveld refinement confirms the presence of anatase (83%), brookite (14.3%), rutile (2.1%). FESEM image (Fig. 4.13) below shows spherical nanoparticles in the range of 20 nm (in agreement with crystallite size) that are aggregated.

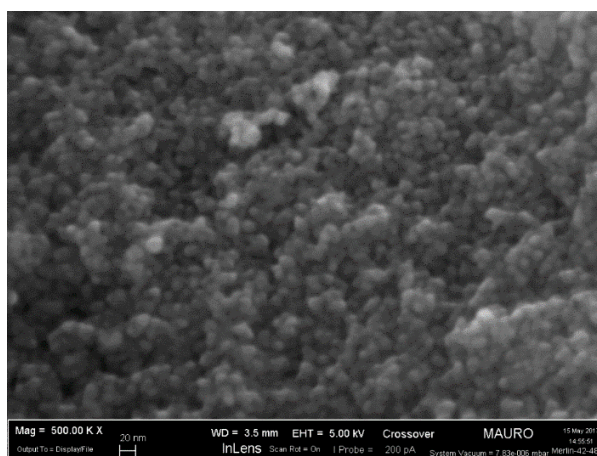


Figure 5.13 FESEM image of RM-TiO₂

The sample has a specific surface area of 71 m²/g. N₂ adsorption/desorption isotherm (Fig. 5.14) at -196°C is typical of mesoporous materials (IV type) and the hysteresis loop of H2 type is shown suggesting the presence of interparticle porosity that is distributed along the sample.

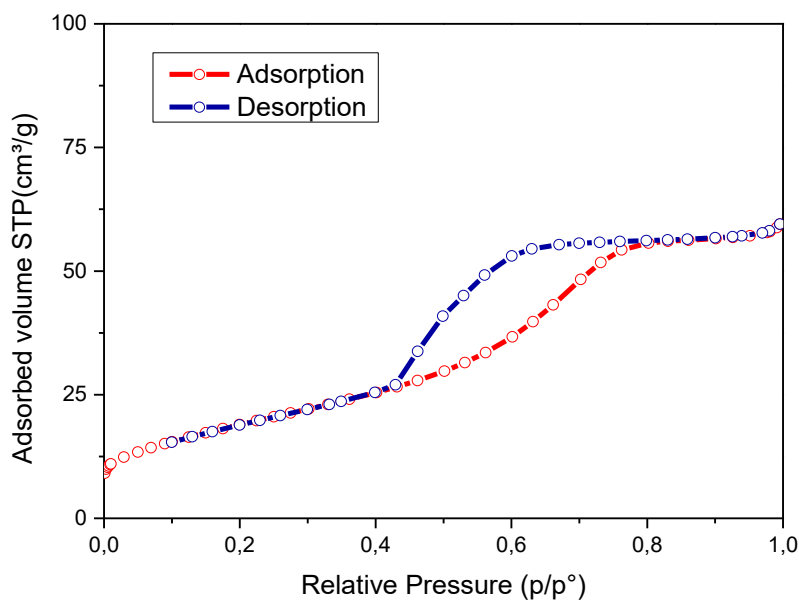


Figure 5.14 N₂ adsorption/desorption isotherm at -196°C of RM-TiO₂

BJH method provides a narrow pore size distribution with an abundance of ca. 3.5 nm sized pores. (Fig. 5.15)

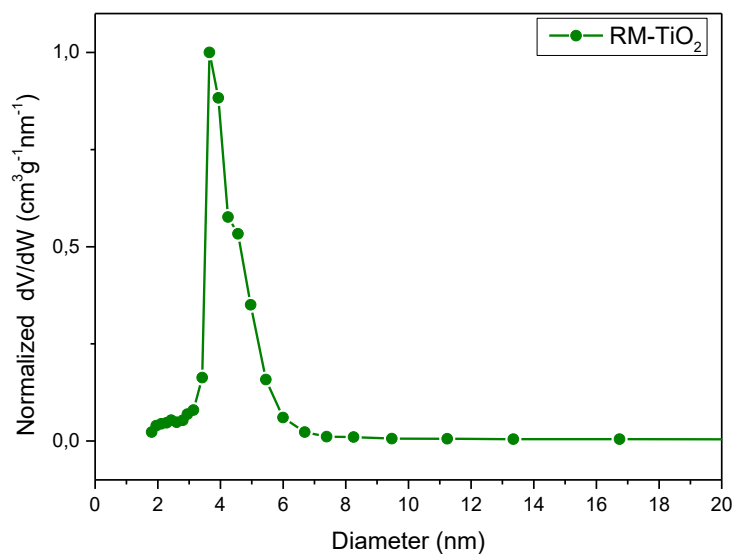


Figure 5.15 Pore size distribution of RM-TiO₂

5.3.5 Sol gel method in acidic conditions: B-TiO₂_200

XRD pattern (Fig. 5.16) shows main peaks related to both anatase and brookite. The presence of a mixed phase can be ascribed to the low calcination temperature (200°C) and the value of pH used to lead the synthesis. Reference from PDF #01-084-1285 is used to match anatase related diffraction peaks (main peak at $2\theta = 25.2^\circ$) whereas those of brookite (main peak at $2\theta = 31^\circ$) are matched by using reference PDF #96-900-4139.

Williamson-Hall method provides a crystallite size of 5.5 ± 0.6 nm related to anatase phase.

Particle size decreases as pH decreases[97][98]. It is due to the occurrence of repulsive interaction between the acidic medium and the synthesis precursor preventing the particle growth. [97]

As seen in TEM micrograph, primary particles are spherical shaped and they form irregular clusters in the range of 50 nm. (Fig 5.17)

The sample is a mixture of anatase (78%) and brookite (22%) according to Rietveld refinement.

Specific surface area of B-TiO₂_200 is 210 m²/g. N₂ adsorption/desorption isotherm (Fig. 5.18) is of Type IV showing the behaviour of a mesoporous material with a H2 hysteresis loop. The shape of the hysteresis is typical of interconnected pores. The texture of the catalyst is likely characterized by interparticle porosity.

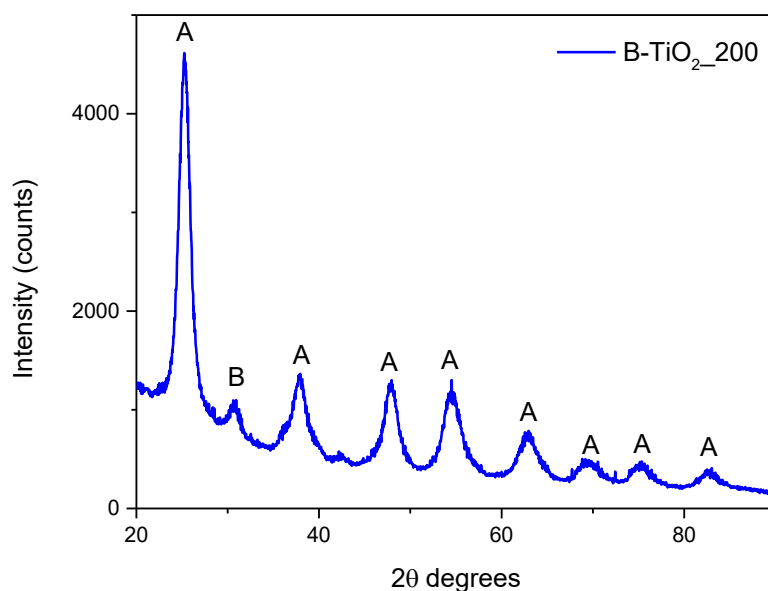


Figure 5.16 XRD pattern of B-TiO₂_200. A is used to label anatase whereas B stands for brookite

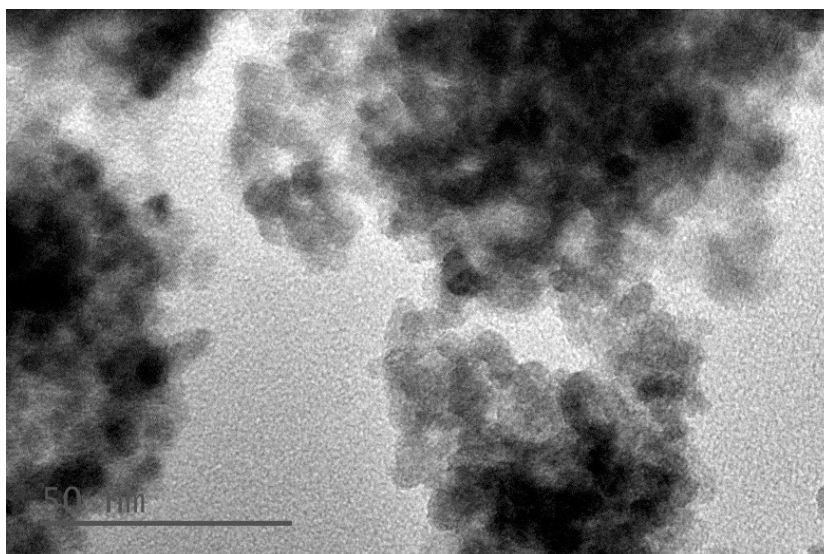


Figure 5.17 TEM image of B-TiO₂_200

Pore size distribution is narrow and provides an abundance of 5 nm sized pores but even pores with a larger size are encountered. (Fig 5.19)

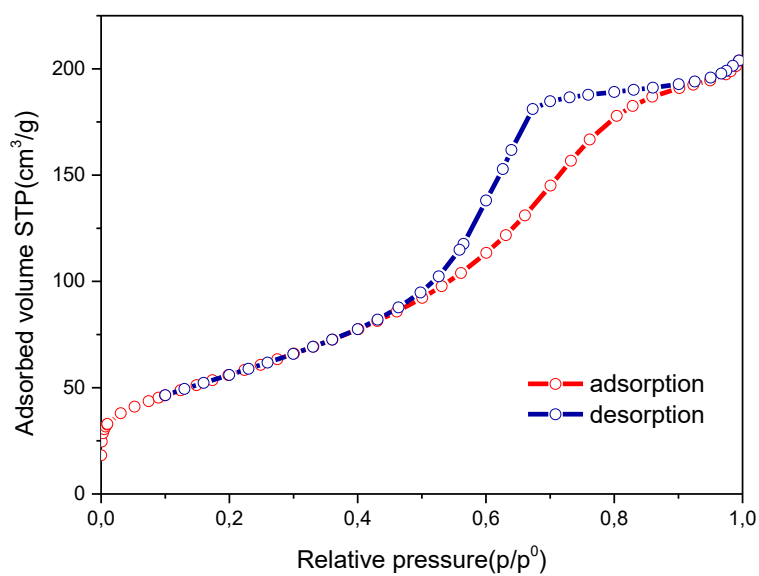


Figure 5.18 N₂ adsorption/desorption isotherm at -196°C of B-TiO₂_200

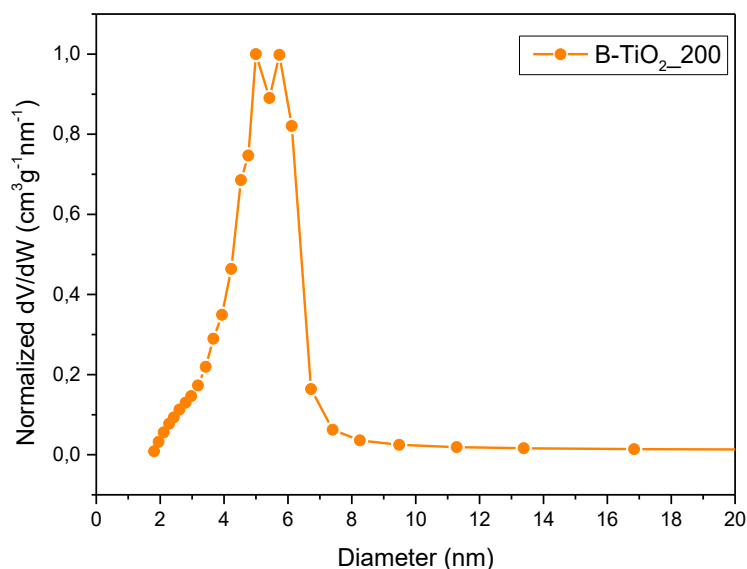


Figure 5.19 Pore size distribution of B-TiO₂_200

4.3.6 Sol gel method in acidic conditions: B-TiO₂_600

XRD pattern (Fig. 5.20) shows main diffraction peaks related to all TiO₂ polymorphs anatase, brookite, rutile. Anatase main peaks (at $2\theta = 25.27^\circ$; 48.01°) are matched by using reference PDF #01-084-1285; brookite (at $2\theta = 31^\circ$) and rutile (at $2\theta = 27^\circ$, 36° , 55°) are matched by using respectively PDF #96-900-4139 and PDF #96-900-4145.

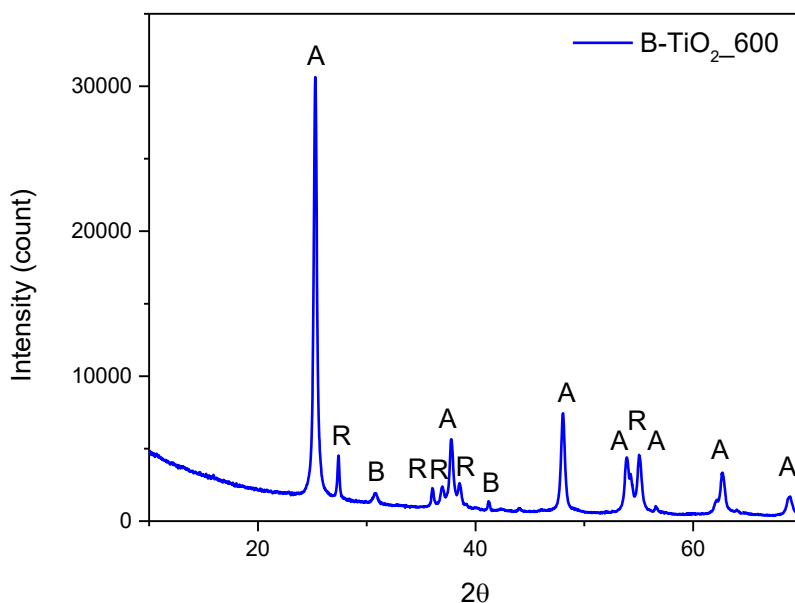


Figure 5.20 XRD pattern of B-TiO₂_600; A=anatase, B=brookite, R=rutile

Williamson-Hall plot provides a crystallite size of 39 ± 5.5 nm related to anatase phase. Crystallites are bigger than those obtained by other described synthesis due to calcination temperature leading to a high crystallinity grade (Fig 5.21).

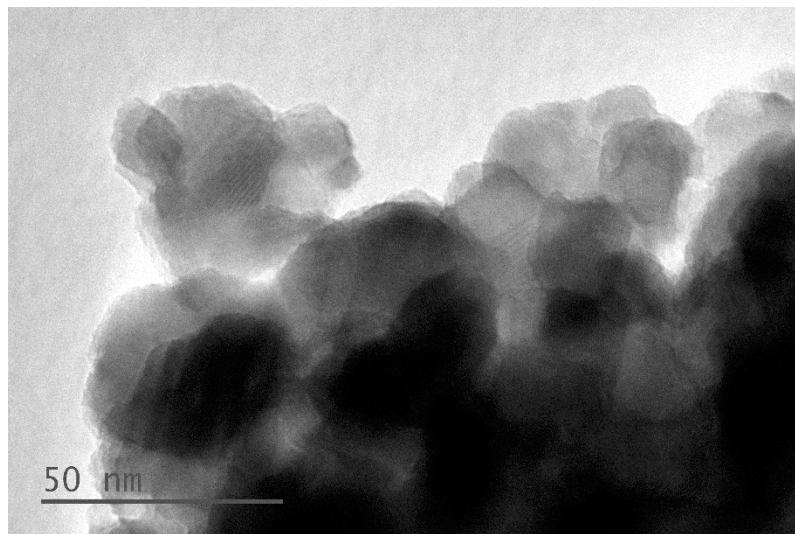


Figure 5.21 TEM image of B-TiO₂_600

B-TiO₂_600 is a mixture of anatase (82.1%), brookite (10.4%) and rutile (7.4%).

The appearance of rutile is due to the temperature chose for the thermal treatment inducing the transition towards a more stable phase of both anatase and brookite[91].

B-TiO₂_600 surface area is of 31 m²/g. The decrease of superficial area can be again ascribed to the calcination temperature. As crystals increase their size the pore volume decreases. N₂ adsorption/desorption isotherm is typical of mesoporous material (type IV) with a H2 hysteresis loop. (Fig 5.22)

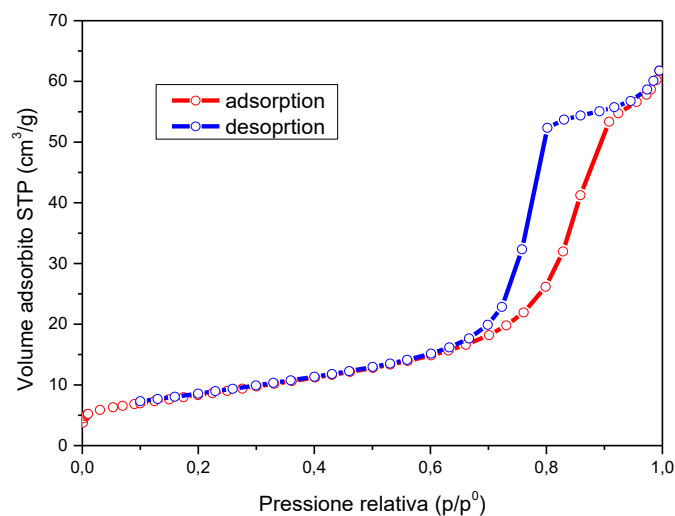


Figure 5.22 N₂ adsorption/desorption isotherm at 196°C of B-TiO₂_600

BJH method shows an abundance of 9 nm sized pores. The sample is characterized by having few mesopores larger than the maximum labelled into the plot, conversely to the other powders. (Fig. 5.23)

Characterization results are summarized in Table 5.1.

5.4 ζ potential measurements

As TiO_2 is a metal oxide, it is characterized by an amphoteric behaviour when it is dissolved in water. Photocatalytic efficiency is largely affected by pH used in the preparation of the samples, due to the fact that potential determining ions of TiO_2 in aqueous solution are H^+ and OH^- (i.e. titania nanoparticles in water can be positively or negatively charged depending on the pH). In particular, pollutant adsorption phenomena depend on the NPs surface charge. Natural pH of phenylurea is 5.7. Due to its low acidity, it preferentially adsorbed on negative charged titania nanoparticles thanks to the generation of an electrostatic attraction.[99]

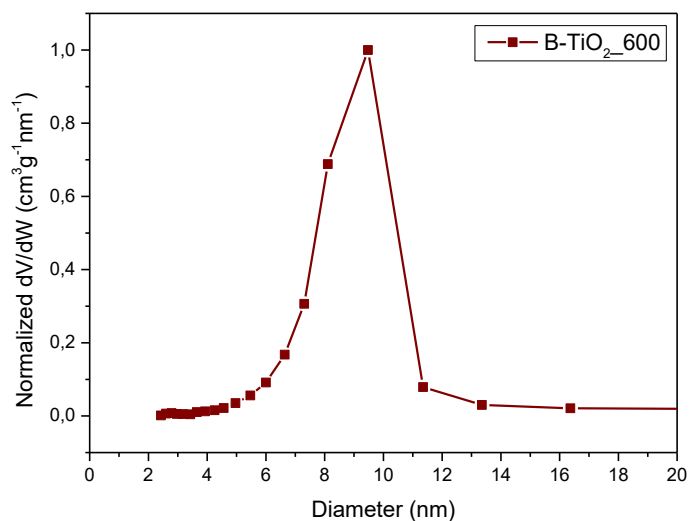


Figure 5.23 Pore size distribution of B- TiO_2 _600

Table 5.1 Results of the characterization of the synthesized samples. Crystallite size is computed by using Williamson-Hall method; Quantitative phase analysis (QPA) is provided by Rietveld refinement; SSA and pore volume are computed by means of BET theory

Sample	Crystallite size (nm)	QPA (%wt)	SSA (m ² /g)	Total pore volume (cm ³ /g)
P25	19±3 (A)	88.8 (A)	74	0.10
	23±4 (R)	11.2 (R)		
MT	12.4±1.3 (A)	100 (A)	147	0.28
RM-TiO₂	10.5±0.4 (A)	83 (A)	70	0.09
	5.4±0.1 (B)	14.9 (B)		
	7.8±0.2 (R)	2.1 (R)		
B-TiO₂_200	5.5±0.6 (A)	78 (A)	210	0.31
	3.8±0.4 (B)	22 (B)		
B-TiO₂_600	39±5.5 (A)	81.6 (A)	31	0.09
	16.8±3.6 (B)	9.3 (B)		
	52.1±8.1 (R)	9.1 (R)		
Fe-MT_dirc	12 (A)	100 (A)	130	0.25

The electrophoretic mobility of TiO₂ nanoparticles was studied and values of pzc (point of zero charge) of the synthesized samples were computed (Fig 5.24). If no specific adsorption occurs on the surface of the particle pzc has the same meaning of iep (isoelectric point)

P25 commercial titania has a pH_{IEP}=6.2-6.9. With respect to this powder used as reference, all the analysed samples have lower pH_{IEP} values. (Table 5.2)

Isoelectric point values may depend on synthesis conditions and particle size. No affection has been detected concerning titania crystalline structure.[100]

If a surfactant is used to lead the synthesis (the case of template-assisted method) NPs has a lower pH_{IEP} value than that of commercial titania. It is likely due to the presence of carbonates on the surface of the particles.[82]

pH_{IEP} increases as particle size decreases because smaller particles have a higher surface charge density.[101] It is the reason why RM-TiO₂ has the highest value of pH_{IEP} among powders we focused on in this work. Template-assisted method allows to obtain particles with ordered mesoporosity and to control their size.

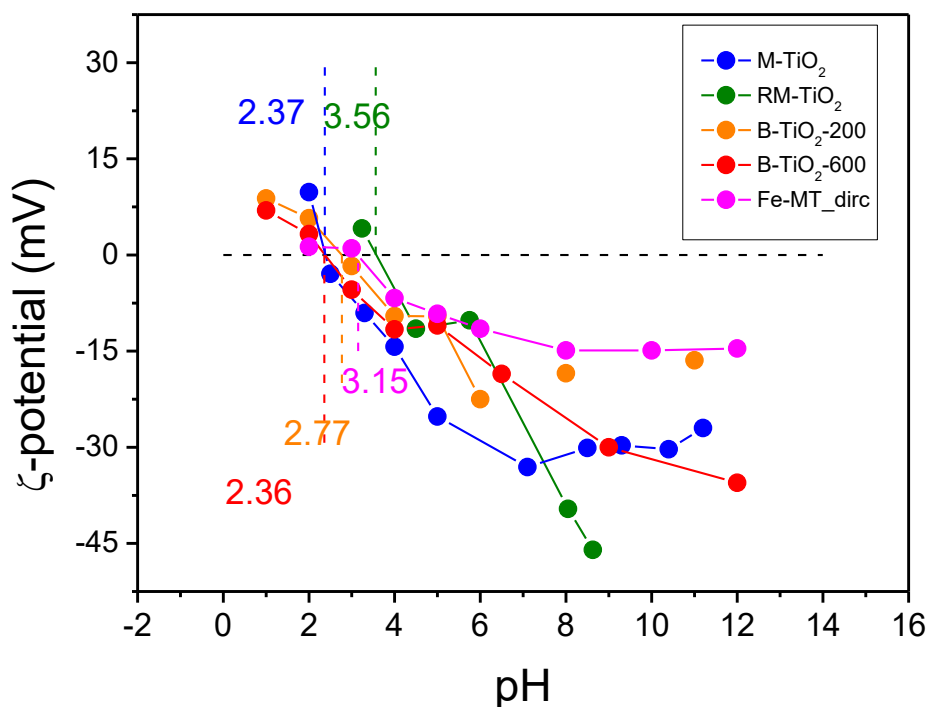


Figure 5.24 ζ potential measurements of the synthesized samples. Coloured values on the plot refer to pH_{IEP}

Table 5.2 A summary of pH_{IEP} of the samples compared to that of P25

Sample	pH_{IEP}
P25	6.2-6.9
MT	2.37
RM-TiO ₂	3.56
B-TiO ₂ _200	2.77
B-TiO ₂ _600	2.36
Fe-MT_dirc	3.15

In order to investigate the stability of the nanoparticles dispersed in water, the hydrodynamic diameter and the polydispersity index (PDI) have been computed by means of dynamic light scattering. The size of the aggregates/agglomerates deeply affects the quantum yield of the photocatalytic process due to a weak penetration of the light beam throughout the turbid solution.[102]

At natural pH~5 all the samples were highly aggregated showing high PDI values and hydrodynamic diameter with an order of magnitude $\sim 1 \mu\text{m}$ (Fig. 5.25) except for powders containing brookite (Fig.5.26)

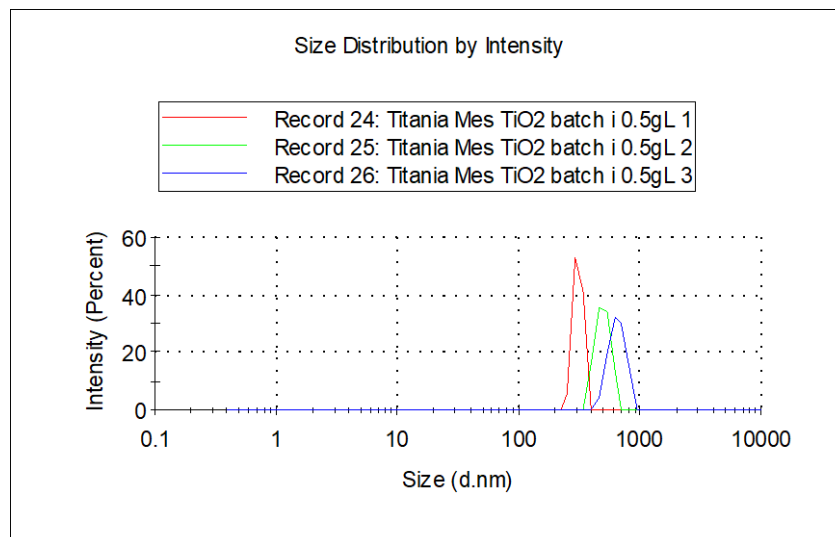


Figure 5.25 Size distribution by intensity of mesoporous titania MT at natural pH ~ 5

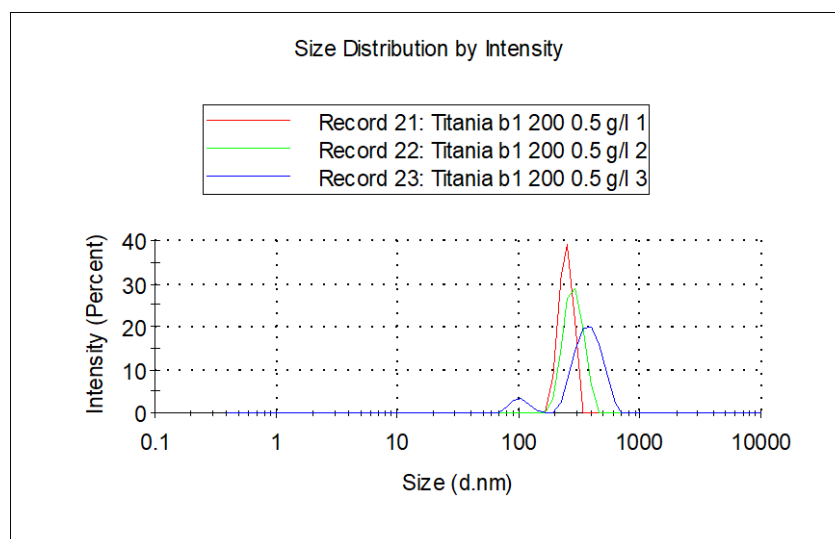


Figure 5.26 Size distribution by intensity of B-TiO₂_200 at natural pH ~ 5

5.5 Titania electronic properties: direct or indirect band gap

Electronic properties of TiO₂ nanoparticle were studied by means of diffuse reflectance (DR) spectra taken in the range 200-800 nm. The instrument used is a UV-Vis Varian Cary 5000 spectrophotometer integrated with a sphere.

Measurements of diffuse reflectance were performed with the aim of calculating the energy band gap (E_{bg}) of the synthesized powders.

When a semiconductor is hit by a photon with a proper energy (i.e. $h\nu \geq E_{bg}$) an electronic transition occurs from the valence (VB) to the conduction band (CB). If the electronic transition is permitted and the momentum of the electron is conserved, a direct band gap is computed. Conversely, if the momentum is not conserved an indirect band gap is computed.[103]

Data collected from DR spectra (Fig. 5.27) are processed by using an analytical function known as Kubelka-Munk function to produce the Tauc plot.

$$F(R) = \frac{1 - R^2}{2R} = \frac{k}{s}$$

Even if in the anatase the direct electronic transition is hindered leading to consider the band gap of the anatase to be indirect[104], both direct and indirect band gap values were computed. On the other hand, rutile and brookite exhibit direct band gap. Indirect band gap is typically smaller than direct band gap[105].

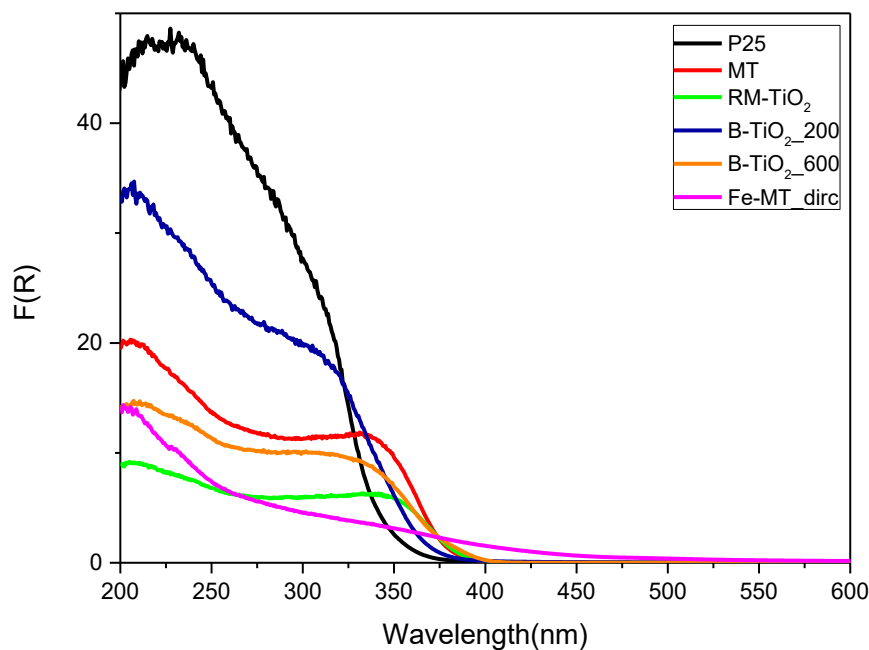


Figure 5.27 DR-UV spectra of the synthesized samples

Catalysts containing pure phases have higher E_{bg} (anatase=3.2 eV; rutile=3.0 eV, brookite= 3.1-3.4 eV [106]) than mixed phase titania (Tab. 5.3) (anatase/rutile =2.82 eV). This results in an enhanced photocatalytic activity due to a longer lifetime of the photogenerated couple[107].

Concerning the doped titania, E_{bg} decreases as the dopant percentage amount present into the lattice increases. Doping process is proposed with the aim of lowering the catalyst energy band gap (Fig. 5.28) and it allows absorption phenomena towards the visible light

region. It is possible because Fe^{3+} electrons of 3d orbitals are excited to TiO_2 conduction band.[108]

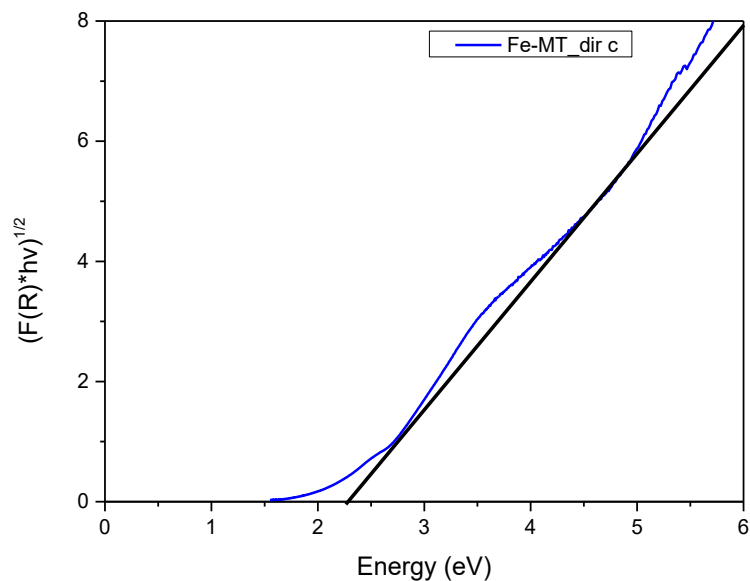


Figure 5.28 Tauc plot for Fe-MT_dir c sample. The Kubelka-Munk function (y axis) raised to $\frac{1}{2}$ refers to indirect band gap. If the power is 2, calculations are for direct band gap

Table 5.3 A summary of calculated energy band gap: two values are obtained for the samples (indirect and direct) except for the sample doped with iron (indirect)

Sample	Energy band gap (eV)
P25	3.28
MT	3.51
	3.23
RM-TiO ₂	3.35
	3.15
B-TiO ₂ _200	3.29
	3.38
B-TiO ₂ _600	3.57
	3.22
Fe-MT_dir c	3.36
	2.3

6. Photocatalytic degradation tests

The catalysts synthesised by following the routes described in the previous chapter were tested in the photocatalytic degradation of N-phenylurea with the aim of studying their activity.

In Chapter 1 several parameters that affect the efficiency of a photocatalytic reaction were discussed: choice of light source and its intensity; catalyst amount; concentration of the contaminant in water; use of extra-oxidant agent to improve OH• generation leading to the degradation of organic pollutants. Such aspects will be discussed in the following paragraphs.

Photocatalytic tests were carried out at room temperature in non-deaerated water inside a cylindrical quartz tube used as reactor. The effect of the light source on the degradation of the molecule was studied by using either solar or UV lamps.

The concentration of the analysed pollutant is regulated by law: A limit concentration ($\sim 10^{-7}$ M) of such contaminant is tolerated in drinking water. With the aim of following the degradation path of N-phenylurea by means of UV-Vis spectrophotometry, however, a higher concentration (10^{-5} M) was chosen. In this way, the main absorption peaks of N-phenylurea chromophores (at 199 nm the amine group; at 235 nm the aromatic ring) were clearly detected in the UV-Vis spectrum and Lambert-Beer law was still valid in the studied concentration range.

In order to ensure a light intensity of 1 SUN (1000 W/m^2), a light simulating solar radiation is placed at a distance of ca. 6 cm orthogonally to the tube. Solar lamp also contained a small fraction of UV radiation (22 W/m^2). In the case of UV lamp, a light intensity of 55-60 mW/cm^2 was measured. In order to compare all the results obtained from photocatalytic tests the same catalyst concentration (1 g/L) was chosen.

When the Fe-MT_dirc sample was tested, a certain amount of H_2O_2 was added to the solution in a stoichiometric quantity. A Fenton-like reaction occurred and its effects on the pollutant decomposition in water were studied.

N-phenylurea degradation path was hypothesized by following the relative modification (shift) in the main absorption peaks as described above.

6.1 Experimental setup

The purpose of the study is the exploitation of the solar light as it is a natural source to be applied in the degradation of persistent contaminants. This is the reason why a lamp that simulates solar light was used during the tests. They were led as follows:

The aqueous solution (50 ml) containing N-phenylurea in a concentration of 10^{-5} M was poured into the quartz tube in which a catalyst load of 1 g/L was after suspended. In order to obtain a good dispersion of the powder, the mixture underwent continuous stirring at 300 rpm. A typical photocatalytic test lasted 5 hours. The mixture was left 60 minutes in dark conditions meanwhile adsorption phenomena occurred. Afterwards, light was switched on for 240 minutes. Samples (~ 2 ml at time) were withdrawn every hour, they underwent centrifugation for 10 minutes at 12000 rpm with the aim of analysing the UV-Vis spectrum of the supernatant

resulted from the separation of the phases by means of a Cary 5000 UV-Vis NIR spectrophotometer using a quartz cell with a path length of 10 mm.

P25 in water was finely dispersed and very volatile hindering the separation of the liquid from the solid phase after the conventional centrifugation. A further filtration step is needed by means of a Regenerated Cellulose syringe filter (porosity 0,45 μm) prior to measurement of supernatant absorbance.

In order to remove the signal of the powder from B-TiO₂_200 and B-TiO₂_600 spectra, the same filter is used prior to measurement.

6.2 Photolysis

In order to examine the role of the photocatalyst in the degradation of the organic pollutants, a previous test, in which only the dilute N-phenylurea solution was irradiated by simulated solar light, was led with the purpose of discovering likely interactions between light and the target molecule (Fig 6.1)

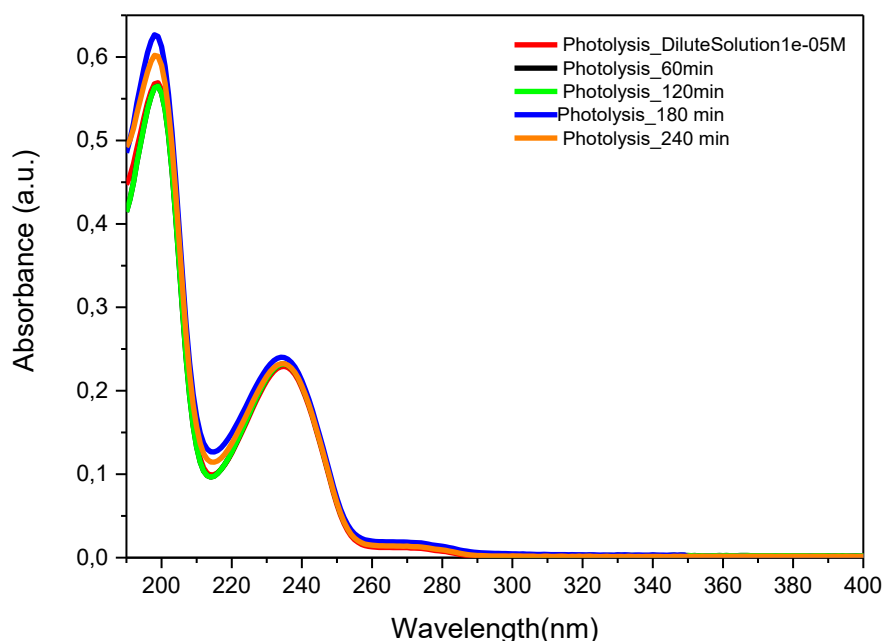


Figure 6.1 N-phenylurea 10^{-5}M dilute solution undergo photolysis under simulated solar light

By analysing the resulting spectrum, it can be stated that phenylurea is photochemically stable, in that when irradiated by a plasma lamp with an intensity of 1 SUN, it poorly adsorbs light and, thus, direct photolysis does not occur. Consequently, heterogeneous photocatalysis has to be applied to achieve the degradation of the contaminant.

6.3 Photocatalytic tests under simulated solar light

6.3.1 Template assisted mesoporous titania: MT

The spectrum of the N-phenylurea 1×10^{-5} M dilute solution (red curve) showed two main absorption peaks at 199 and 235 nm; the curve related to adsorption in dark conditions (black curve) overlapped the red one suggesting adsorption does not occur at the surface. pH_{IEP} of mesoporous titania is 2.36 whereas natural pH of the solution measured during the test is ca 5.5. So, titania NPs are negatively charged in the aqueous solution. Based on $\text{pK}_a = 13.37$ reported in literature, phenylurea is a weak acid and it is not very keen to interact with negatively charged particles. Curves shape does not effectively change in time even after two hours of illumination. (Fig 6.2) Under illumination, instead, a progressive decrease in absorption intensity occurs. After 3 hours of illumination, a blue shift of the peak at 235 nm occurs, suggesting that the aromatic ring is attacked by OH^\bullet radicals, likely leading to the loss of the lateral chain. The aromatic ring is probably opened after 4 hours of illumination and carboxylated products are formed since a new band at 200-210 nm occurs together with a weak shoulder at 228 nm likely due to the presence of $-\text{COOH}$ chromophore as reported in literature.[109]

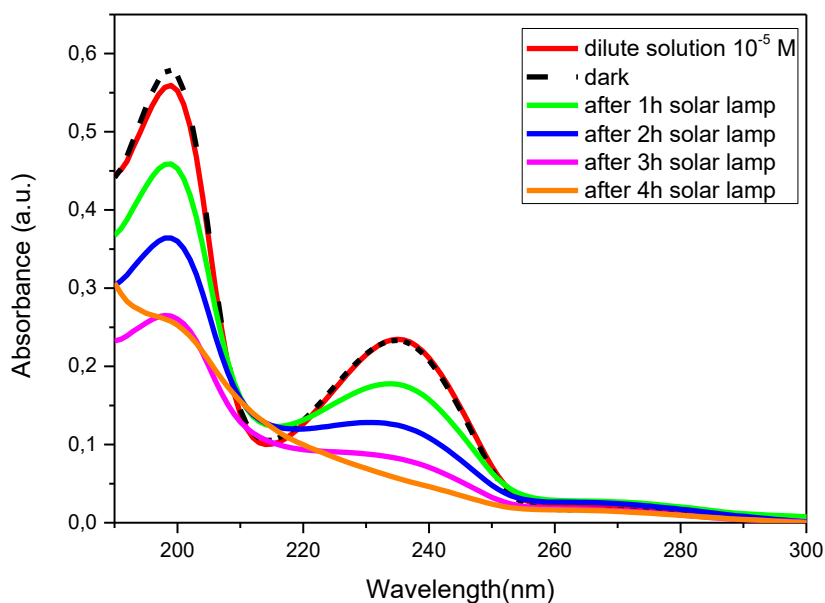


Figure 6.2 UV-Vis spectra of N-phenylurea supernatants withdrawn every hour to test the photocatalytic activity of MT sample towards the degradation of the contaminant under simulated solar light.

6.3.2 Template assisted mesoporous titania: Fe-MT_dirc

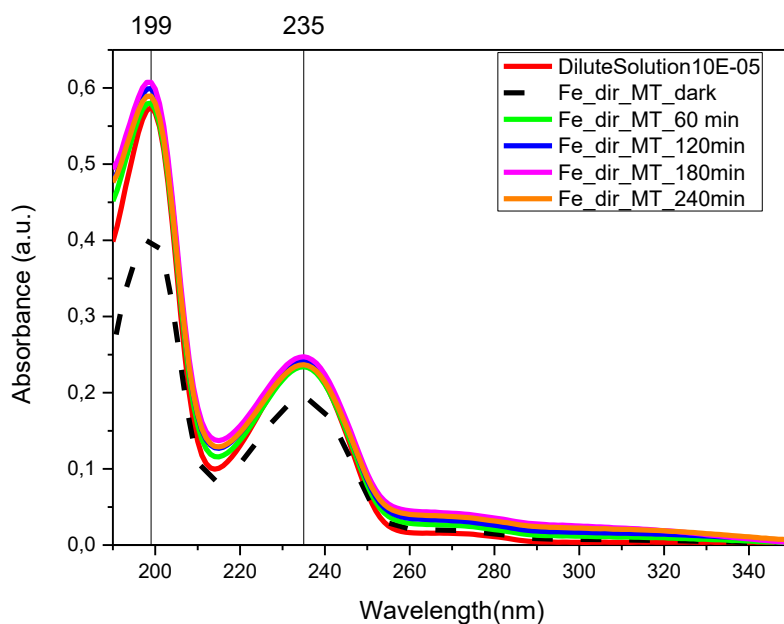


Figure 6.3 UV-Vis spectra of N-phenylurea supernatants withdrawn every hour to test the photocatalytic activity of Fe-MT_dirc sample towards the degradation of the contaminant under simulated solar light.

The decrease in absorbance during adsorption in dark conditions (dotted curve) indicates adsorption on the solid catalyst. No modification in the shape of the curves or absorbance peaks is registered during the whole test (Fig. 6.3). The two bands at 199 and 235 nm are affected by a hyperchromic effect (typically encountered if OH groups bind to the molecule) suggesting the formation of hydroxylated aromatic compounds, without breaking the aromatic ring. It is interesting to notice the appearance of a band at 280-320 nm, increasing in intensity during time, which could be ascribed to the formation of nitrates ($\lambda_{\max} = 302 \text{ nm}$, $\epsilon = 7.2 \text{ M}^{-1} \text{ cm}^{-1}$) [110].

6.3.3 Template assisted mesoporous titania: Fe-MT_dirc + H₂O₂

H₂O₂ act as OH[•] scavenger. Fe doped titania seems to be active in dark conditions as the absorbance peaks at 199 and 235 nm decrease, and this is likely due to a Fenton-like reaction. No relevant shifts are recorded but the same degradation path of the previous test could occur (Fig. 6.4): hyperchromic effect results in the formation of hydroxylated derivatives and the increasing absorption band at 280-320 nm suggests the appearance of nitrates in water.

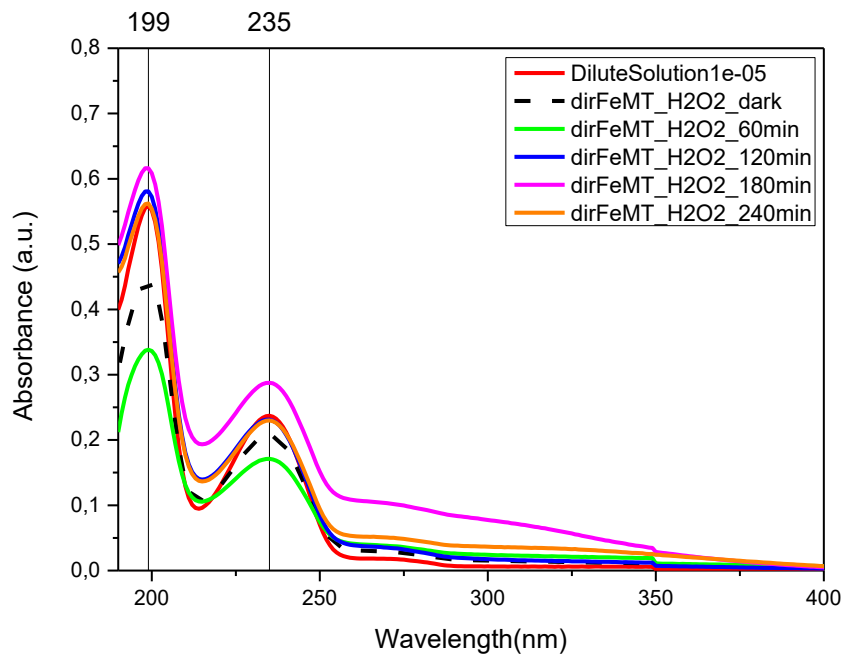


Figure 6.4 UV-Vis spectra of N-phenylurea supernatants withdrawn every hour to test the photocatalytic activity of Fe-MT_dirc sample towards the degradation of the contaminant under the combined action of simulated solar light and an extra-oxidant agent.

6.3.4. RM-TiO₂

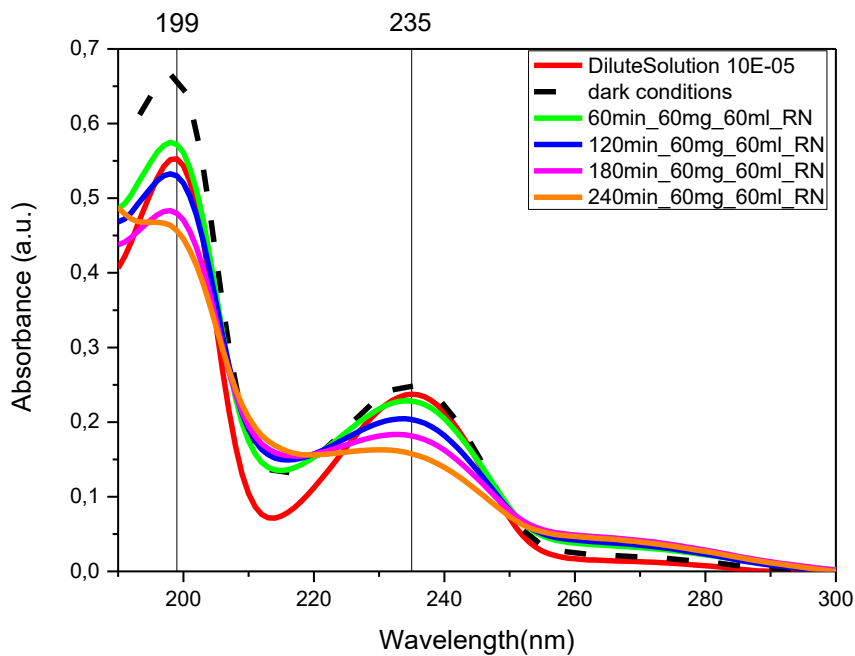


Figure 6.5 UV-Vis spectra of N-phenylurea supernatants withdrawn every hour to test the photocatalytic activity of RM-TiO₂ sample towards the degradation of the contaminant under simulated solar light.

The absorption band at 235 nm has a blue shift only after 240 minutes (Fig. 6.5). Hence, the aromatic ring is stable under the combined action of light and heterogeneous catalysis. A further band appears at 280-300 nm and it has a characteristic increase in the absorbance that is inversely proportional to the trend of the aromatic part of the molecule. This suggest that OH[•] causes the cleavage of the urea moiety with the formation of nitrates whereas hydroxylated aromatic derivates are still present even if less evidently than in the case of Fe-doped TiO₂.

6.3.5 B-TiO₂_200

Blank experiments were performed in order to take the spectrum of each powder dissolved in water by means of the UV-Vis spectrophotometer. Due to the presence of unreacted precursor B-TiO₂_200 showed a high absorbance in UV-Vis range and washing with a water/ethanol mixture was needed to attenuate the characteristic peak of the powder. To this purpose, after every regular withdrawn of the irradiated dispersion, the sample was centrifuged and further filtrated with a Regenerated Cellulose (RC) syringe filter whose porosity was 0,45 μm.

Both the characteristic peaks of the target molecule disappear sharply meaning that B-TiO₂_200 is very active under simulated solar light. The absorption band related to the aromatic part of the molecule is as shifted as the amine group towards lower wavelengths (blue shift, Fig. 6.6). This result suggests a different degradation mechanism with respect to those described so far. Even if the blue shift still indicates the cleavage of the urea moiety, the hydroxylated aromatic intermediates, resulted from the attack of OH groups binding the ring, have a shorter life being totally degraded after 4 hours.

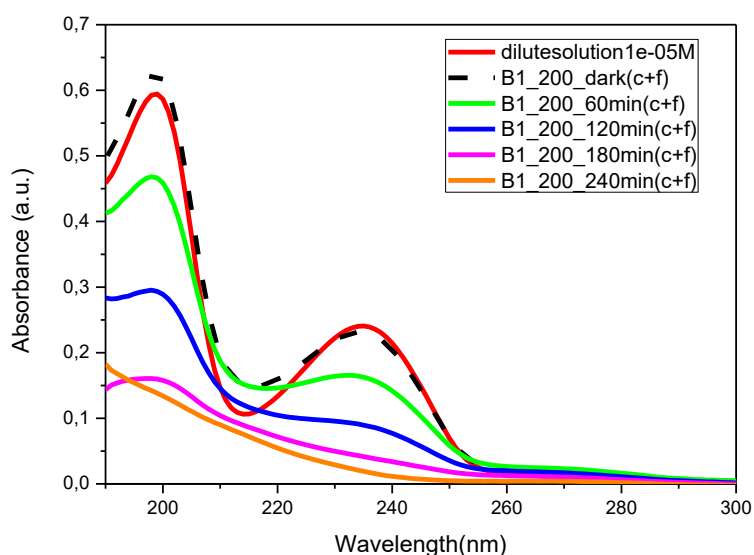


Figure 6.6 UV-Vis spectra of N-phenylurea supernatants withdrawn every hour to test the photocatalytic activity of B-TiO₂_200 sample towards the degradation of the contaminant under simulated solar light.

6.3.6 B-TiO₂_600

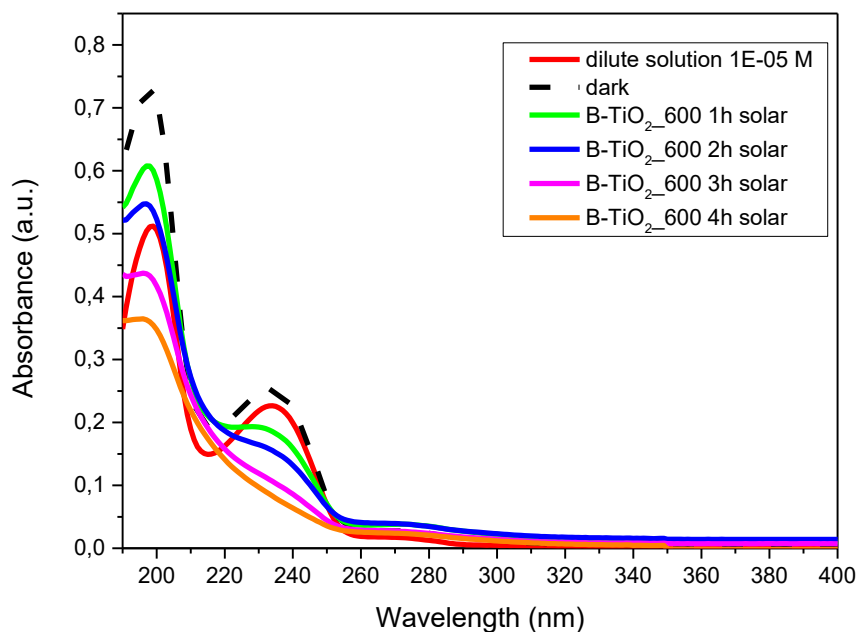


Figure 6.7 UV-Vis spectra of N-phenylurea supernatants withdrawn every hour to test the photocatalytic activity of B-TiO₂_600 sample towards the degradation of the contaminant under simulated solar light

Characteristic peak at 235 nm undergo a blue shift meaning that the cleavage of urea moiety occurred and hydroxylated intermediates appeared (Fig. 6.7). Despite of the brookite content, being promising in phenylurea degradation as the previous test confirms, the absorption band does not effectively disappear after 4 hours as since the sample has a lower surface area than B-TiO₂_200. A new band is present at ~ 220 nm suggesting the formation of hydroxylated aromatic derivatives, as phenol absorbs at 210 nm with a molar extinction coefficient of 6000 M⁻¹cm⁻¹ [111].

6.3.7 Degussa P25

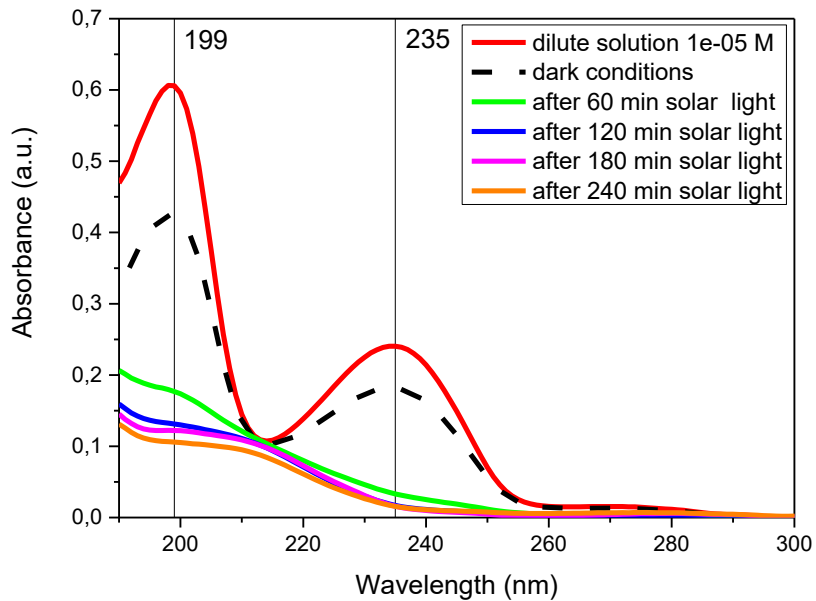


Figure 6.8 UV-Vis spectra of N-phenylurea supernatants withdrawn every hour to test the photocatalytic activity of P25 sample towards the degradation of the contaminant under simulated solar light.

The dotted curve related to the adsorption phenomena shows a decrease in the absorbance meaning that adsorption occurs at the solid surface. Both the characteristic absorption bands at 199 nm and 235 nm disappear progressively and, thus, P25 is active under the action of simulated solar light. (Fig.6.8) It has a competitive behaviour with respect to B-TiO₂_200 as it degrades the aromatic ring after 4 hours even if at the same time the curve related to the sample containing brookite has a steeper slope likely being this catalyst more active towards phenylurea degradation.

6.4 Photocatalytic tests under UV light

6.4.1 Template assisted mesoporous TiO_2 : MT

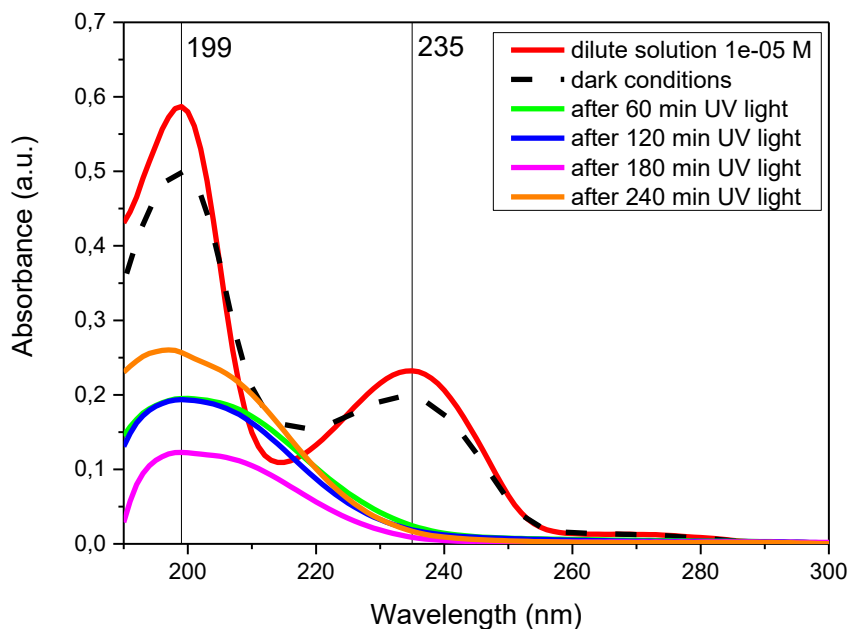


Figure 6.9 UV-Vis spectra of N-phenylurea supernatants withdrawn every hour to test the photocatalytic activity of MT sample towards the degradation of the contaminant under UV light.

After 1 hour in dark conditions the two characteristic peaks of N-phenylurea decrease meaning that adsorption occurs. The combined action of the catalyst and UV light seems to be more effective in the degradation of the contaminant with respect to simulated solar light as the absorption band of the aromatic ring sharply disappears after 1 hour of illumination (Fig. 6.9). This result suggests that no hydroxylated aromatic derivatives can be detected if the measurement is processed every hour. Accordingly to the mechanism already described for the previous tests, the blue shift of the absorption band at 235 nm indicates the cleavage of the urea moiety. If the aromatic ring is totally degraded and mineralized the shape of the curves after 2 hours of illumination could be related to the oxidation of urea producing NO_2^- whose concentration increases in time.

6.4.2 Template assisted mesoporous TiO_2 : Fe-MT_dirc

UV light action provides a more efficient degradation with respect to the simulated solar light even in this test. Hyperchromic effect is not present anymore for the absorption peak at 235 nm meaning that hydroxyl radicals preferentially attack the ring that is partially degraded after 3 hours of illumination. A slight change in the shape of the curve suggests that the ring is likely opened after 4 hours and aliphatic degradation products are formed undergoing decarboxylation (Fig.6.10)

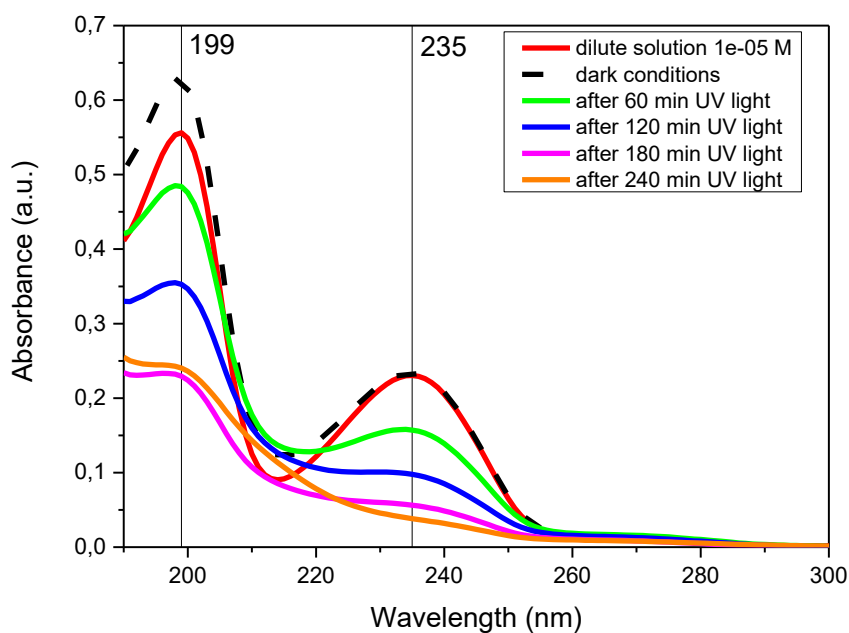


Figure 6.10 UV-Vis spectra of N-phenylurea supernatants withdrawn every hour to test the photocatalytic activity of Fe-MT_dirc sample towards the degradation of the contaminant under UV light.

6.4.3 RM-TiO₂

RM-TiO₂ efficiently works under UV light as the absorbance peak of the aromatic part of the molecule at 235 nm sharply disappears after 1 hour of illumination meaning that the ring is being degrading. No clear shifts of the characteristic bands are recorded after 2 hours (Fig. 6.11). This result suggests that the degradation product is stable and its concentration is almost constant. Also in this case the most likely degradation product seems to be a carboxyl acid. Nitrates or nitrites could be present in traces, deriving from the oxidation of the aliphatic chain of the molecule, but they are not detectable due to low concentration.

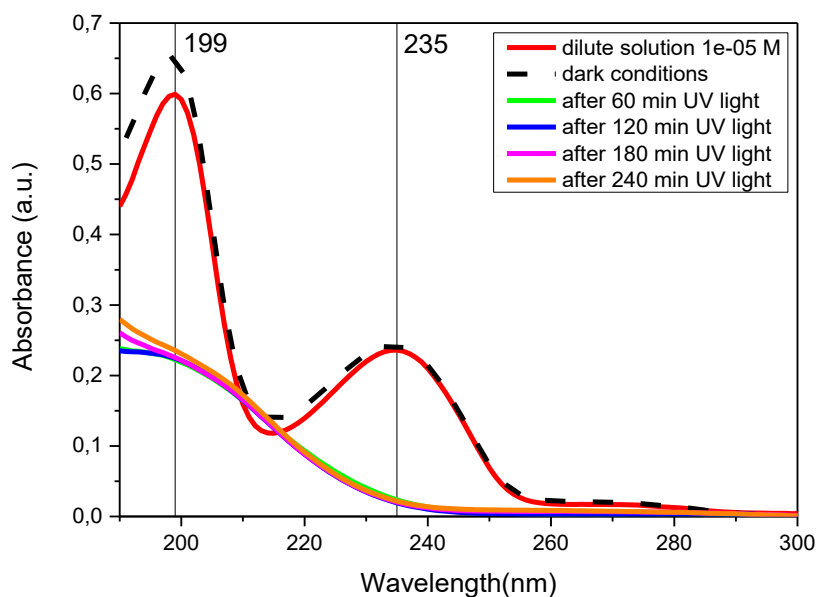


Figure 6.11 UV-Vis spectra of N-phenylurea supernatants withdrawn every hour to test the photocatalytic activity of RM-TiO₂ sample towards the degradation of the contaminant under UV light.

6.4.4 B-TiO₂_200

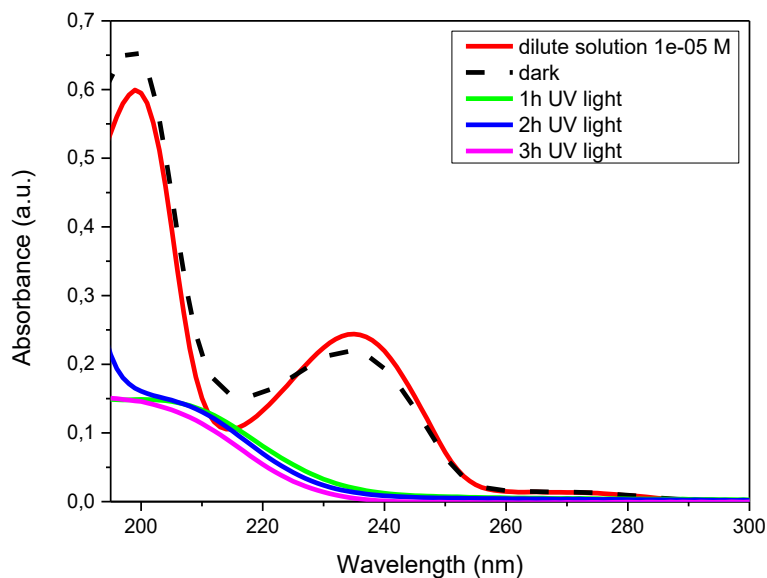


Figure 6.12 UV-Vis spectra of N-phenylurea supernatants withdrawn every hour to test the photocatalytic activity of B-TiO₂_200 sample towards the degradation of the contaminant under UV light.

B-TiO₂_200 is very active in the degradation of the contaminant under UV light as the aromatic ring is totally degraded after 1 hour of illumination (Fig. 6.12). Successive

measurements recorded similar spectra meaning that the degradation product is stable during the test.

6.4.5 B-TiO₂_600

The sample is active in the degradation of the pollutant since a bathochromic effect (blue shift) occurs in the absorption band at 235 nm after 1 hour of illumination meaning that the aromatic ring is soon degraded. The band appearing at 280-300 could be ascribed to the formation of nitrates (Fig. 6.13).

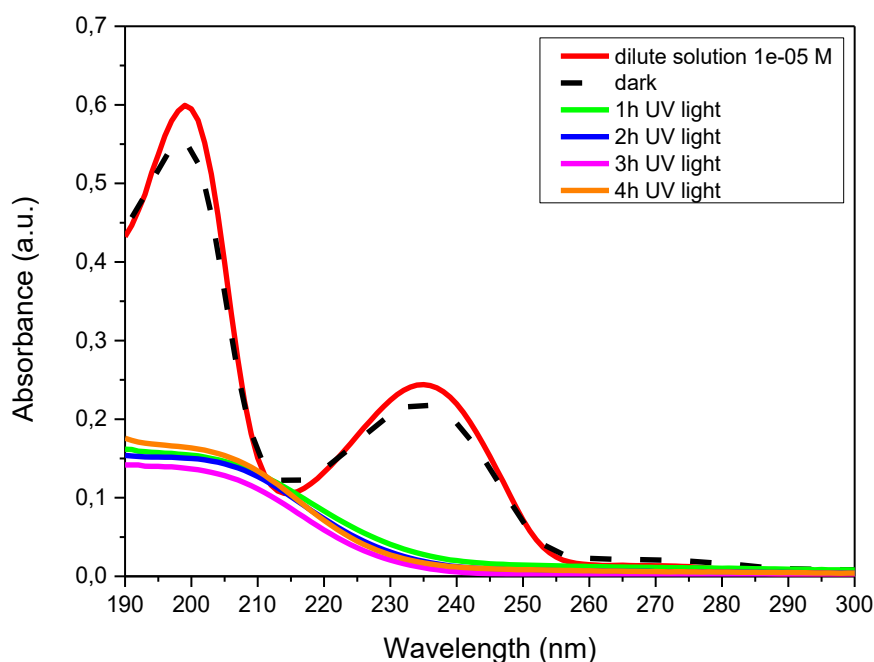


Figure 6.13 UV-Vis spectra of N-phenylurea supernatants withdrawn every hour to test the photocatalytic activity of B-TiO₂_600 sample towards the degradation of the contaminant under UV light.

6.4.6 Degussa P25

The dotted curve related to the adsorption/desorption phenomena shows that characteristic absorbance peaks decrease in dark condition due to a good dispersibility of the powder in the water solution that promotes good interaction between the active site of the catalyst and the molecules of the pollutant. On the other hand, P25 is very light and volatile and a syringe filter was needed to separate the solid from the supernatant. It is active in the degradation of the aromatic ring since absorption band at 235 nm disappears after 1 hour (Fig 6.14).

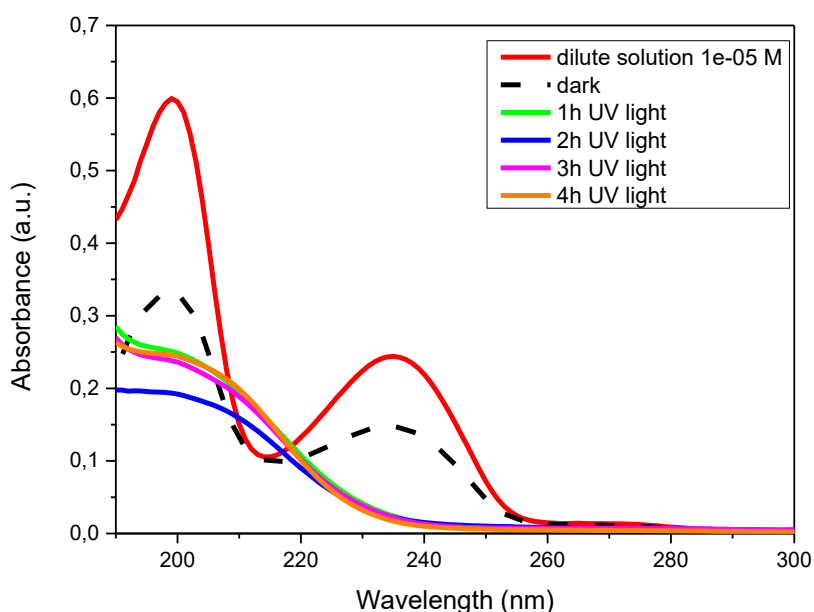


Figure 6.14 UV-Vis spectra of N-phenylurea supernatants withdrawn every hour to test the photocatalytic activity of P25 sample towards the degradation of the contaminant under UV light.

It is interesting to notice that all the powders tested under UV light show the same behaviour related to the shape of the spectra recorded after regular intervals of time, except for MT and Fe-MT_dirc suggesting that degradation mechanisms could be different. Surely, it could be ascribed to the synthesis methods used, i.e. pure anatase TiO₂ obtained by a template assisted method promote the formation of degradation product (NO₂⁻) that could be still harmful.

6.5 Powders behaviour under simulated solar light and UV light

6.5.1 UV light

The two characteristic absorption bands at 199 and 235 nm disappear after 4 hours of illumination for both the samples that contain brookite phase (Fig. 6.15). B-TiO₂_200 and B-TiO₂_600 have similar behaviour under UV light meaning that the presence of mixed phases improves the photocatalytic activity. Since B-TiO₂_600 has a lower surface area (31 m²/g) it can be stated that specific surface area has a minor effect on photocatalytic efficiency although it provides a larger number of active sites available for the reaction.

A similar trend in the degradation of phenylurea is shown by RM-TiO₂. This could be ascribed to the presence of the three phases as well. B-TiO₂_600 seems to be more effective due to synthesis conditions. Acidic conditions promote the formation of a larger amount of brookite; calcination temperature at 600°C causes brookite to rutile (BR) phase transition being responsible of hindering the electron-hole recombination.

6.5.2 Solar light

After 4 hours of illumination the sample B-TiO₂_200 is able to degrade the aromatic ring (i.e. the absorption band at 235 nm) almost completely (Fig. 6.16). This result could be ascribed to the properties of the catalyst structure: it is characterized by the largest brookite amount and the largest surface area (due to calcination process at 200°C). P25 gives similar results probably due to the presence of mixed phases (anatase+rutile) that are highly interconnected enhancing the photocatalytic activity. B-TiO₂_600 even works well under solar light notwithstanding its small surface area. Its good photocatalytic activity is likely due to the presence of brookite (in a smaller amount than B-TiO₂_200) that is quickly transformed to rutile after the calcination at 600°C. So, the presence of different phases that are interconnected provides a longer lifetime to the photogenerated electron/hole pairs. RM-TiO₂ shows a controversial behaviour being the least active sample under solar light. It has a surface area comparable to P25 but it does not show the same photocatalytic activity due to its morphology. It is characterized by having small nanoparticles that easily form aggregates, likely lowering the quantum yield of the reaction. On the contrary, the commercial catalyst is finely dispersed, providing a larger surface area actually involved in the reaction. This issue could suggest that surface area values obtained by N₂ adsorption/desorption isotherms calculations are not representative of the surface actually available for the photocatalytic reaction. This is a crucial point, indicating the importance of aggregation/agglomeration processes that may occur and affect the final performance of the catalyst.

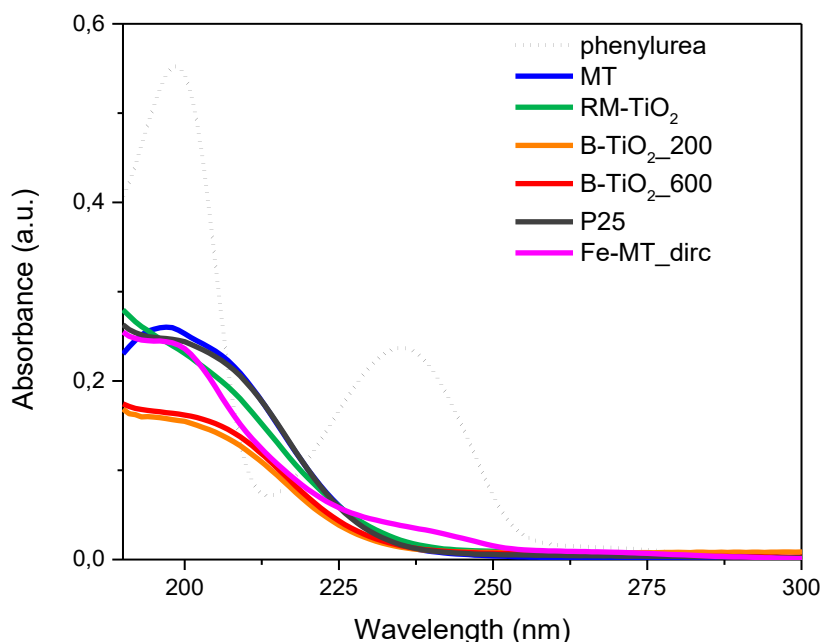


Figure 6.15 A comparison of the UV-Vis spectra of the supernatants obtained after 4h of simulated solar light irradiation.

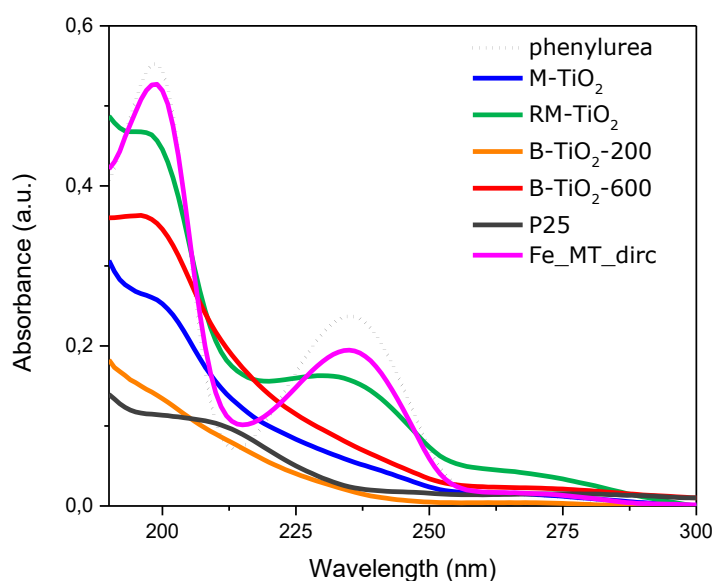


Figure 6.16 A comparison of the UV-Vis spectra of the supernatants obtained after 4h of UV light irradiation.

In Fig. 6.17 the trend of the characteristic absorption peak at 225 nm over illumination time is shown. Both B-TiO₂_200 and P25 samples degrade the contaminant almost completely after 240 minutes.

6.6 N-phenylurea degradation rate under simulated solar light

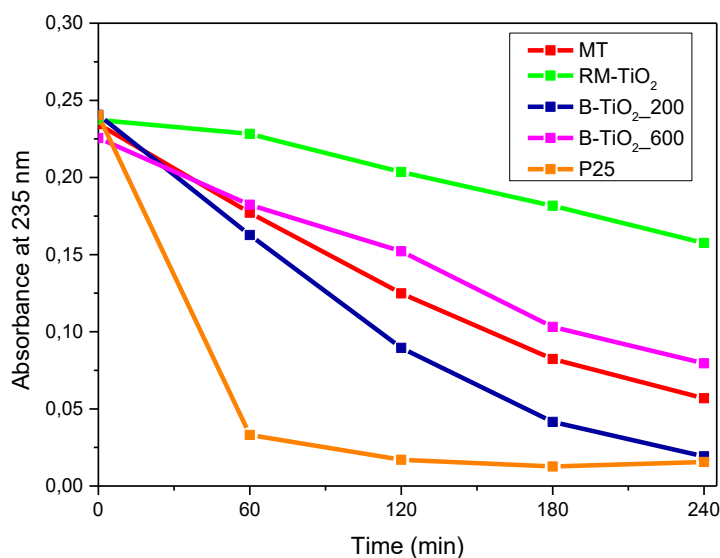


Figure 6.17 Absorbance at 235 nm of the supernatant withdrawn every hour during the photocatalytic test.

As shown in chapter 2, N-phenylurea degradation kinetics can be studied by using Langmuir-Hinshelwood (LH) approach. The contaminant follows a pseudo first order kinetics that can be described by the following equation (Eq. 6.1):

$$C_t = C_0 e^{-kt} \quad (6.1)$$

Where C_t (mol L^{-1}) is the contaminant concentration at time t ; C_0 is the initial concentration; k is the rate constant (in min^{-1}) and its values are shown in Table 6.1.

The equation above is linearized and it takes the following form (Eq. 6.2):

$$\ln\left(\frac{C_t}{C_0}\right) = -kt \quad (6.2)$$

The rate constant is now the slope of the straight line in a semilog plot (Fig. 6.18). The line equation is obtained by a linear fitting provided by OriginPro9 Software. Contaminant half-life time (Eq. 6.3) can be computed as:

$$t_{1/2} = 0.639/k \quad (6.3)$$

Since the Lambert-Beer law is valid in the concentration range used to perform the tests, C (concentration) values can be substituted with A (absorbance) values.

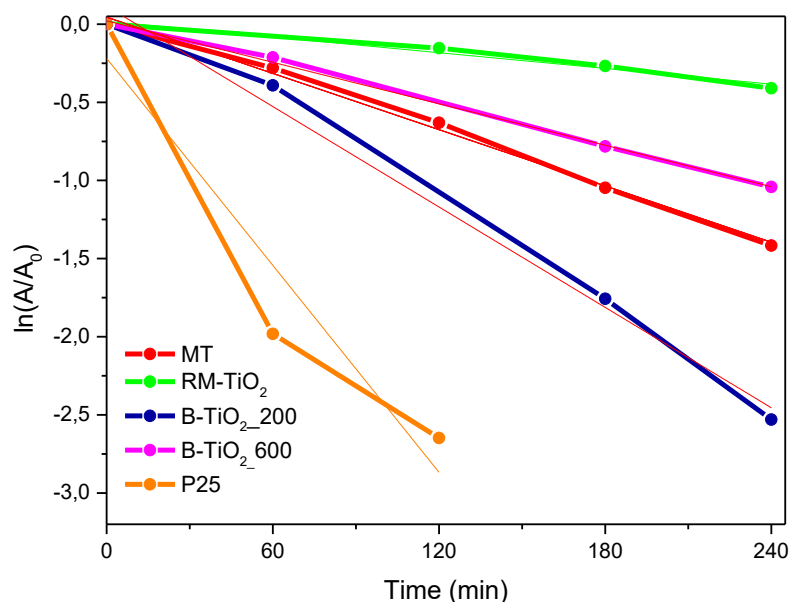


Figure 6.18 N-phenylurea follows a pseudo first order kinetics as confirmed from the linear interpolation of the data in a semilog plot.

Table 6.1 N-phenylurea degradation rate constants

Sample	Rate constant k (min^{-1})	R^2	$t_{1/2}$ (min)
MT	0.006	0.99405	106.5
RM-TiO ₂	0.00167	0.96543	382.6
B-TiO ₂ _200	0.01071	0.98545	59.7
B-TiO ₂ _600	0.00442	0.99681	144.6
P25	0.02207	0.84824	28.95

7. Summary

The aim of this work was the synthesis of nanostructured TiO₂ mixed phases to be applied in the photocatalytic degradation of N-phenylurea, currently considered an emerging contaminant.

Three different sol-gel synthesis methods were used to produce the TiO₂ nanoparticles:

- (i) Template assisted sol-gel method by using a triblock copolymer (Pluronic P123); followed by calcination at 450°C to obtain pure anatase.
- (ii) Template assisted sol-gel method in a reverse micelles environment by using a diblock copolymer (commercial name Brij O20) in a water in oil (w/o) emulsion.

The use of the template promoted the formation of nanoparticles with controlled size and mesoporous structure. The acidic environment within the microreactors (reverse micelles) also promoted the formation of brookite.

- (iii) Template-free sol-gel method in acidic conditions: the pH was tuned by addition of HNO₃. The sample showed the largest brookite amount and the largest specific surface area.

The synthesized catalysts were characterized by means of X-ray Powder Diffraction (XRD) to obtain information about crystal structure and phase composition (Rietveld refinement); N₂ adsorption/desorption isotherms at 77 K were measured to calculate the specific surface area. ζ potential measurements were performed to calculate pH_{IEP} values. To this purpose, all the samples have a lower pH_{IEP} with respect to the commercial TiO₂ (6.2-6.9). This result could be ascribed to the different size of the particles and the synthesis condition as well.

A rough estimation of the polydispersity index (PDI) was given by means of DLS (dynamic light scattering) measurements. PDI values for the two samples synthesized by the third method are ca. 0.6 suggesting that their nanoparticles were better dispersed in water than those of M-TiO₂_200 or Fe-MT_dirc. This result confirmed that the presence of aggregates/agglomerates in water likely lowered the quantum yield of the process.

Finally, synthesis in acidic medium promoted the formation of brookite (see B-TiO₂_200 and RM-TiO₂). B-TiO₂_600 was calcined at 600°C, it has a lower surface area with respect to the sample calcined at 200°C due to the increasing crystallinity. In agreement with the temperature chose for the thermal treatment, a small amount of rutile occurred due to BR (brookite to rutile) transition leading to a slower recombination rate.

In order to investigate the optical properties of TiO₂ nanoparticles diffuse reflectance (DR-UV) measurements were performed by means of an integrated sphere mounted on the spectrophotometer to calculate the band gap. As expected, Fe-MT_dirc showed the lower E_g value (2.3 eV) confirming the ability of the sample to absorb better in the visible range. Both

direct and indirect band gaps were calculated since mixed phases were tailored. By focusing on the values obtained using the Tauc plot method, B-TiO₂_200 resulted in a larger one with the respect to the pure anatase sample (M-TiO₂). This is due to the presence of both anatase and brookite: the content of brookite causes an increase of E_g as reported in literature.

All the powders were tested both under solar and UV light. Good results in the degradation of N-phenylurea were shown by B-TiO₂_200 which is the sample with the largest content of brookite and specific surface area. B-TiO₂_600 showed a good activity as well notwithstanding its smaller surface area. It works well under both the light sources used during the photocatalytic tests thanks to the presence of highly interconnected phases (anatase+brookite+rutile) that hinders electron/hole recombination. This result may suggest that the fate of the photogenerated pair has a relevant effect with respect to the surface area available for the reaction towards the photocatalytic activity. Finally, promising results were obtained in the presence of the B-TiO₂ samples. P25 was very active towards the degradation of the contaminant, being a mixture of anatase and rutile. Again, the compresence of the two phases enhances the photocatalytic activity. This powder was finely dispersed in water and probably provided a larger actual surface area to the reaction. Conversely, RM-TiO₂ was made of highly aggregated particles resulting in the less active sample. Even if its specific surface area is comparable to that of P25, particle aggregation hinders diffusion phenomena and the quantum yield of the reaction (aggregates increase the suspension turbidity). P25 dispersibility in water may suggest that a lower amount of the catalyst could be needed to perform the tests. Future works could be devoted to calculating the optimal powder amount normalized to the specific surface area with respect to the commercial sample. N-phenylurea has a degradation pathway difficult to understand by means of analytical techniques used in this work. Liquid chromatography could be used to better investigate about oxidation intermediates that, in most cases, could be more harmful than the starting molecule. In order to quantitatively estimate the activity of the catalysts towards the degradation of the contaminant a study of the kinetics (i.e. calculation of rate constants) could be performed.

Bibliography

- [1] P. Verlicchi, “I contaminanti emergenti nelle acque: a che punto siamo arrivati?,” *Ing. dell’ambiente*, vol. 5, pp. 147–148, 2018.
- [2] G. W. A. Milne, *CRC Handbook of Pesticides*. CRC Press, 2018.
- [3] Consiglio Nazionale delle Ricerche (CNR), “Microinquinanti emergenti (MIE) nelle acque di rifiuto urbane: esperienze italiane e svizzere.” [Online]. Available: <https://www.cnr.it/it/evento/13532/microinquinanti-emergenti-mie-nelle-acque-di-rifiuto-urbane-esperienze-italiane-e-svizzere>. [Accessed: 10-Aug-2018].
- [4] F. S. Freyria, F. Geobaldo, and B. Bonelli, “Nanomaterials for the abatement of pharmaceuticals and personal care products from wastewater,” *Applied Sciences (Switzerland)*. 2018.
- [5] J. Dich, S. H. Zahm, A. Hanberg, and H. O. Adami, “Pesticides and cancer,” *Cancer Causes and Control*. 1997.
- [6] M. I. Al-Wabel, G. Abdel-Nass, A. M. Al-Turki, and M. H. El-Saeid, “Behavior of Atrazine and Malathion Pesticides in Soil: Sorption and Degradation Processes,” *J. Appl. Sci.*, vol. 10, no. 16, pp. 1740–1747, Dec. 2010.
- [7] B. Yuan, S. Liang, Y.-X. Jin, M.-J. Zhang, J.-B. Zhang, and N.-H. Kim, “Toxic effects of atrazine on porcine oocytes and possible mechanisms of action.,” *PLoS One*, vol. 12, no. 6, p. e0179861, 2017.
- [8] T. B. Hayes *et al.*, “Hermaphroditic, demasculinized frogs after exposure to the herbicide atrazine at low ecologically relevant doses,” *Proc. Natl. Acad. Sci.*, vol. 99, no. 8, pp. 5476–5480, 2002.
- [9] E. L. Arthur, B. S. Perkovich, T. A. Anderson, and J. R. Coats, “Degradation of an Atrazine and Metolachlor Herbicide Mixture in Pesticide-Contaminated Soils from Two Agrochemical Dealerships in Iowa,” *Water. Air. Soil Pollut.*, vol. 119, no. 1/4, pp. 75–90, 2000.
- [10] J. G. Speight and J. G. Speight, “Chemical Transformations in the Environment,” *Environ. Org. Chem. Eng.*, pp. 305–353, Jan. 2017.
- [11] J. G. Speight and J. G. Speight, “Transformation of Inorganic Chemicals in the Environment,” *Environ. Inorg. Chem. Eng.*, pp. 333–382, Jan. 2017.
- [12] C. C. Wong and W. Chu, “The direct photolysis and photocatalytic degradation of alachlor at different TiO₂ and UV sources,” *Chemosphere*, vol. 50, no. 8, pp. 981–987, 2003.
- [13] M. Saverini, “Genotossicità in cellule procariotiche ed eucariotiche dei terpeni presenti nei reflui della industria agrumaria e loro degradazione per mezzo di fotocatalisi

eterogenea.”

- [14] A. FUJISHIMA and K. HONDA, “Electrochemical Photolysis of Water at a Semiconductor Electrode,” *Nature*, vol. 238, no. 5358, pp. 37–38, Jul. 1972.
- [15] M. Pelaez *et al.*, “A review on the visible light active titanium dioxide photocatalysts for environmental applications,” *Appl. Catal. B Environ.*, vol. 125, pp. 331–349, Aug. 2012.
- [16] L. J. Antila, F. G. Santomauro, L. Hammarström, D. L. A. Fernandes, and J. Sá, “Hunting for the elusive shallow traps in TiO₂ anatase,” *Chem. Commun.*, vol. 51, no. 54, pp. 10914–10916, 2015.
- [17] S. Anandan, Y. Ikuma, and K. Niwa, “An Overview of Semi-Conductor Photocatalysis: Modification of TiO₂ Nanomaterials,” *Solid State Phenom.*, vol. 162, pp. 239–260, 2010.
- [18] J. Liu, L. Zhang, X. Yao, and S. S. C. Chuang, “Photo-generated conduction-band and shallow-trap electrons from UV irradiation on ethanol-adsorbed TiO₂ and N-TiO₂: an in situ infrared study,” *Res. Chem. Intermed.*, vol. 43, no. 9, pp. 5041–5054, 2017.
- [19] T. Hirakawa, K. Yawata, and Y. Nosaka, “Photocatalytic reactivity for O₂⁻ and OH radical formation in anatase and rutile TiO₂ suspension as the effect of H₂O₂ addition,” *Appl. Catal. A Gen.*, vol. 325, no. 1, pp. 105–111, May 2007.
- [20] A. Fujishima and X. Zhang, “Titanium dioxide photocatalysis: present situation and future approaches,” *Comptes Rendus Chimie*. 2006.
- [21] V. Caratto *et al.*, “Studio dell’attività fotocatalitica di nano-particelle di TiO₂ su batteri gram negativi.”
- [22] J. Schneider *et al.*, “Understanding TiO₂ photocatalysis: Mechanisms and materials,” *Chem. Rev.*, vol. 114, no. 19, pp. 9919–9986, 2014.
- [23] J. Jing, M. Liu, V. L. Colvin, W. Li, and W. W. Yu, “Photocatalytic degradation of nitrogen-containing organic compounds over TiO₂,” *J. Mol. Catal. A Chem.*, vol. 351, pp. 17–28, 2011.
- [24] S. Malato, J. Blanco, J. Cáceres, A. R. Fernández-Alba, A. Agüera, and A. Rodríguez, “Photocatalytic treatment of water-soluble pesticides by photo-Fenton and TiO₂ using solar energy,” 2002.
- [25] K. Nishizawa, M. Okada, and E. Watanabe, “New Preparation Method of Visible Light Responsive Titanium Dioxide Photocatalytic Films,” *Mater. Sci. Appl.*, 2014.
- [26] “Fotocatalisi.” [Online]. Available: <https://www.airclean-led.com/it/aspetti-tecnici/fotocatalisi>. [Accessed: 10-Aug-2019].
- [27] S. Kuriakose, N. Bhardwaj, J. Singh, B. Satpati, and S. Mohapatra, “Structural, optical and photocatalytic properties of flower-like ZnO nanostructures prepared by a facile

- wet chemical method,” *Beilstein J. Nanotechnol.*, vol. 4, no. 1, pp. 763–770, 2013.
- [28] E. Evgenidou, K. Fytianos, and I. Poulios, “Photocatalytic oxidation of dimethoate in aqueous solutions,” vol. 175, pp. 29–38, 2005.
- [29] X. Chen *et al.*, “Accelerated TiO₂ photocatalytic degradation of Acid Orange 7 under visible light mediated by peroxymonosulfate,” *Chem. Eng. J.*, vol. 193–194, pp. 290–295, 2012.
- [30] G. Yang, Z. Jiang, H. Shi, T. Xiao, and Z. Yan, “Preparation of highly visible-light active N-doped TiO₂ photocatalyst,” *J. Mater. Chem.*, vol. 20, no. 25, pp. 5301–5309, 2010.
- [31] A. Zaleska, “Doped-TiO₂: A Review,” *Recent Patents Eng.*, vol. 2, no. 3, pp. 157–164, 2008.
- [32] S. A. Ansari, M. M. Khan, M. O. Ansari, and M. H. Cho, “Nitrogen-doped titanium dioxide (N-doped TiO₂) for visible light photocatalysis,” *New J. Chem.*, vol. 40, no. 4, pp. 3000–3009, 2016.
- [33] B. Bonelli, S. Esposito, F. F.-T. Dioxide, and undefined 2017, “Mesoporous Titania: Synthesis, properties and comparison with non-porous titania,” *intechopen.com*.
- [34] M. B. Marami, M. Farahmandjou, and B. Khoshnevisan, “Sol–Gel Synthesis of Fe-Doped TiO₂ Nanocrystals,” *J. Electron. Mater.*, vol. 47, no. 7, pp. 3741–3748, 2018.
- [35] N. Banić *et al.*, “Photodegradation of thiacloprid using Fe/TiO₂ as a heterogeneous photo-Fenton catalyst,” *Appl. Catal. B Environ.*, vol. 107, no. 3–4, pp. 363–371, 2011.
- [36] J. Araña, O. González Díaz, M. Miranda Saracho, J. M. Doa Rodríguez, J. A. Herrera Melián, and J. Pérez Pea, “Photocatalytic degradation of formic acid using Fe/TiO₂ catalysts: The role of Fe³⁺/Fe²⁺ ions in the degradation mechanism,” *Appl. Catal. B Environ.*, vol. 32, no. 1–2, pp. 49–61, 2001.
- [37] T. S.r.l, “I nanomateriali nel campo dell ’ innovazione tecnologica : i prodotti foto catalitici e le loro applicazioni.” .
- [38] F. Scarpelli, T. F. Mastropietro, T. Poerio, and N. Godbert, “Mesoporous TiO₂ Thin Films: State of the Art,” *Titan. Dioxide - Mater. a Sustain. Environ.*, no. June, 2018.
- [39] L. E. Oi, M.-Y. Choo, H. V. Lee, H. C. Ong, S. B. A. Hamid, and J. C. Juan, “Recent advances of titanium dioxide (TiO₂) for green organic synthesis,” *RSC Adv.*, vol. 6, no. 110, pp. 108741–108754, 2016.
- [40] Y. Zhang *et al.*, “Titanate and titania nanostructured materials for environmental and energy applications: A review,” *RSC Adv.*, vol. 5, no. 97, pp. 79479–79510, 2015.
- [41] “Strutture della titania.” [Online]. Available: http://lem.ch.unito.it/didattica/infochimica/2010_Titania/struttura.html. [Accessed: 10-Aug-2019].

- [42] J. Zhang, P. Zhou, J. Liu, and J. Yu, “New understanding of the difference of photocatalytic activity among anatase, rutile and brookite TiO₂,” *Phys. Chem. Chem. Phys.*, vol. 16, no. 38, pp. 20382–20386, 2014.
- [43] A. Kumar, “Different Methods Used for the Synthesis of TiO₂ Based Nanomaterials: A Review,” *Am. J. Nano Res. Appl.*, 2018.
- [44] P. Nyamukamba, O. Okoh, H. Mungondori, R. Taziwa, and S. Zinya, “Synthetic Methods for Titanium Dioxide Nanoparticles: A Review,” in *Titanium Dioxide - Material for a Sustainable Environment*, 2018.
- [45] E. Stathatos, P. Lianos, F. Del Monte, D. Levy, and D. Tsiourvas, “Formation of TiO₂ nanoparticles in reverse micelles and their deposition as thin films on glass substrates,” *Langmuir*, 1997.
- [46] R. Nasi *et al.*, “Application of reverse micelle sol-gel synthesis for bulk doping and heteroatoms Surface Enrichment in Mo-Doped TiO₂ nanoparticles,” *Materials (Basel)*, 2019.
- [47] European Commission, “Pesticides|Food Safety.” [Online]. Available: https://ec.europa.eu/food/plant/pesticides_en. [Accessed: 10-Aug-2019].
- [48] “Pesticidi Sistemici – The Task Force on Systemic Pesticides.” [Online]. Available: <http://www.tfsp.info/it/systemic-pesticides/>. [Accessed: 04-Jun-2019].
- [49] Istituto Agrario Sartor, “Fitofarmaci – Prodotti fitosanitari.”
- [50] ISPRA, *Rapporto nazionale pesticidi nelle acque (dati 2015-2016)*. 2018.
- [51] European Union, “Council Decision 2006/507/EC concerning the conclusion, on behalf of the European Community, of the Stockholm Convention on Persistent Organic Pollutants,” *Off. J. Eur. Union*, vol. 2006, no. L, pp. 1–53, 2002.
- [52] “Persistent Organic Pollutants.” [Online]. Available: [http://www.eugris.info/FurtherDescription.asp?e=93&Ca=2&Cy=0&T=Persistent Organic Pollutants](http://www.eugris.info/FurtherDescription.asp?e=93&Ca=2&Cy=0&T=Persistent%20Organic%20Pollutants). [Accessed: 04-Jun-2019].
- [53] Ministero dell’Ambiente e della Tutela del Territorio e del Mare, “Decreto 14 aprile 2009 n.56,” *Gazz. Uff.*, pp. 1–13, 2009.
- [54] Q.F., “Glifosato, Bayer condannata per il Roundup: è la terza volta. Due miliardi a una coppia che ha contratto il cancro,” 2019. [Online]. Available: <https://www.ilfattoquotidiano.it/2019/05/14/glifosato-bayer-condannata-diserbante-roundup-e-la-terza-volta-due-miliardi-a-una-coppia-che-ha-contratto-il-cancro/5177478/>. [Accessed: 10-Aug-2019].
- [55] J. Giliberto, *Pesticidi nell’acqua: Piemonte e Friuli in testa*. 2018.
- [56] F. Freyria, M. Armandi, ... M. C.-... of N. and, and undefined 2017, “Catalytic and photocatalytic processes for the abatement of N-containing pollutants from wastewater.

Part 2: Organic pollutants,” *ingentaconnect.com*.

- [57] “N-Phenylurea 97% | Sigma-Aldrich.” [Online]. Available: <https://www.sigmaaldrich.com/catalog/product/aldrich/p36959?lang=it®ion=IT>. [Accessed: 04-Jun-2019].
- [58] “PHENYLUREA | 64-10-8.” [Online]. Available: https://www.chemicalbook.com/ChemicalProductProperty_EN_CB2252571.htm. [Accessed: 04-Jun-2019].
- [59] J. Liu, *Phenylurea Herbicides*, Third Edit., vol. Volume 2. Elsevier Inc., 2010.
- [60] D. Bamba, M. Coulibaly, and D. Robert, “Nitrogen-containing organic compounds: Origins, toxicity and conditions of their photocatalytic mineralization over TiO₂,” *Sci. Total Environ.*, vol. 580, pp. 1489–1504, 2017.
- [61] M. A. Oturan, M. C. Edelahi, N. Oturan, K. El kacemi, and J.-J. Aaron, “Kinetics of oxidative degradation/mineralization pathways of the phenylurea herbicides diuron, monuron and fenuron in water during application of the electro-Fenton process,” *Appl. Catal. B Environ.*, vol. 97, no. 1–2, pp. 82–89, Jun. 2010.
- [62] AA.VV, “Diserbanti ureici,” pp. 653–660, 2000.
- [63] R. Zouaghi, A. Zertal, B. David, and S. Guittonneau, “Photocatalytic Degradation of Monolinuron and Linuron in an Aqueous Suspension of Titanium Dioxide Under Simulated Solar Irradiation,” *Rev. des Sci. l’eau*, vol. 20, no. 2, p. 163, 2007.
- [64] L. Lhomme, S. Brosillon, D. Wolbert, and J. Dussaud, “Photocatalytic degradation of a phenylurea, chlortoluron, in water using an industrial titanium dioxide coated media,” *Appl. Catal. B Environ.*, vol. 61, no. 3–4, pp. 227–235, Nov. 2005.
- [65] E. Pramauro, M. Vincenti, V. Augugliaro, and L. Palmisano, “Photocatalytic Degradation of Monuron in Aqueous TiO₂ Dispersions,” *Environ. Sci. Technol.*, vol. 27, no. 9, pp. 1790–1795, 1993.
- [66] J. Zeng *et al.*, “Common characteristic assessments of transformation mechanism for substituted phenylurea herbicides by reactive oxygen species (ROSs) during photocatalytic process,” *Chem. Eng. J.*, vol. 273, pp. 519–526, 2015.
- [67] A. Amine-Khodja, A. Boulkamh, and P. Boule, “Photochemical behaviour of phenylurea herbicides,” *Photochemical and Photobiological Sciences*. 2004.
- [68] N. W. Ashcroft and N. D. Mermin, “Solid State Physics,” *Solid State Physics*. 1976.
- [69] B. Mallick, “X-ray diffraction analysis of polymeric solid using Bragg-Brentano geometry,” *Int. J. Appl. Glas. Sci. Mater. Chem. Phys.*, 2015.
- [70] S. Vicini and E. Princi, “Tecniche di caratterizzazione dei polimeri,” 2013.
- [71] F. P. L. Silvestri, M. Pentimalli, “Caratterizzazione Di Materiali Porosi Mediante

Adsorbimento Di Gas : Evoluzione Del Composito Nitruro Di Boro - Grafite
Caratterizzazione Di Materiali Porosi Mediante Adsorbimento Di Gas :,” 2013.

- [72] K. S. W. Sing *et al.*, “Reporting Physisorption Data for Gas/Solid Systems with Special Reference to the Determination of Surface Area and Porosity,” *Pure Appl. Chem.*, vol. 57, no. 4, pp. 603–619, 1985.
- [73] S. Chimiche, T. Valentina, C. Dottorato, P. P. Ugo, and P. F. Pinna, “Sviluppo di materiali a base di TiO₂ per l’ abbattimento di inquinanti,” 2011.
- [74] P. Y. Bruice, *Organic chemistry*. 2016.
- [75] K. A. Mohammad, A. Zekry, and M. Abouelatta, “LED Based Spectrophotometer can compete with conventional one,” *Int. J. Eng. Technol.*, vol. 4, no. 2, p. 399, 2015.
- [76] J. W. Robinson, E. M. Skelly Frame, and G. M. Frame, *Undergraduate instrumental analysis, sixth edition*. 2004.
- [77] AA.VV, “Changes in adsorption spectra.” [Online]. Available: http://photonicswiki.org/index.php?title=Changes_in_Absorption_Spectra. [Accessed: 10-Aug-2019].
- [78] Thermofisher Scientific, “How does FTIR work and why use it?” [Online]. Available: <https://www.thermofisher.com/it/en/home/industrial/spectroscopy-elemental-isotope-analysis/spectroscopy-elemental-isotope-analysis-learning-center/molecular-spectroscopy-information/ftir-information/ftir-basics.html>. [Accessed: 10-Aug-2019].
- [79] Beltrami, “Spettroscopia agli infrarossi in trasformata di Fourier (FTIR).”
- [80] V. Venditto, “Tecniche di Analisi Microscopica Microscopica Ottica,” pp. 1–34.
- [81] G. Fioravanti, “Chimica delle superfici ed interfasi.” 2014.
- [82] D. L. Liao, G. S. Wu, and B. Q. Liao, “Zeta potential of shape-controlled TiO₂ nanoparticles with surfactants,” *Colloids Surfaces A Physicochem. Eng. Asp.*, 2009.
- [83] K. Pate and P. Safier, “Chemical metrology methods for CMP quality,” in *Advances in Chemical Mechanical Planarization (CMP)*, 2016.
- [84] Dipartimento di Chimica Industriale Università di Bologna, “Dynamic Light Scattering (DLS).” [Online]. Available: <http://www.chimica-industriale.unibo.it/it/servizi-e-strutture/strumentazione-scientifica/dynamic-light-scattering-dls>. [Accessed: 10-Aug-2019].
- [85] W. Y. Teoh, “A perspective on the flame spray synthesis of photocatalyst nanoparticles,” *Materials (Basel)*., vol. 6, no. 8, pp. 3194–3212, 2013.
- [86] B. Niu, X. Wang, K. Wu, X. He, and R. Zhang, “Mesoporous titanium dioxide: Synthesis and applications in photocatalysis, energy and biology,” *Materials (Basel)*., vol. 11, no. 10, pp. 1–23, 2018.

- [87] H. Phattepur, G. B. Siddaiah, and N. Ganganagappa, "Synthesis and characterisation of mesoporous TiO₂ nanoparticles by novel surfactant assisted sol-gel method for the degradation of organic compounds," *Period. Polytech. Chem. Eng.*, vol. 63, no. 1, pp. 85–95, 2019.
- [88] S. K. Das, M. K. Bhunia, and A. Bhaumik, "Self-assembled TiO₂ nanoparticles: Mesoporosity, optical and catalytic properties," *Dalt. Trans.*, vol. 39, no. 18, pp. 4382–4390, 2010.
- [89] C. B. D. Marien, C. Marchal, A. Koch, D. Robert, and P. Drogui, "Sol-gel synthesis of TiO₂ nanoparticles: effect of Pluronic P123 on particle's morphology and photocatalytic degradation of paraquat," *Environ. Sci. Pollut. Res.*, vol. 24, no. 14, pp. 12582–12588, 2017.
- [90] F. Freyria *et al.*, "Pure and Fe-Doped Mesoporous Titania Catalyse the Oxidation of Acid Orange 7 by H₂O₂ under Different Illumination Conditions: Fe Doping Improves Photocatalytic Activity under Simulated Solar Light," *Catalysts*, vol. 7, no. 7, p. 213, Jul. 2017.
- [91] B. K. Mutuma, G. N. Shao, W. D. Kim, and H. T. Kim, "Sol-gel synthesis of mesoporous anatase-brookite and anatase-brookite-rutile TiO₂ nanoparticles and their photocatalytic properties," *J. Colloid Interface Sci.*, 2015.
- [92] Royal Society of Chemistry, "TiO₂ : Manufacture of Titanium Dioxide," *RSC Adv. Chem. Sci.*, no. Masterclass: TiO₂, p. 5, 2016.
- [93] E. Masolo *et al.*, "Mesoporous titania powders: The role of precursors, ligand addition and calcination rate on their morphology, crystalline structure and photocatalytic activity," *Nanomaterials*, vol. 4, no. 3, pp. 583–598, 2014.
- [94] S. D. Delekar, H. M. Yadav, S. N. Achary, S. S. Meena, and S. H. Pawar, "Structural refinement and photocatalytic activity of Fe-doped anatase TiO₂ nanoparticles," *Appl. Surf. Sci.*, vol. 263, pp. 536–545, 2012.
- [95] Y. Yalçın, M. Kiliç, and Z. Çınar, "Fe³⁺-doped TiO₂: A combined experimental and computational approach to the evaluation of visible light activity," *Appl. Catal. B Environ.*, vol. 99, no. 3–4, pp. 469–477, 2010.
- [96] S. Wang, J. S. Lian, W. T. Zheng, and Q. Jiang, "Photocatalytic property of Fe doped anatase and rutile TiO₂ nanocrystal particles prepared by sol-gel technique," *Appl. Surf. Sci.*, 2012.
- [97] M. Tsega and F. B. Dejene, "Influence of acidic pH on the formulation of TiO₂ nanocrystalline powders with enhanced photoluminescence property," *Heliyon*, vol. 3, no. 2, p. e00246, 2017.
- [98] M. Koelsch, S. Cassaignon, C. Ta Thanh Minh, J. F. Guillemoles, and J. P. Jolivet, "Electrochemical comparative study of titania (anatase, brookite and rutile) nanoparticles synthesized in aqueous medium," in *Thin Solid Films*, 2004.

- [99] F. Azeez *et al.*, “The effect of surface charge on photocatalytic degradation of methylene blue dye using chargeable titania nanoparticles,” *Sci. Rep.*, 2018.
- [100] K. Suttiponparnit, J. Jiang, M. Sahu, S. Suvachittanont, T. Charinpanitkul, and P. Biswas, “Role of Surface Area, Primary Particle Size, and Crystal Phase on Titanium Dioxide Nanoparticle Dispersion Properties,” *Nanoscale Res. Lett.*, 2011.
- [101] J. P. Holmberg, E. Ahlberg, J. Bergenholtz, M. Hassellöv, and Z. Abbas, “Surface charge and interfacial potential of titanium dioxide nanoparticles: Experimental and theoretical investigations,” *J. Colloid Interface Sci.*, vol. 407, pp. 168–176, Oct. 2013.
- [102] F. Pellegrino *et al.*, “Influence of agglomeration and aggregation on the photocatalytic activity of TiO₂ nanoparticles,” *Appl. Catal. B Environ.*, 2017.
- [103] S. Valencia, J. M. Marín, and G. Restrepo, “Study of the Bandgap of Synthesized Titanium Dioxide Nanoparticles Using the Sol-Gel Method and a Hydrothermal Treatment,” pp. 9–14, 2010.
- [104] J. Zhang, P. Zhou, J. Liu, and J. Yu, “New understanding of the difference of photocatalytic activity among anatase, rutile and brookite TiO₂,” *Phys. Chem. Chem. Phys.*, vol. 16, no. 38, pp. 20382–20386, 2014.
- [105] T. Zhu and S. Gao, “The stability, electronic structure, and optical property of TiO₂ polymorphs,” pp. 12–14.
- [106] M. Monai, T. Montini, and P. Fornasiero, “Brookite: Nothing New under the Sun?,” *Catalysts*, vol. 7, no. 10, p. 304, Oct. 2017.
- [107] S. Paul and A. Choudhury, “Investigation of the optical property and photocatalytic activity of mixed phase nanocrystalline titania,” *Appl. Nanosci.*, 2014.
- [108] J. Moma and J. Baloyi, “Modified Titanium Dioxide for Photocatalytic Applications,” in *Photocatalysts - Applications and Attributes*, 2019.
- [109] M. Szyper and P. Zuman, “Electronic absorption of carboxylic acids and their anions,” *Anal. Chim. Acta*, 1976.
- [110] H. Boucheloukh, T. Sehili, N. Kouachi, and K. Djebbar, “Kinetic and analytical study of the photo-induced degradation of monuron by nitrates and nitrites under irradiation or in the dark,” *Photochem. Photobiol. Sci.*, 2012.
- [111] J. C. Dearden and W. F. Forbes, “Light absorption studies,” *Can. J. Chem.*, vol. 37, no. 6, pp. 1145–1154, 1955.